Department of Physics
University of Jyväskylä
Research Report No. 9/2011

Studies of $T_z = -\frac{3}{2}$ Nuclei of Astrophysical Interest

by
Antti Saastamoinen

Academic Dissertation
for the Degree of
Doctor of Philosophy

To be presented, by permission of the
Faculty of Mathematics and Natural Sciences
of the University of Jyväskylä,
for public examination in Auditorium FYS 1 of the
University of Jyväskylä on December 8th, 2011
at 12 o'clock noon

Jyväskylä, Finland
December 2011

Preface

Studies presented in this thesis have been carried out during 2005-2011 in the Accelerator laboratory of the University of Jyväskylä and in the Cyclotron institute of the Texas A&M University. These years and numerous experiments (most of which are not included here) have showed that experimental physics is most of all team work and this work is not possible without the efforts of so many people with different skills.

First of all, I would like to thank my supervisors Prof. Juha Äystö and Prof. Ari Jokinen for introducing the world of experimental nuclear physics, all the guidance over these years and giving the opportunity to work in the IGISOL group. This group has been an excellent team to work with and I would like to thank the past and present members for the enjoyable moments in the lab and outside the work. A special thanks goes to Dr. Tommi Eronen and Dr. Viki-Veikko Elomaa for the help on trap related issues, Dr. Sami Rinta-Antila for all the help getting started with spectroscopy electronics and IGISOL in general, Dr. Kari Peräjärvi and Dr. Heikki Penttilä for the discussions and insights into different aspects of this work, Dr. Iain Moore for the valuable comments and proof-reading this manuscript as well as all the interesting discussions; Dr. Pasi Karvonen, Mr. Mikael Reponen, Mr. Janne Ronkainen and Mr. Dmitry Gorelov for sharing the workload keeping the IGISOL front-end running.

Major part of this work was done in the Texas A&M University and the friendliness and hospitality of the people of the Cyclotron institute is much appreciated. Dr. Livius Trache has been almost an unofficial supervisor to me, so I would like to thank him for the help and guidance. I would like to thank Dr. Adriana Banu, Dr. Matt McCleskey and Dr. Brian Roeder for the help related to the experiments and for all the fun outside the lab. I would like to thank Dr. Peter Dendooven and Dr. Sivaji Purushothaman for the collaboration on cryogenic devices and for the hospitality during my visits to KVI. Out of other experimental work, not included in this thesis, it has been a privilege to participate in experiments at KVI, ISOLDE and JYFL within the Aarhus-Madrid-Gothenburg-York-JYFL collaboration and I would like to thank all the members for the great work done.

Department of Physics has been a pleasant place to work and study, so the whole staff deserves a big thanks for the atmosphere. I would like to thank Mr. Mikko Laitinen for sharing the office, all the interesting discussions and tolerating my sports gear in the office. None of this work would have not been possible without the excellent support from the technical staffs of JYFL, TAMU and KVI laboratories. Especially the flexibility and professionalism of the mechanical and electronic workshops as well as the accelerator and ion source staffs of JYFL is much appreciated. I would like to thank the office staff of the Department of Physics for all the help navigating in the system when living on the grants and for filtering the ever increasing amount of bureaucracy that administration brings upon us. Atomin pamaus deserves thanks for all the fun over the hours spent in the football field and my fellow Kenyans for the numerous exercise sessions for running and skiing. I would like thank all my friends for reminding that there is life outside the lab and my parents Heikki and Leena and my sister Anna for all the support and encouragement over the years.

Jyväskylä, December 2011

Antti Saastamoinen

Author

Antti Saastamoinen
Department of Physics
University of Jyväskylä
Finland

Supervisors

Prof. Dr. Juha Äystö
Department of Physics
University of Jyväskylä
Finland

Prof. Dr. Ari Jokinen
Department of Physics
University of Jyväskylä
Finland

Reviewers

Prof. Dr. Hans Fynbo
Department of Physics and Astronomy
University of Aarhus
Denmark

Prof. Dr. Olof Tengblad
Consejo Superior de Investigaciones Científicas
Instituto de Estructura de la Materia - Madrid
Spain

Opponent

Prof. Dr. Riccardo Raabe
Department of Physics and Astronomy
Katholieke Universiteit Leuven
Belgium

Abstract

Saastamoinen, Antti
Studies of $T_z = -3/2$ Nuclei of Astrophysical Interest
Jyväskylä: University of Jyväskylä, 2011, xiv + 96 pp.
Department of Physics, University of Jyväskylä, Research Report 9/2011
ISBN 978-951-39-4555-8 (printed)
ISBN 978-951-39-4556-5 (electronic)
ISSN 0075-465X

This thesis presents a summary of experimental studies of β-decaying $T_z = -3/2$ nuclei ^{23}Al and ^{31}Cl. The properties of these nuclei and the respective β-decay daughters, ^{23}Mg and ^{31}S, have an influence on the end products of ONe nova outbursts. The experiments were carried out at the IGISOL facility in the Accelerator laboratory of University of Jyväskylä and at the Cyclotron institute of Texas A&M University.

The mass excess of ^{23}Al was determined with Penning trap mass spectrometry by using the JYFLTRAP setup at IGISOL facility. The new mass excess is two orders of magnitude more precise than the previous value. A good agreement between theory and experimental values was found when applying the newly determined mass value to test the isobaric multiplet mass equation in the $A = 23, T = 3/2$ isobaric multiplet.

A β-decay setup was developed for the focal plane of momentum achromat recoil spectrometer in Texas A&M University. The study of the β-decay of ^{23}Al brought new information to the discrepancy between earlier measurements concerning the low energy protons emitted from ^{23}Mg. The new results completed data needed to determine the resonance strength of the astrophysically most relevant resonance in the ^{22}Na(p,γ)^{23}Mg reaction by completely indirect data. The study of the β-decay of ^{31}Cl confirmed the key findings of the previous studies. In addition, several states in ^{31}S, including the IAS of ^{31}Cl, were observed for the first time in a β-decay experiment. The results improve the energies and constrain the possible J^π of the states relevant for the ^{30}P(p,γ)^{31}S reaction.

A cryogenic ion guide was developed and the results of these tests are presented.

The successful tests have led to a full-scale prototype gas catcher for the future FAIR facility at GSI. In addition, it was demonstrated that going to cryogenic operation can reduce contaminant stable beam components observed in the standard operating conditions at the IGISOL facility.

Acknowledgments

This work would have not been possible without the generous financial support received from external sources. The author expresses deepest gratitude for the financial support from Jenny and Antti Wihuri foundation, the rector of the University of Jyväskylä; Vilho, Yrjö and Kalle Väisälä Foundation, Magnus Ehrnrooth Foundation, Emil Aaltonen Foundation and Waldemar von Frenckell foundation. The Graduate School in Particle and Nuclear Physics (GRASPANP) is acknowledged for financing travels to numerous schools and conferences.

This work has been supported by the EU within the 6th framework programme "Integrating Infrastructure Initiative — Transnational Access", Contract Number: 506065 (EURONS, JRA TRAPSPEC). The support from the Academy of Finland under the Finnish Centre of Excellence Programme 2006–2011(Project No. 213503, Nuclear and Accelerator Based Physics Programme at JYFL) is acknowledged.

Contents

List of Tables

List of Figures

1. Introduction

Nuclear astrophysics is a multidisciplinary science with the goal of explaining the origin of the chemical species, namely how the different elements are formed. The present understanding is that all the nuclei of every single atom are products of nucleosynthesis that has taken place at some stage during life-time of the universe. Only the very lightest elements –hydrogen, helium and lithium– are thought to have been synthesized in the big-bang-nucleosynthesis. To explain the formation of any heavier elements, other nuclear-reaction-based mechanisms have to take place.

Nucleosynthesis pathways in stellar environments depend on the seed nuclei and their properties as well as the physical parameters of the star. Thus the understanding of the dynamics of stellar phenomena requires various experimental and theoretical inputs from nuclear physics. In explosive nucleosynthesis scenarios, such as classical novae, the nucleosynthesis takes place among short-lived nuclei. To study the properties of these nuclei they have to be produced in sufficient quantities and as pure as possible.

In this thesis isotope separation on-line and in-flight techniques were used to produce high quality samples for the experimental studies. Precise and selective tools were used to study nuclei of astrophysical interest: the mass of ^{23}Al was determined by use of Penning trap mass spectrometry and the properties of excited states of ^{23}Mg and ^{31}S were studied through β-decay of ^{23}Al and ^{31}Cl, respectively. Part of the work has been carried out at the Accelerator laboratory of the Department of Physics of the University of Jyväskylä in Jyväskylä, Finland and part at the Cyclotron institute of Texas A&M University in College Station, Texas.

The outline of this thesis is as follows. In chapter 2, relevant nuclear physics concepts and brief introduction to related astrophysics is given. Chapter 3 presents the methods of producing the studied nuclear samples and chapter 4 explains the experimental techniques used in probing the properties of these nuclei. The results of the experiments are given and the attached publications summarized in chapter 5. Chapter 6 gives conclusions from the present work and provides an outlook for further studies.

This thesis is based on the following enclosed publications that are already published

or submitted for publication:

I **Mass of ^{23}Al for testing the isobaric multiplet mass equation**
A. Saastamoinen, T. Eronen, A. Jokinen, V.-V. Elomaa, J. Hakala, A. Kankainen, I. D. Moore, S. Rahaman, J. Rissanen, L. Trache, C. Weber and J. Äystö
Phys. Rev. C **80**, 044330 (2009)

II **Experimental study of β-delayed proton decay of ^{23}Al for nucleosynthesis in novae**
A. Saastamoinen, L. Trache, A. Banu, M. A. Bentley, T. Davinson, T. Eronen, J. C. Hardy, V. E. Iacob, M. McCleskey, B. Roeder, E. Simmons, G. Tabacaru, R. E. Tribble, P. J. Woods, J. Äystö
Phys. Rev. C **83**, 045808 (2011).

III **Study of excited states of ^{31}S through β-decay of ^{31}Cl for nucleosynthesis in ONe novae**
A. Saastamoinen, L. Trache, A. Banu, M. A. Bentley, T. Davinson, J. C. Hardy, V. E. Iacob, A. Jokinen, M. McCleskey, B. Roeder, E. Simmons, G. Tabacaru, R. E. Tribble, P. J. Woods and J. Äystö
(Proceedings of the 4th international conference on proton emitting nuclei and related topics) AIP Conf. Proc. **1409**, In press (2011).

IV **A setup for measuring low-energy decay products from implanted radioactive ion beams**
M. McCleskey, L. Trache, A. Saastamoinen, A. Banu, E. Simmons, B. Roeder, G. Tabacaru, T. Davinson, P. J. Woods, M. A. Bentley, R. E. Tribble, J. Äystö
To be submitted to Nucl. Instrum. Meth. in Phys. Res. A

V **Characterization of a Cryogenic Ion Guide**
A. Saastamoinen, I. D. Moore,M. Ranjan, P. Dendooven, A. Popov, K. Peräjärvi, H. Penttilä, J. Äystö
Submitted to Nucl. Instrum. Meth. in Phys. Res. A

VI **Cryogenic helium as stopping medium for high-energy ions**
S. Purushothaman, P. Dendooven, I. Moore, H. Penttilä, J. Ronkainen, A. Saastamoinen, J. Äystö, K. Peräjärvi, N. Takahashi, K. Gloos
Nucl. Instrum. Meth. in Phys. Res. B **266**, 4488 (2008).

VII **High-precision mass measurement of ^{31}S with the double Penning trap JYFLTRAP improves the mass value for ^{32}Cl**
A. Kankainen, T. Eronen, D. Gorelov, J. Hakala, A. Jokinen, V. S. Kolhinen,

M. Reponen, J. Rissanen, A. Saastamoinen, V. Sonnenschein, and J. Äystö
Phys. Rev. C **82**, 052501(R) (2010)

The author has participated in the setting up and operation of all the experiments described in the above publications. Especially for work described in technical publications IV,V,VI the author has contributed as technical workforce ranging from CAD and machine shop work to data interpretation and analysis. The author is the main writer of publications I–III and a major contributor in publications IV, V. The author has partially analyzed data for publications I,V and fully responsible for analysis of the data presented in publications II and III.

2. Theoretical Background

2.1. Nuclear Physics

An atomic nucleus has a total of $A = N + Z$ nucleons where N is the number of neutrons and Z the number of protons. Describing such an object in detail with all mutual interactions needed would require a massive number of parameters. However, the general behavior of a nucleus can be understood with a limited number of static and dynamic parameters that describe it as a single entity [1]. The key parameters of nuclei from the point of view of nuclear astrophysics are energy (mass), spin, parity of the nuclear state as well as the life-time and decay modes.

2.1.1. Nuclear Masses

Assembling the N neutrons and Z protons together as a nucleus releases the so-called binding energy B such that $B = (N \cdot m_n + Z \cdot m_p - [M(N,Z) - Z \cdot m_e])\, c^2$, where $M(N,Z)$ is the atomic mass of the nucleus and $m_{n,p,e}$ are the masses of the neutron, proton and electron, respectively. As nuclei exist rarely as bare entities stripped from electrons in the laboratory environment, but rather as ions or atoms, the masses are usually treated as atomic masses. Nuclear mass $m(N,Z)$ can be calculated from atomic mass with $m(N,Z) = M(N,Z) - Z \cdot m_e + B_e/c^2$, where B_e is the binding energy of all electrons. A widely used and convenient notation is the so-called atomic mass excess Δ which is defined as $M(N,Z) = A \cdot m_u + \Delta/c^2$, with $\Delta = 0$ for ^{12}C. The latest evaluations of atomic masses and atomic mass excesses can be found from Refs. [2–4]. The nuclear binding energy is a relatively large fraction of the mass-energy of the whole system. Studying the overall trend of the binding energy per nucleon as a function of nuclear mass number reveals that the maximum binding energy occurs at Fe/Ni ($A \sim 60$) region and that the overall trend is fairly constant apart from the very lightest nuclei. This general behavior can be understood e.g. with a so-called semi-empirical mass formula [1].

The importance of atomic masses arises from the fact that they define the energy budget of the reaction processes. One of the most important mass derivatives is the

reaction Q-value – the mass energy difference of the initial and final states:

$$Q = (M_i - M_f) \cdot c^2 = \Delta_i - \Delta_f. \tag{2.1}$$

A reaction with a positive Q-value releases energy and can occur without external energy input. Another important derivative of atomic masses is the separation energy, defining the amount of energy needed to remove a nucleon (n or p) or a group of nucleons (e.g. two or more protons, an α-particle) from a given nucleus. Relevant to this work is the proton separation energy, S_p, defined as:

$$S_p(A, Z) = (-M(A, Z) + M(A-1, Z-1) + M_H) \cdot c^2 = -Q_p, \tag{2.2}$$

where $M(A, Z)$ and $M(A-1, Z-1)$ are again atomic masses of the given nuclei, and M_H is the atomic mass of hydrogen. The nuclear states above this energy threshold are unbound against proton emission. Proceeding from stable nuclei towards more proton rich nuclei decreases the S_p. Eventually, with large enough proton excess, the ground states of nuclei lie beyond the line where $S_p = 0$ and are unbound against proton emission. This line is called the proton drip-line.

2.1.2. Nuclear Shell Model

The nuclear shell model is one of the most successful ways to describe an atomic nucleus. The treatment is analogous to the theory of atomic electrons. As the name implies, in this model, protons and neutrons occupy shells in accordance with the Pauli exclusion principle. In the shell model, the nucleons are described as interacting in an average potential where only one or few nucleons are defining the properties of a given nucleus, while the rest are forming an inert "core". The nucleon(s) defining the properties are called valence nucleon(s) occupying a valence shell while the set of shells that are used in the description of a given nucleus is called the valence space [1, 5].

The main characteristics of the shells, namely large gaps at certain "magic numbers", arise from solving the Schrödinger equation for a suitable potential with an added spin-orbit interaction [6]. The magic shells occur when the number of protons or neutrons is 2, 8, 20, 28, 50, 126 and 184 and can be observed experimentally e.g. when plotting two-neutron or two-proton separation energies versus the mass number A [3]. The magic nuclear numbers appear also as the difference between the best fit of the semi-empirical mass formula to the observed nuclear binding energies.

The nuclei studied in this work, ^{23}Al ($Z = 13, N = 10$) and ^{31}Cl ($Z = 17, N = 14$), are both in the so-called *sd*-shell. The *sd*-shell consists of the three shells ($0d_{5/2}, 1s_{1/2}, 0d_{3/2}$) between the magic shell gaps at $Z = 8$ and 20. In the shell model picture the orbital which the valence nucleon occupies defines the spin and parity of the whole nucleus. Therefore ^{23}Al is expected to have a ground state spin-parity $J^{\pi}_{g.s.} = \frac{5}{2}^{+}$ and ^{31}Cl $J^{\pi}_{g.s.} = \frac{3}{2}^{+}$, corresponding to the valence proton in the $d_{5/2}$ and $d_{3/2}$ orbitals, respectively.

2.1.3. Isospin

Protons and neutrons can also be described as two different states of the same entity called the nucleon [7]. In the isospin formalism, the nucleons are separated by having a different z-projection (labeled as T_z or T_3) of the isospin quantum number (T). The proton is assigned with $T_3 = -\frac{1}{2}$ and the neutron with $T_3 = +\frac{1}{2}$. As a mathematical concept, isospin is analogous to angular momentum and the T_3 of a nucleus with N neutrons and Z protons is the sum of individual nucleons: $T_3 = \frac{1}{2}(N - Z)$ and $T_3 = -T, -T + 1, -T + 2, \ldots, T$.

If there are no charge-dependent nucleon-nucleon interactions and in the absence of the electromagnetic interaction, these sub-states are degenerate, i.e. they have same energy. The states in the same isobar (same A) with the same T form a multiplet where the $2T + 1$ members have different T_3 projection. These are called isobaric analogue states (IAS). For example, the $A = 23, T = \frac{3}{2}$ multiplet, as illustrated in Fig 2.1, has four states, each in a different nucleus, with identical structure having $T_3 = \pm\frac{1}{2}, \pm\frac{3}{2}$. Of these, the $T_3 = \pm\frac{1}{2}$ members are excited states and $T_3 = \pm\frac{3}{2}$ are ground states of the respective nuclei. In reality the states are not degenerate in energy but differ by the proton-neutron mass difference, the Coulomb interaction between protons and a small deviation from charge symmetry in the nuclear force. [1,5,8]

2.1.4. Isobaric Multiplet Mass Equation

It can be shown that the mass excesses of the $2T + 1$ nuclear states belonging to a given isospin multiplet are related with the so-called Isobaric Multiplet Mass Equation (IMME),

$$M(A, T, T_3) = a(A, T) + b(A, T)T_3 + c(A, T)T_3^2. \tag{2.3}$$

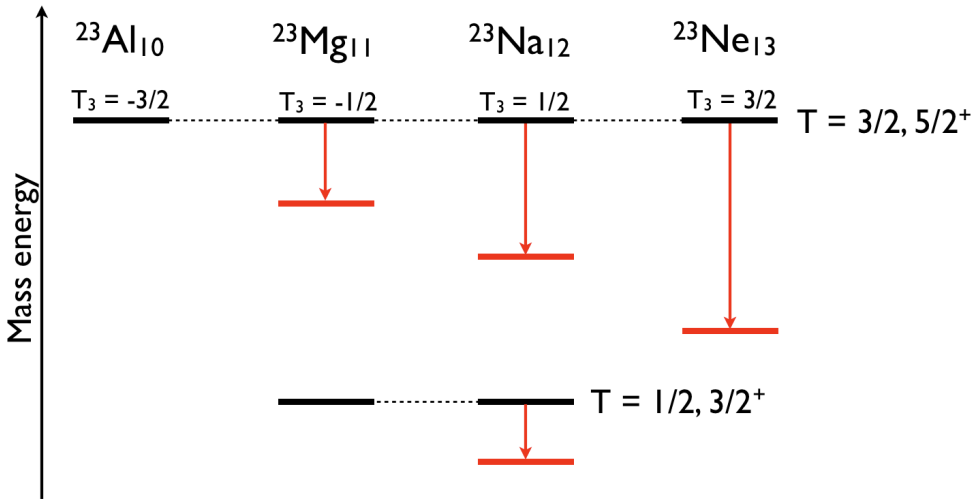

Figure 2.1: A schematic of the $A = 23$ isobaric multiplet. The black lines illustrate the situation in the absence of any charge-dependent nucleon-nucleon and electromagnetic interactions: the members of the upper $T = \frac{3}{2}$ quadruplet as well as the $T = \frac{1}{2}$ doublet are degenerate. The red lines and arrows indicate how the situation changes when charge-dependent forces are taken into account.

This explicit form of the IMME is attributed to Wigner [9], based on the work on nuclear electrostatic energies described in Refs. [10–12]. The mathematical formalism in the context of Coulomb energies and masses of isobaric analogue states (IAS) is discussed in detail in Refs. [13, 14]. Here the basic assumption is that any charge-dependent effects and the Coulomb force between the nucleons are of two-body nature, i.e. they are of tensorial rank two or less in isospin space and they can be treated by first-order perturbation theory. Possible higher-order terms (dT_3^3 or higher) may arise, for example, if second-order perturbation theory has to be used or if there is isospin mixing between the isobaric analogue state and neighboring states [15].

The IMME is a local mass model that can be used to predict energies of the isobaric analogue states in regions where experimental data are lacking. Applications include probing both excitation energies and ground state masses of nuclei, e.g. along the rp-process path and the location of the proton drip line. The IMME parameters are also applied to improve shell model calculations for theoretical corrections needed in testing the unitarity of the CKM matrix [16, 17]

2.1.5. β-decay

β-decay is a weak interaction process where a neutron transforms into a proton, emitting an electron and an anti-neutrino (β^--decay) or a proton transforms into a neutron, emitting a positron and a neutrino (β^+-decay). A third process, competing with the β^+-decay is called electron capture (EC), where the nucleus captures an electron from the inner orbitals of the atom, emitting an x-ray and a neutrino. Positron emission can occur only when the Q-value is high enough ($> 2 \cdot m_e = 1022$ keV) and it starts to dominate over EC with increasing Q-values. The Q-values for these processes (with atomic masses) are:

$$Q_{\beta^-} = [M(A,Z) - M(A,Z+1)] \cdot c^2 \quad (2.4)$$

$$Q_{\beta^+} = [M(A,Z) - M(A,Z-1)] \cdot c^2 - 2 \cdot m_e, \quad (2.5)$$

$$Q_{EC} = [M(A,Z) - M(A,Z-1)] \cdot c^2 - B_e, \quad (2.6)$$

where B_e is the binding energy of the captured electron. The energy released in the decay is shared among the daughter nucleus and the leptons and is transferred mostly to the leptons. As β-decay is three-body process, the resulting electron/positron spectrum is continuous, with $E_{e^\pm,max} = Q_{\beta^\pm}$.

β-decays are classified by the orbital angular momentum (l) taken away by the final state leptons. When the leptons are emitted with $l = 0$, the processes are called allowed β-decays and in other cases (i.e. $l > 0$) the processes are called forbidden β-decays. In reality the latter is just a naming convention, the decays are not forbidden but greatly suppressed when compared to allowed decays. In the following, only allowed β-decays are discussed. Allowed β-decays are categorized further to Fermi [18] and Gamow-Teller [19] type transitions by the coupling of the spins of the final state leptons. In Fermi-type transition the spins of the leptons are coupled to $S = 0$ and in Gamow-Teller-type transitions to $S = 1$. As the parity π of a nuclear state is $\pi = (-1)^l$, then due to conservation of parity the initial and final states have the same parity in allowed β-decay. These selection rules are summarized in table 2.1.

In the lowest order approximation of allowed β-decay, only two real coupling constants of the weak interaction are needed. These are the vector coupling constant (G_V) and axial-vector coupling constant (G_A) of the charge current. As both interactions can contribute at the same time, the transition rate of the decay $\lambda \propto G_V^2 \langle M_F \rangle^2 + G_A^2 \langle M_{GT} \rangle^2$. Here $\langle M_F \rangle$ and $\langle M_{GT} \rangle$ are the Fermi and Gamow-

Table 2.1: Selection rules of allowed nuclear β-decay.

Type of transition	$\Delta J = \lvert J_i - J_f \rvert$	$\pi_i \pi_f$	log ft [20, 21]
Fermi	0	+1	3.0 - 3.6
Gamow-Teller	1 ($J_i = 0$ or $J_f = 0$)	+1	2.8 - 10.8
Gamow-Teller	0,1 ($J_i > 0, J_f > 0$)	+1	2.8 - 10.8

Teller matrix elements, respectively. In isospin formalism, the conversion of proton to neutron (or vice versa) is handled by the raising/lowering operator $\boldsymbol{t}_\pm$ (changes the isospin projection T_3) and thus it is present in both types of matrix elements. In the approximation of the allowed decay, the vector part of the interaction is reduced to the unit operator $\mathbf{1}$ and the vector-axial part is reduced to the spin operator $\boldsymbol{\sigma}$ [5, 22].

In Fermi-type decay only T_3 changes. The square of the Fermi matrix element can be expressed as

$$\begin{aligned} \langle M_F \rangle^2 &= \frac{1}{2J_i + 1} \sum_{M_i M_f} | < J_f M_f T_f T_{3,f} | \mathbf{1} \sum_{k=1}^{A} \boldsymbol{t}_\pm(\boldsymbol{k}) | J_i M_i T_i T_{3,i} > |^2 \\ &= T(T+1) - T_{3,i} T_{3,f}, \end{aligned} \tag{2.7}$$

where the simple expression is true if the initial and final states are analogue states and T is a good quantum number [22]. It is not possible to get such a simple expression for the Gamow-Teller matrix element (in terms of T and T_3 only) because both spin and isospin operators are involved. The square of the Gamow-Teller matrix element is defined as:

$$\begin{aligned} \langle M_{GT,\pm} \rangle^2 &= \frac{1}{2J_i + 1} \sum_{m M_i M_f} | < J_f M_f T_f T_{3,f} | \sum_{k=1}^{A} \boldsymbol{\sigma_m}(\boldsymbol{k}) \boldsymbol{t}_\pm(\boldsymbol{k}) | J_i M_i T_i T_{3,i} > |^2 \\ &= 6(2j_f + 1) \begin{Bmatrix} \frac{1}{2} & \frac{1}{2} & 1 \\ j_i & j_f & l \end{Bmatrix}, \end{aligned} \tag{2.8}$$

where the latter form is a very simple single-particle estimate acquired by assuming that only one nucleon is active with an inert $J = 0, T = 0$ core [22].

A β-decay transition with branching $b_{\beta,i}$ has a partial half-life $t_{1/2,i} = \frac{t_{1/2}}{b_{\beta,i}}$, where $t_{1/2}$ is the total half-life of the nucleus. The partial transition rate (probability) of a given decay is connected to the half-life via the relation:

$$\lambda_i = \frac{\ln 2}{t_{1/2,i}}. \tag{2.9}$$

All the partial transition rates sum up to the total transition rate $\lambda = \sum_i \lambda_i$, yielding also the total half-life of the nucleus. In Fermi's theory of β-decay the decay-causing interaction is taken as a small perturbation and the transition rate can be expressed with Fermi's Golden Rule of time-dependent perturbation theory:

$$\lambda = \frac{2\pi}{\hbar} \left|V_{fi}\right|^2 \frac{dn}{dE_f}, \tag{2.10}$$

where $\frac{dn}{dE_f}$ is the density of final states and $|V_{fi}|$ is the matrix element of the transition operator [1,5,22]. The total transition rate is obtained by integrating the above expression over the spectrum of electron (positron) energy, leading to an expression for the comparative half-life, or ft-value:

$$\begin{aligned} f_0 t(1+\delta_R) &= \frac{\kappa}{G_V^2 \left\langle M_F \right\rangle^2 (1-\delta_C) + G_A^2 \left\langle M_{GT} \right\rangle^2}, \\ f_0 &= \begin{cases} f_0^-, & \text{for } \beta^- \text{ decay}, \\ f_0^+ + f_0^{EC}, & \text{for } \beta^+/\text{EC decay}, \end{cases} \end{aligned} \tag{2.11}$$

where $\left\langle M_F \right\rangle^2$ and$\left\langle M_{GT} \right\rangle^2$ are the Fermi and Gamow-Teller matrix elements, respectively. The radiative and isospin-symmetry-breaking corrections δ_R and δ_C are of the order of 1% [16] and are often left out from the expression. For the coupling constants one has the relation: $G_A/G_V = -1.2694(28)$ [23] and the constant $\kappa/G_V = \frac{2\pi^3\hbar^7 ln2}{m_e^5 c^4 G_F^2} = 6144(2)$ s, for which the numeric value is obtained from the super-allowed $0^+ \to 0^+$ transitions [24].

The $f_0^{\mp,EC}$ denote the corresponding phase-space factors, which can be acquired from calculations that are tabulated e.g. in Ref. [25]. For light nuclei ($Z_i < 40$) the EC phase space factor can be approximated with $f_0^{EC} \approx 2\pi(\alpha Z_i)^3[(1-\frac{1}{2}(\alpha Z_i)^2) + E_0]^2$ [5], where α is the fine structure constant. A widely used analytical approximation for $f_0^{\mp}$ is so-called Primakoff-Rosen approximation [5,26]:

$$f_0^{\mp} \approx \frac{1}{30}(E_0^5 - 10E_0^2 + 15E_0 - 6)F_0^{(PR)}(\pm Z_f), \tag{2.12}$$

where $E_0 = \frac{E_i - E_f}{m_e c^2}$ and $F_0^{(PR)}(\pm Z_f)$ is the approximation for the Fermi function. Due to the strong E^5 dependence in the available phase space in the approximation above, half-lives of different β-decaying nuclei vary over several orders of magnitude. For this reason ft-values are given mostly as $\log_{10} ft$. The ft-values can be used for rough classification of the β-decays, but there is a considerable overlap among the different types as seen in Refs. [20, 21]. The transitions between isobaric analogue states are among the fastest decays with very small ft-values (see table 2.1).

2.1.6. β-delayed proton and γ decays

A β-decaying nucleus feeds states in its daughter nucleus as shown in Fig. 2.2. Under the proton separation threshold S_p of the daughter, the de-excitation happens only via γ-emission. In γ-decay, a photon with energy $E_\gamma = E_i - E_f - E_{rec}$ is emitted. For low energy γ-decays, the energy of the recoiling nucleus $E_{rec} = \frac{E_\gamma}{2Mc^2}$ is by far smaller than the typical experimental uncertainties and thus is negligible. In γ-decay the angular momentum L carried away by the photon must abide by the selection rule $|J_i - J_f| \leq L \leq J_i + J_f$ and it cannot be zero. γ-decay does not change parity in an electric transition with $L = even$ and in a magnetic transition with $L = odd$. The parity changes in electric transiton if $L = odd$ and in magnetic transition if $L = even$.

Above S_p proton emission starts to compete with γ emission. The proton emission probability increases with excitation energy and the high-lying states decay basically only via proton emission whereas the states near threshold may have only a small proton branching due to competing γ-decays. Various β-delayed particle emission modes in proton-rich nuclei are reviewed in detail e.g. in Refs. [27, 28].

Angular momentum conservation limits the angular momentum of the emitted proton, l_p, to the condition: $|J_i - J_f| - 1/2 \leq l_p \leq |J_i - J_f| + 1/2$. Furthermore, the parity of the final state in the proton daughter must be $\pi_f = (-1)^{l_p} \cdot \pi_i$ and the isospin has to be conserved: $T_f = T_p + T_i$. The probability per unit time for the decay of a level (or in the inverse process: formation of a resonance) is called the partial width Γ_i and is directly proportional to the partial decay rate λ_i. The partial width $\Gamma_{\lambda c}$ of a level λ through a channel c is expressed as:

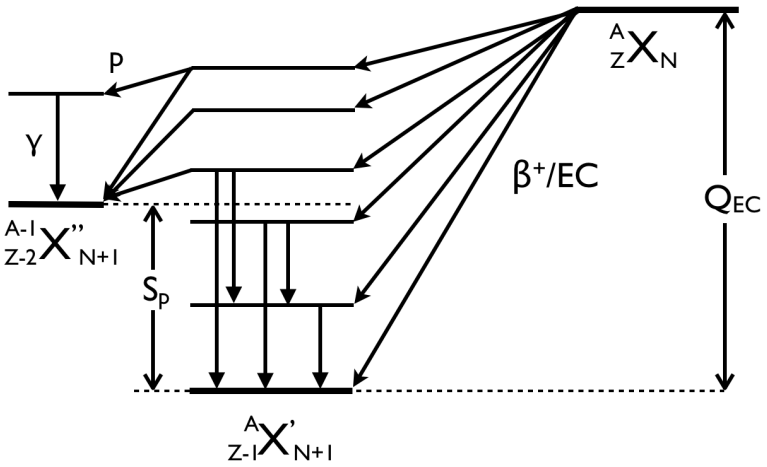

Figure 2.2: Schematic of β-delayed decays. β-decay of ${}^{\mathrm{A}}_{\mathrm{Z}}\mathrm{X}_{\mathrm{N}}$ feeds states in its daughter nucleus ${}^{\mathrm{A}}_{\mathrm{Z}-1}\mathrm{X}'_{\mathrm{N}+1}$, called an emitter in the case of proton-emitting nuclei. The proton emission feeding states in the proton daughter ${}^{\mathrm{A}}_{\mathrm{Z}-2}\mathrm{X}''_{\mathrm{N}+1}$ can occur from states above S_p, whereas states below decay only by γ-emission.

$$\Gamma_{\lambda c} = 2\frac{\hbar}{\mu R^2} P_c C^2 S \theta_{pc}^2, \tag{2.13}$$

where μ is the reduced mass of the proton-proton daughter (or proton-target) system and $R = a(A_p^{1/3} + A_d^{1/3})$ is the interaction radius, with $a = 1.2 \ldots 1.3$ fm. P_c is the barrier penetrability factor defining the probability that the proton will tunnel through the Coulomb and angular momentum barriers. C^2S is a product of the square of the isospin Clebsch-Gordan coefficient (C^2) and the single-particle spectroscopic factor(S). It defines the probability that nucleons can be found in the final state configuration. θ_{pc} is the single-particle partial width, giving the probability that a single nucleon is found at the nuclear boundary [29, 30].

The energy available for proton emission is $E = E^* - S_p$, where E^* is the excitation energy of the level in the emitter. The intensity of the emitted protons from an initial state i in emitter to a final state f in the proton daughter is:

$$I_p^{if} = I_\beta^i \frac{\Gamma_p^{if}}{\Gamma_p^i + \Gamma_\gamma^i}, \tag{2.14}$$

where $\Gamma^{i}_{p,\gamma} = \sum_f \Gamma^{if}_{p,\gamma}$ are the total proton and γ partial widths, respectively [31]. If the level life-time τ is known, the latter can be acquired directly from the Heisenberg uncertainty principle giving $\Gamma_\gamma = \hbar/\tau$. In general, the intensities of the lines in a proton spectrum depend on the A, Z of the preceding nucleus and depend greatly on the mass region due to different level densities in the available energy window $(Q_{\beta^+} - S_p)$ [27]. Emission of very low energy protons from excited states near S_p are hindered due to the Coulomb and angular momentum barriers and due to competition with γ emission. The proton emission becomes easier with increasing energy and being a strong interaction process, it wins over the slower electromagnetic interaction γ emission. At higher energies the proton emission intensity starts to decrease due to the fact that β-feeding of the states in the upper end of the available energy window are reduced by the available phase space (Eq. 2.12).

Nuclei with $T_Z = -\frac{3}{2}, A = 4n + 1$ have been observed to be particularly favorable for β-delayed proton emission [31] and the lowest $T = \frac{3}{2}$ state is usually located inside the $(Q_{\beta^+} - S_p)$ window making proton emission from the IAS possible. In these nuclei the super-allowed decay from the precursor, feeding the IAS in the emitter has been observed from $n = 2$ to 36 [27]. However, the proton emission is isospin-forbidden due to energetically available states in a $T = 0$ proton daughter.

For example, the IAS of the ground state of ^{23}Al in ^{23}Mg has $J^\pi = 5/2^+, T = 3/2$ and it is unbound against proton emission only slightly above 200 keV. As the proton emission could lead only to the ground state of ^{22}Na having $J^\pi = 3^+, T = 0$ it is allowed by angular momentum conservation, but this process is forbidden by the isospin conservation. Proton emission from the IAS in ^{23}Mg would thus require a nearby $T = 1/2$ state with same J^π to allow the existence of isospin-mixing matrix elements in the Hamiltonian describing the system [32–35]. Observation of decays involving forbidden proton emission yields important information about isospin-mixing in light nuclei [33, 34].

2.2. Astrophysics

2.2.1. Explosive hydrogen burning in classical novae

The astrophysical aspects of this work relate to close binary stellar systems called classical novae, illustrated in Fig. 2.3. Present understanding is that classical novae occur in closely interacting binary systems, where hydrogen-rich material from a low-mass main-sequence star is accreted on to a white dwarf. The main-sequence

companion has reached the point at which its outer layers are expanding and fill the Roche lobe leading to an overflow. At this point the hydrogen-rich matter can come under the gravitational influence of the white dwarf, forming an accretion disc around it and finally falling onto the surface. As the accretion of matter proceeds, temperature and density in the surface layer rises until thermonuclear runaway (TNR) occurs releasing the accreted and synthesized matter ($M \sim 10^{-4} \ldots 10^{-5} M_{\odot}$) into the interstellar medium. As the TNR occurs in the surface it does not destroy the white dwarf in the explosion (as is the case of type Ia supernova) and they are thought to recur every $10^4 - 10^5$ years. Based on observations from other galaxies, about 30 nova outbursts per year per galaxy are expected to happen, but only about 5 are observed in our galaxy due to fact that interstellar gas etc. absorbs and distorts the observations [30, 36–40].

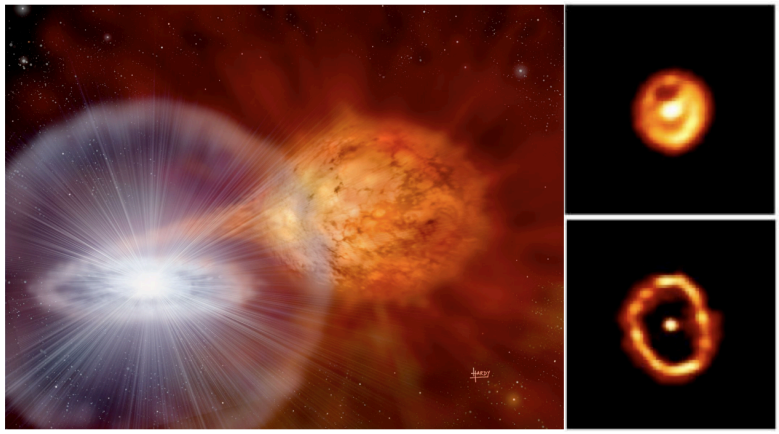

Figure 2.3: Artist's illustration of a closely interacting binary system [41]. The two panels on the right show the Hubble space telescope observations of Nova Cygni 1992. The upper image is taken 467 days after the explosion and the lower seven months after the top frame showing clearly the expanding gas envelope from the nova outburst [42].

Classical novae are classified by the major composition of the white dwarf: the two types are CO and ONe novae, providing a different profile of seed nuclei for the nucleosynthesis. As there is basically no leakage from the CNO region to higher masses at typical nova temperatures (0.1-0.4 GK), larger amounts of end products with $A \geq 20$ require an ONe white dwarf. In classical novae, nucleosynthesis proceeds close to stability mostly via proton or α-capture reactions and β-decays up to its endpoint in the $A \sim 40$ region, as illustrated in Fig. 2.4. In the early stages of the burst, the nucleosynthesis occurs mainly via proton-proton chains (pp-chains) and

cold CNO cycles and with increasing temperature it proceeds to hot CNO cycles. In ONe novae, nucleosynthesis at lower temperatures also includes so-called NeNa and MgAl (pseudo-)cycles. In case the β-decay half-life of a nucleus in the path of nucleosynthesis is comparatively long, a waiting point or a "bottleneck" for the the process can occur. It is worth noting that the majority of the energy production of the outburst is generated by the reactions of the CNO cycles and thus the reactions at the higher mass region are interesting for their influence on the final abundance pattern. [30, 38–40, 43]

An understanding of the dynamics of these outbursts and of the nucleosynthesis fueling them is crucial in testing our modeling of the dynamics of stellar phenomena in general. As classical novae are relatively frequent phenomena in the galaxy (X-ray bursts are the most frequent and novae the second most frequent) being observed almost throughout the whole electromagnetic spectrum they make good test beds for the theoretical models. It is believed that novae could become the first type of explosive process for which all the nuclear input to the nucleosynthesis calculations is based on experimental data [38, 39, 43].

2.2.2. Thermonuclear Reaction Rates

The astrophysical reaction rate for a charged particle-induced reaction, in units of ($\mathrm{cm^3 mol^{-1} s^{-1}}$) is given by:

$$N_a \langle \sigma \nu \rangle = \sqrt{\frac{8}{\pi \mu}} \frac{N_A}{(kT)^{3/2}} \int_0^\infty E \sigma(E) e^{-\frac{E}{kT}} dE \tag{2.15}$$

where N_A is the Avogadro number, $\mu = \frac{m_p m_T}{m_p + m_T}$ is the reduced mass of the projectile (p) and target (T), $\sigma(E)$ the reaction cross section and k is the Boltzmann constant [30, 36]. The most relevant energy region in a stellar environment, such as classical nova, for a charged particle-induced reaction to occur is called the Gamow window. It is product of two contributions: First of all, the kinetic energy of the fusing particles depends on the temperature and energy of the particles, distributed as in a Maxwell-Boltzmann distribution (P(E) dE = $\frac{2}{\sqrt{\pi}}(kT)^{-3/2}\sqrt{E}e^{-E/kT}$ dE). The second factor is the (s-wave) Coulomb barrier penetration probability at energies lower than the barrier height, given by the barrier penetrability factor $e^{-2\pi\eta}$, where

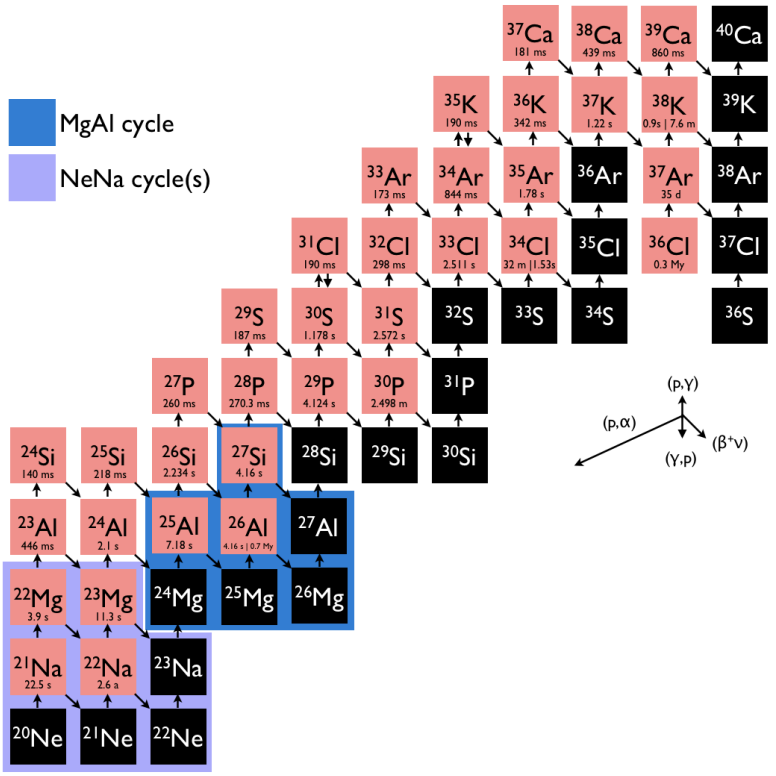

Figure 2.4: The major nuclear paths in the $A \geq 20$ region [44, 45]. The black boxes represent stable nuclei and the red boxes β-emitting nuclei.

$$2\pi\eta = 0.989534 Z_p Z_T \sqrt{\frac{1}{E}\frac{M_p M_T}{M_p + M_T}}. \tag{2.16}$$

The integrand in Eq. 2.15 has a maximum where the tails of the Maxwell-Boltzmann and barrier penetrability probabilities have maximal overlap, as illustrated in Fig. 2.5. This maximum corresponds to the Gamow peak. It can be approximated with a Gaussian distribution $exp(-\frac{3E_0}{kT})exp\left(-\frac{E-E_0}{\Delta/2}\right)^2$, where the Gamow energy and width E_0 and Δ, respectively, at temperature T_9 (T in GK) are defined as:

$$E_0 = \left[\left(\frac{\pi}{\hbar}\right)^2 (Z_p Z_T e^2)^2 \frac{\mu}{2}(kT)^2\right]^{\frac{1}{3}} = 0.1220 \left[Z_p^2 Z_T^2 \frac{M_p M_T}{M_p + M_T} T_9^2\right]^{\frac{1}{3}} \quad (2.17)$$

$$\Delta = \frac{4}{\sqrt{3}}\sqrt{E_0 kT} = 0.2368 \left(Z_p^2 Z_T^2 \frac{M_p M_T}{M_p + M_T} T_9^5\right)^{\frac{1}{6}}. \quad (2.18)$$

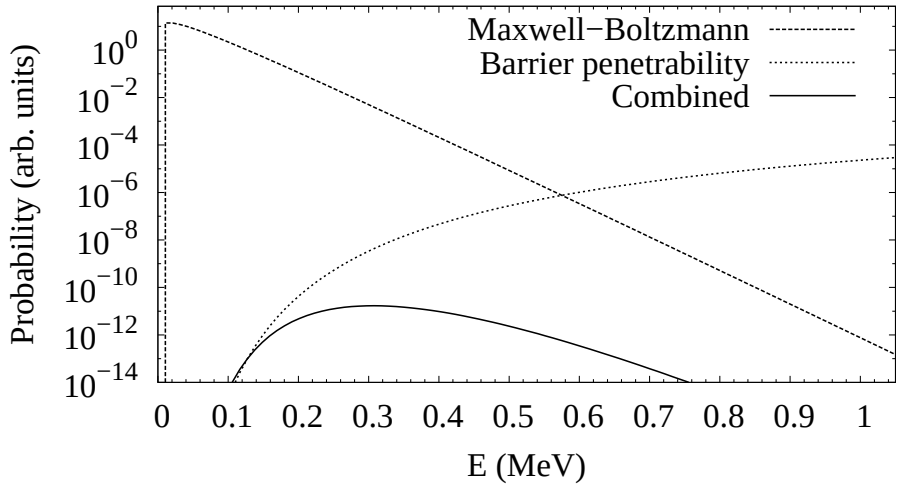

Figure 2.5: Gamow peak of the ^{22}Na(p,γ)^{23}Mg reaction. Shown are the probability distributions of the barrier penetrability ($\propto e^{-2\pi\eta}$), the Maxwell-Boltzmann distribution of the projectile energies ($\propto (kT)^{-3/2}\sqrt{E}e^{-E/kT}$) and the product of the two defining the Gamow peak. Notably the maximum of the Gamow peak is at $E_0 = 0.30$ MeV (Eq. 2.17), whereas the most probable projectile energy at the typical nova peak temperature ($T = 0.35$ GK) is only about 30 keV.

For a non-resonant reaction, the reaction cross-section varies smoothly in energy. The reaction rate for a non-resonant reaction, in other words a direct capture, with a constant S-factor can be approximated by replacing the Gamow peak with a Gaussian approximation (Eqs. 2.17,2.18) and applying necessary corrections, giving the following expression [30, 36]:

$$N_a \langle \sigma\nu \rangle = \left(\frac{4}{3}\right)^{\frac{3}{2}} \frac{\hbar}{\pi} \frac{N_A}{\mu Z_p Z_T e^2} S_{\text{eff}} \tau^2 e^{-\tau}, \quad (2.19)$$

in units of $\mathrm{cm^3 mol^{-1} s^{-1}}$, where $\tau = \frac{3E_0}{kT}$ and S_{eff} is the effective S-factor that can be determined numerically [30,36]. If the S-factor has a strong (but still smooth) energy dependence, and thus the Taylor expansion does not hold anymore, the reaction rate has to be obtained by numerical integration.

For capture reactions involving resonances the S-factor varies strongly in energy. The wave function of the tunneling particle has nodes inside the potential well and the astrophysical reaction rate is described by the resonant reaction rate. If the resonances are narrow and isolated the reaction rate is expressed as:

$$N_a \langle \sigma\nu \rangle = 1.5399 \cdot 10^{11} \left(\mu T_9\right)^{-3/2} \times \sum_i (\omega\gamma)_i e^{\left(-11.605 E_i / T_9\right)}, \tag{2.20}$$

in units of $\mathrm{cm^3 mol^{-1} s^{-1}}$, where μ is the reduced mass of the colliding nuclei in units of u, T_9 the temperature in GK, E_i the center of mass energy of the ith resonance in MeV and $\omega\gamma_i$ is the resonance strength of the ith resonance in MeV [30,36]. The resonance strength is defined as:

$$\omega\gamma = \frac{2J+1}{(2J_p+1)(2J_t+1)} \cdot \frac{\Gamma_p \Gamma_\gamma}{\Gamma_p + \Gamma_\gamma}, \tag{2.21}$$

where Γ_p, Γ_γ are proton and γ-widths of the state. Typically for low resonance energies when $\Gamma_p << \Gamma_\gamma$, the resonance strength depends only on the proton width, i.e. $\omega\gamma \approx \omega\Gamma_p$. If the intensities of the state are known the absolute proton width can be approximated from the γ-ray width simply as $\Gamma_p = \frac{I_p}{I_\gamma}\Gamma_\gamma$ with $\Gamma_\gamma = \frac{\hbar}{\tau}$.

2.3. Decay spectroscopy as a probe for astrophysically relevant states

The selectivity of β-decay and the following decays, especially proton emission, offer insight into the underlying nuclear structure of the daughter nucleus. In relatively light nuclei such as ^{23}Al and ^{31}Cl the β-decay feeds daughters with relatively low density of states and thus the proton peaks in the spectrum are well separated [27]. In combination with a simultaneously collected γ spectrum it is possible to pin down the properties of the emitting states and the pattern of the feeding β-decays. From the proton- and γ-decay data, the relative branching ratios can be determined and if the total number of parent nuclei is known, also the absolute branching ratios. The

nature of the β-transitions and the J^π of the emitting states can be deduced from determined log ft values. Of course β-decay itself does not give out all necessary details, but the full picture can be built with complementary data e.g. from reaction measurements.

In principle proton emission is the time-reversed process of proton capture. The probability for formation or decay of a resonance is described by the partial width $\Gamma_{\lambda c}$ given by Eq. 2.13 in section 2.1.6. As illustrated in Fig. 2.6, β-decay of a nucleus ${}^{\mathrm{A}}_{\mathrm{Z}}\mathrm{X}_{\mathrm{N}}$ feeds states in the proton emitter ${}^{\mathrm{A}}_{\mathrm{Z}-1}\mathrm{X}'_{\mathrm{N}+1}$ and further proton emission feeds states in the proton daughter ${}^{\mathrm{A}}_{\mathrm{Z}-2}\mathrm{X}''_{\mathrm{N}+1}$. In a resonant proton capture reaction the nucleus ${}^{\mathrm{A}}_{\mathrm{Z}-2}\mathrm{X}''_{\mathrm{N}+1}$ captures a proton forming a state in the compound nucleus ${}^{\mathrm{A}}_{\mathrm{Z}-1}\mathrm{X}'_{\mathrm{N}+1}$. This state can then decay either by proton emission back to the target nucleus and a free proton or by γ emission to the ground state and a new nucleus is synthesized. Allowed β-decay can be used to probe the astrophysically relevant states in the compound nucleus. For example, allowed β-decay of ^{23}Al feeds states with $\frac{3}{2}^+, \frac{5}{2}^+, \frac{7}{2}^+$ in ^{23}Mg and the s-wave protons ($l_p = 0$) in the resonant capture reaction $^{22}\mathrm{Na}(\mathrm{p},\gamma)^{23}\mathrm{Mg}$ are captured to states with $\frac{5}{2}^+, \frac{7}{2}^+$ in ^{23}Mg.

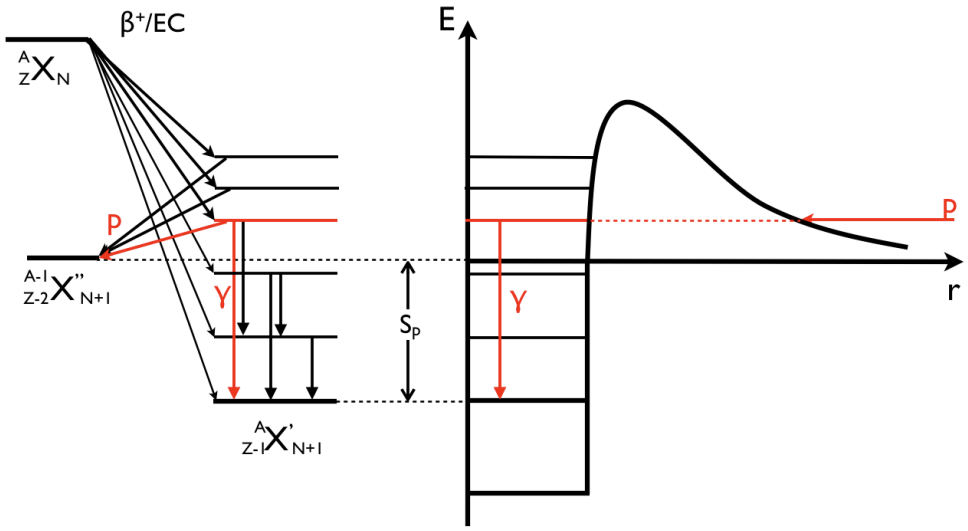

Figure 2.6: Schematic showing similarities between decay and capture reactions. As in Fig. 2.2, β-decay of ${}^{\mathrm{A}}_{\mathrm{Z}}\mathrm{X}_{\mathrm{N}}$ feeds states in the proton emitter ${}^{\mathrm{A}}_{\mathrm{Z}-1}\mathrm{X}'_{\mathrm{N}+1}$ and subsequent proton emission feeds states in the proton daughter ${}^{\mathrm{A}}_{\mathrm{Z}-2}\mathrm{X}''_{\mathrm{N}+1}$. In a resonant proton capture reaction, the nucleus ${}^{\mathrm{A}}_{\mathrm{Z}-2}\mathrm{X}''_{\mathrm{N}+1}$ captures a proton forming a state in the compound nucleus ${}^{\mathrm{A}}_{\mathrm{Z}-1}\mathrm{X}'_{\mathrm{N}+1}$.

Energetics of the two reaction mechanisms are rather similar and the most convenient frame of reference for both cases is the center-of-mass system (CMS). However it is worth noting that in literature, the results of the direct reaction measurements are usually given as the laboratory energy ($E_{p,lab}$) of the proton beam (e.g. in Ref. [46]) whereas in β-decay studies the proton energies are given as the emitted proton energy ($E_{p,decay}$) in the laboratory system (e.g. in Refs. [47, 48]). These two reported energies are related by:

$$E_{p,lab} = \left(\frac{m_p + m_R}{m_R}\right)^2 E_{p,decay}. \tag{2.22}$$

3. Production of Radioactive Ion Beams

Production methods of radioactive ion beams (RIB) are usually split into two main categories. The first is the so-called in-flight method and the second is the isotope separation on-line (ISOL) method. This categorization is illustrated in Fig. 3.1.

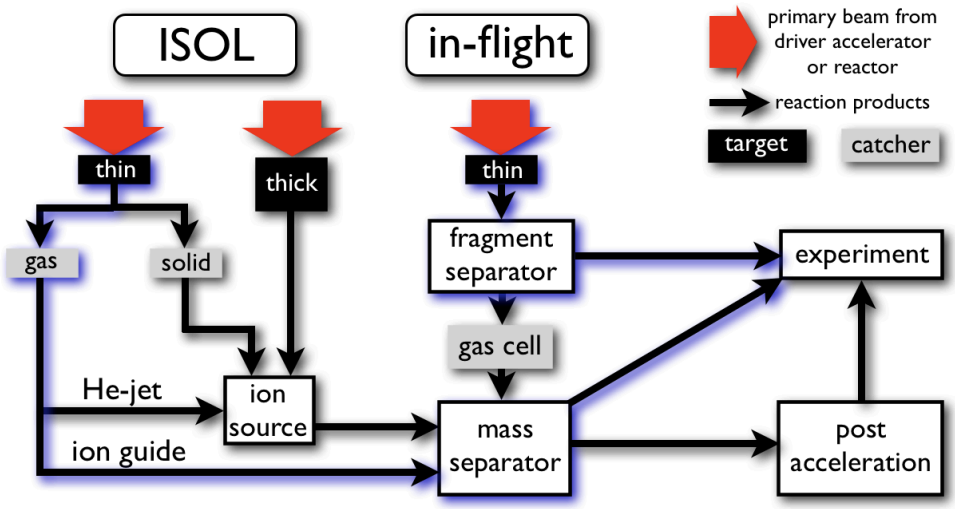

Figure 3.1: Description of production methods of radioactive ion beams, adapted from [49, 50]. The production methods used in this work are highlighted.

In the in-flight method, an energetic heavy ion beam impacts with a thin stationary target whereby reaction products are created via fusion, fission or fragmentation reactions. Due to the momentum gained from the primary beam, the reaction products have high energy (several MeV/u and upwards) when leaving the target. This makes the separation process fast as the flight time from the production target to the experimental setup is usually of the order of microseconds.

The traditional ISOL method is based on a thick stationary target, in which the target also works as the catcher (the target can be also thin, coupled to a solid catcher). The target-catcher is combined with an ion source, from where the reaction products

are extracted as a low energy (few tens of keV) secondary beam. Other variations of the thin target ISOL method are the He-jet and the ion guide method where the reaction products are thermalized in gas and then extracted either with or without an ion source. After the extraction from the gas cell (or ion source), the secondary beam is usually mass separated. It can also be post-accelerated before being delivered to the experiments. The ISOL method is slower than in-flight production as the delay time from the target to the experiment can be from milliseconds to several seconds.

The radioactive ion beams for the studies in this thesis were created using the ion guide isotope separation on-line (IGISOL) technique and by the in-flight method with a recoil spectrometer. In the following sections introductions to the used devices will be given.

3.1. Isotope Separation On-Line: IGISOL

3.1.1. The IGISOL method

The ion guide isotope separation on-line (IGISOL) method was developed in the Accelerator laboratory of the University of Jyväskylä in the early 1980's. The development of the method is described in detail in Refs. [49,51]. In the IGISOL method, a thin (typically a few mg/cm^2) target is bombarded by an energetic primary beam and the reaction products recoiling out from the target are stopped in a noble gas (usually He) with a typical pressure of a few hundred mbar. The highly-charged reaction products are thermalized through collisions with the noble gas atoms. The reaction products undergo charge exchange reactions and due to the high ionization potential of He, the majority of the reaction products end up into charge state of 1^+ before being flushed out of the stopping volume by gas flow. In the present system, the thermalized ions exiting from the gas cell are guided via a sextupole RF-electrode system (SPIG) [52] into a differentially pumped electrode system consisting of extraction and acceleration electrodes. The typical total acceleration potential used at IGISOL is 30 kV. The principle of the IGISOL method is illustrated in Fig. 3.2.

Using a thin instead of a thick target provides the IGISOL method a great advantage over traditional the ISOL method: the reaction products come out from the target with the momentum gained from the reaction with the primary beam instead of diffusing out from the target matrix. This makes the IGISOL method chemically non-selective. In principle, radioisotopes of any chemical element can be produced

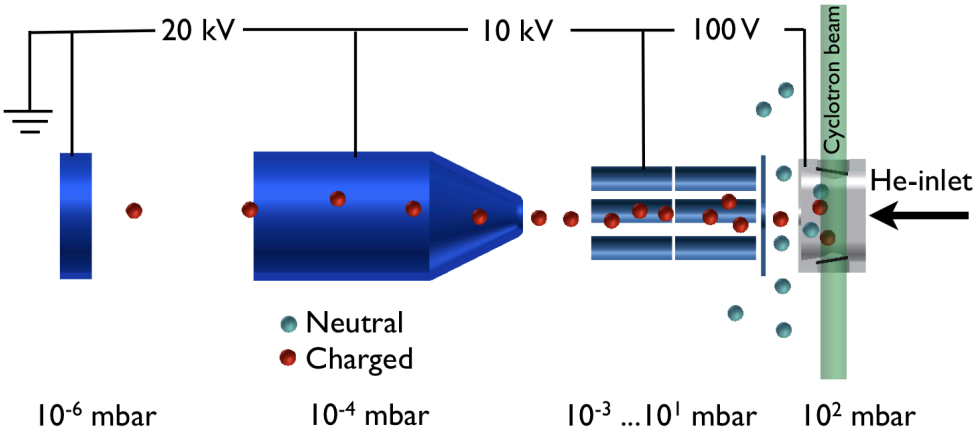

Figure 3.2: Schematic presentation of the IGISOL technique with typical high voltage and buffer gas pressures in different regions. As compared to the earlier systems [49, 51] the skimmer has been replaced by a sextupole ion guide [52] electrode system.

with short delay times. However, it is important to note, that possible impurities in the gas used for stopping can result in molecular formation with impurities, thus affecting the final yield. The IGISOL method is also relatively fast: sub-millisecond extraction times have been achieved with the small volume light-ion guide (whereas the traditional ISOL is usually in the ms range at best). On the other hand, the small size of the gas cell (a few cm^3 to few tens of cm^3), in addition to somewhat limited gas pressure, keeps the overall stopping efficiency of the most energetic reaction products relatively low. The highest reported total efficiency has been about 10%, but the usual is somewhere in the region of per mil to percent range. In most of the ion guides, the primary beam has to pass through the gas volume where it ionizes the stopping gas, increasing the probability of neutralization of the reaction products via electronic recombination and charge exchange reactions. It has been observed that the yields start to drop with increasing primary beam current. This so called "plasma effect" limits the amount of primary beam that can be used.

The IGISOL3 facility is illustrated in Fig. 3.3. The production target is located in the target chamber, from where the extracted and accelerated ions are guided forward and separated by their A/q ratio with a 55° dipole magnet with a typical mass resolving power (MRP) $\frac{M}{\Delta M} = 500$. After separation, the ions can be monitored at the electrostatic switchyard from where the beam is sent to different experiments. The yields of the activities produced with the IGISOL system are usually measured

in the focal plane by using a Si-detector setup (33% absolute efficiency from the geometry) or if needed, with a separate $\beta\gamma$-setup consisting of a 3π-scintillator, a HPGe detector and a vacuum-operated tape transport system. Figure 3.3 also illustrates one of the experimental beam lines housing a gas-filled radio-frequency quadrupole (RFQ) cooler-buncher [53] which is used to prepare samples for delivery to a collinear laser spectroscopy line and to the JYFLTRAP Penning trap setup [54].

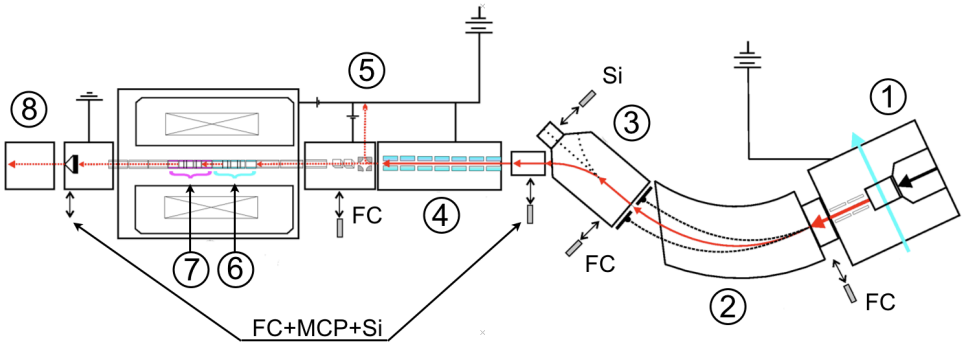

Figure 3.3: Schematic presentation of the IGISOL3 facility with beam lines relevant to this work. 1. Target chamber, see also Fig. 3.2. 2. 55° dipole magnet. 3. Electrostatic switchyard. 4. RFQ cooler/buncher. 5. Beam line to collinear laser spectroscopy. 6. Preparation trap. 7. Precision trap. 8. Post-trap setups. Beam diagnostics elements are labeled as FC (Faraday cup), MCP (micro-channel plate) and Si (Si-detector).

In the mass measurement of ^{23}Al, a light-ion fusion ion guide [55] was used to produce the studied isotopes by bombarding a self-supporting 4.3 mg/cm^2 $^{\text{nat}}$Mg target with 40 MeV protons from the K-130 cyclotron. The ions of interest were produced with the IGISOL method described above. The typical observed β-counting rate at the focal plane for $A = 23$ was 50 000 s^{-1} with a proton-beam intensity of 8–10 μA. The majority of the activity was identified to be ^{23}Mg, produced via ^{24}Mg(p,pn)^{23}Mg. The identification was done by a half-life measurement, giving a yield of about 150 000 ^{23}Mg ions/s. The yield of ^{23}Al activity, produced via ^{24}Mg(p,2n)^{23}Al, has been observed to be about 0.5% of the total activity produced [48], resulting in a yield of approximately 700 ^{23}Al ions/s.

3.1.2. Cryogenic Ion Guide Development

Requirements for converting a high-energy beam to a low-energy beam with higher quality are emerging for future facilities such as FAIR at GSI [56]. The low energy branch of the FAIR facility will be located after the superconducting projectile fragment separator (Super-FRS) [57] which provides radioactive ion beams with energies up to ∼GeV/u. Energy and range bunching [58] is used to slow down the high energy beam to 1 – 100 MeV/u, depending on the experimental section of the low energy branch. Even lower energies are needed e.g. for laser spectroscopy and ion trap experiments, where the required beam energy is few tens of keV with an energy spread $\sim$ 1 eV and and emittance of a few π mm rads [59].

The conventional approach to this transformation has been using large volume, high purity gas cells [60,61]. The use of cryogenic helium as a stopping medium has been proposed and tested as a technically simpler alternative approach to an ultra-high purity large scale gas cell [62, 63]. It has been shown that cooling the stopping gas to cryogenic temperatures increases the ion survival and transport efficiency. In Ref. [62] the combined survival and transport efficiency for α-recoil ions was observed to saturate just below 90K. The high efficiency and saturation were attributed to freezing of the impurities which enhances the survival of thermalized ions. The effect has been observed also at low ionization densities induced by a proton beam [63]. In addition to being a relatively simple method for achieving pure conditions, the required size of the cell can be smaller as the density of the gas ρ_{gas} scales as $\frac{1}{T}$. The studies in Refs. [62,63] were done in a "closed cell", so no ions were extracted into high vacuum.

To study the next step a cryogenically cooled ion guide was developed to serve as a prototyping device for the full scale cryogenic ion catcher recently tested at GSI. The cryogenic ion guide (CIG) is based on the existing light ion guide design [55] that is mounted onto a vacuum-isolated cold finger. The cold finger is cooled by liquid nitrogen (LN_2) bath which serves also as a cooler for the stopping gas. The cryogenic ion guide setup at IGISOL is illustrated in Fig. 3.4.

The light ion guide is a versatile tool for testing several of the properties learned from the closed cell studies. It can house a small α-recoil source (^{223}Ra) for off-line studies thus providing a reference to earlier works. At the same time it can house a target for producing radioactive species from light-ion induced fusion evaporation reactions. Finally, it can be used to study the stopping of a stable energetic beam. However, as shown in Fig 3.5, the small size (inner diameter $\sim$ 30 mm) limits the useful stopping range to a fraction of a larger cell. On the other hand, the small size

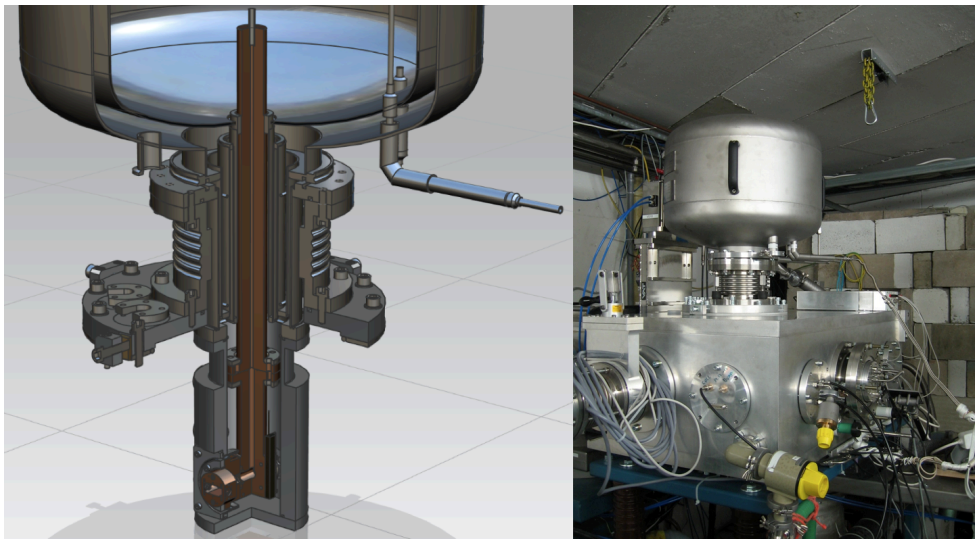

Figure 3.4: The cryogenic ion guide setup at IGISOL. Left: The technical structure of the system. The LN_2 bath cryostat used for cooling the cold finger and He gas is on top. The cold finger is surrounded by an insulation vacuum vessel. The light ion guide attached to the tip of the cold finger is outside the insulation vacuum. Right: The setup mounted into the IGISOL target chamber.

means small volume ($V \sim 3$ cm^3) which allows for a fast extraction of ions and the capability to study effects of cooling on the extraction times.

3.2. In-flight: Momentum Achromat Recoil Spectrometer

The momentum achromat recoil spectrometer (MARS), illustrated in Fig. 3.6, is an in-flight recoil spectrometer at the Cyclotron Institute of Texas A&M University. MARS is built for providing radioactive beams produced in transfer reactions using inverse kinematics for a wide variety of physics cases which are outlined along with the development and detailed design parameters in Refs. [65–67] and references therein.

Heavy ion beams from the superconducting K-500 cyclotron are used as a primary beam to produce the desired reaction products by bombarding a cryogenically cooled gas target separated from high vacuum by thin (4 - 50 μm) havar windows. The reaction products recoiling out from the gas target in the angular range between 0°

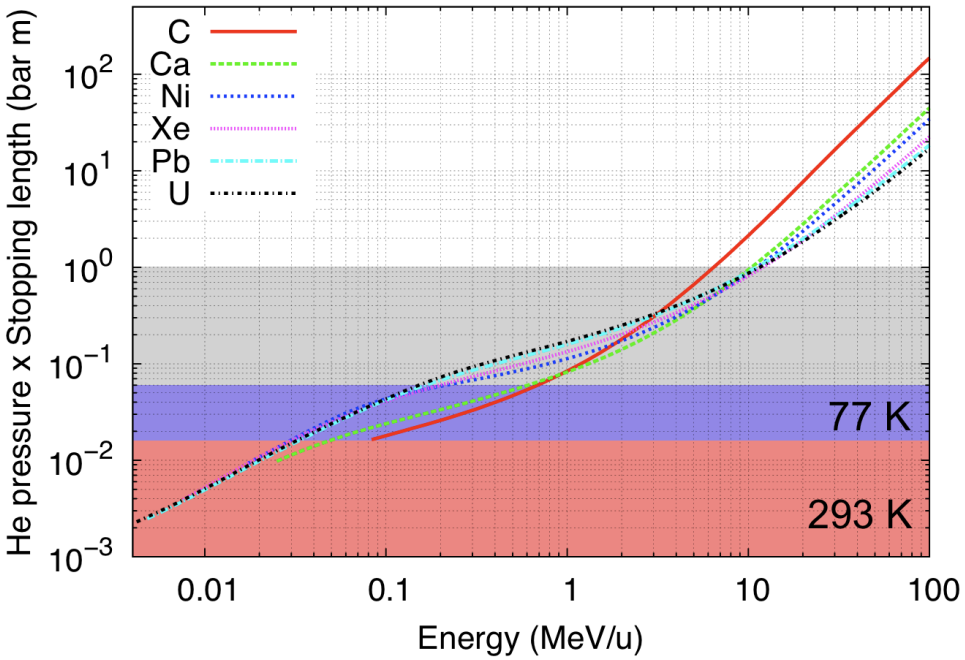

Figure 3.5: Stopping of ions in helium gas based on a SRIM [64] calculation. The red region is accessible with a standard light ion guide [55] in room temperature and the extended blue zone becomes accessible by cooling the stopping gas to liquid nitrogen (LN_2) temperature. The gray shade demonstrates the region accessible with one meter long gas cell with a one bar of helium at room temperature.

to 30° can be injected into the momentum achromat formed by a combination of three quadrupoles and two dipoles in a QQDQD configuration. After the momentum achromat the beam travels through a Wien filter where perpendicular electric and magnetic fields select products with velocity $v = E/B$, where E and B are the strengths of the electric and magnetic fields, respectively. After the Wien filter the third dipole with an adjustable bending angle is used to match the momentum and velocity dispersions and the last quadrupole doublet provides a m/q (mass to charge ratio) focus to the focal plane. The three first sets of slits are used to define the solid angle acceptance, horizontal momentum selection and vertical extent of the beam, whereas the last two are used for final solid angle and the m/q selection in the mass focal plane [67].

The MARS has a typical mass resolving power $MRP = 300$ and energy acceptance

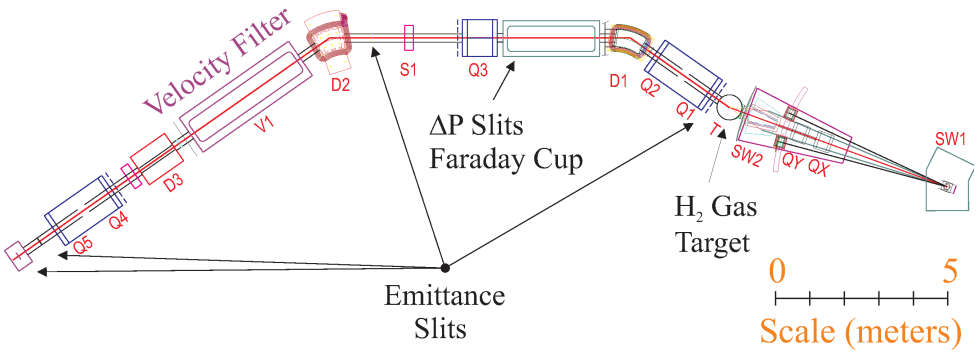

Figure 3.6: Layout of the Momentum Achromat Recoil Spectrometer (MARS) at the Cyclotron Institute of Texas A&M University. Quadrupole magnets are labeled with "Q", dipole magnets with "D".

$\frac{\Delta E}{E} = \pm 9\%$. The species in the final beam are identified with a ΔE-E telescope located at the focal plane. Examples of beam identification plots from the experiments in this work are given in Fig. 3.7. With the momentum defining slits, the momentum spread of the final beam can be narrowed down to the sub-% level, allowing a well-controlled implantation depth distribution in the stopping medium.

In the decay study of ^{23}Al, the ^{1}H(^{24}Mg,^{23}Al)2n reaction in inverse kinematics was used by bombarding a 2.5 mg/cm^2-thick liquid-nitrogen-cooled H_2 target at 1.6 atm pressure with a ^{24}Mg beam at 48 MeV/u. Separation of the reaction products with the MARS resulted in a beam of up to 4000 ^{23}Al ions/s at 42 MeV/u with a purity of better than 90% and a momentum spread $\Delta p/p = \pm 0.6\%$.

In the case of ^{31}Cl, the secondary beam was produced in the inverse kinematics fusion-evaporation reaction ^{1}H(^{32}S,^{31}Cl)2n by bombarding a 2.5 mg/cm^2-thick liquid-nitrogen-cooled H_2 target at 1.6 atm pressure with a ^{32}S beam at 40 MeV/u. The final separated beam had up to 2-3000 ^{31}Cl ions/s at 34 MeV/u with purity of a 89% and a momentum spread $\Delta p/p = \pm 0.6\%$. Beam identification plots from both of the experiments are given in Fig. 3.7.

The produced beam is selected by centering the species of interest in the target detector setup and then cutting away the other species using momentum defining and physical slits. The top panel of Fig. 3.7 shows the cut made in the production of ^{23}Al. The resulting beam is a cocktail of the wanted species with some impurities that may be present.

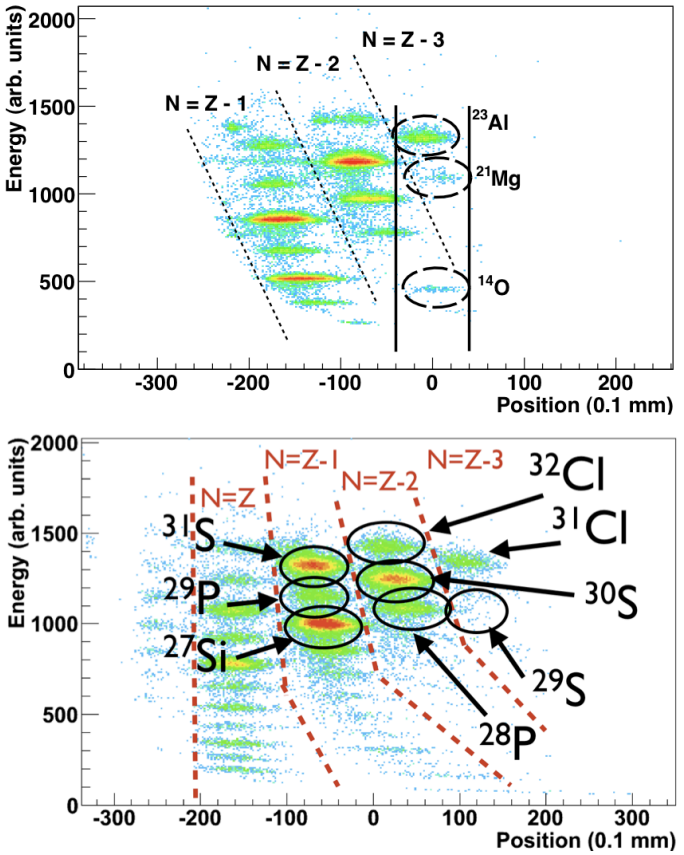

Figure 3.7: Secondary beam identification with the ΔE-E target telescope at the focal plane of MARS. The upper panel presents the identification plot from the ^{23}Al experiment. The vertical bars represent the position of the momentum-defining slits in MARS during the production of ^{23}Al. This setting yields $\Delta p/p = \pm 0.6\%$ and a purity of better than 90%. The lower panel shows the identification plot from the ^{31}Cl experiment with all the produced species included.

4. Experimental Techniques

4.1. Ion trap setup: JYFLTRAP

In general, ion traps are devices whereby electromagnetic fields are used to confine charged particles into a well-defined finite volume for (in principle) infinite times. The basics and progress of Penning trap mass spectrometry (PTMS) are reviewed in Ref. [68].

4.1.1. Working principle of a Penning trap

A Penning trap is formed by a combination of static electric ($\vec{E}$) and magnetic ($\vec{B}$) fields. Housed in the magnetic field, a set of electrodes create a potential, in which movement of the ions with charge q is defined by the Lorentz force: $\vec{F} = q(\vec{E}+\vec{v}\times\vec{B})$. The z-axis of the electric field is usually selected to be parallel to the magnetic field. In such a case, if the stability conditions are met, the ions end up having three eigenmotions that are illustrated in Fig. 4.1. In the axial direction (the z-direction) ions with charge q and mass m are oscillating as a harmonic oscillator with frequency ν_z and in the radial direction the oscillation has two components: the reduced cyclotron motion with frequency ν_+ and the magnetron motion with frequency ν_- In an ideal trap these frequencies are coupled to the actual cyclotron frequency of the ion by the relation:

$$\nu_+ + \nu_- = \nu_c = \frac{1}{2\pi}\frac{qB}{m}, \tag{4.1}$$

where B is the strength of the magnetic field. This relation establishes the usefulness of the Penning trap as a mass measurement tool: the sum of the two eigenmotions of the ion in the trap are directly related to the charge-to-mass ratio of the ion. In practice, the magnetic field and the trap dimensions are fixed, so the ion motions are manipulated by altering the electric fields. In the following, the mass measurement principle is discussed briefly, using the JYFLTRAP setup as an example.

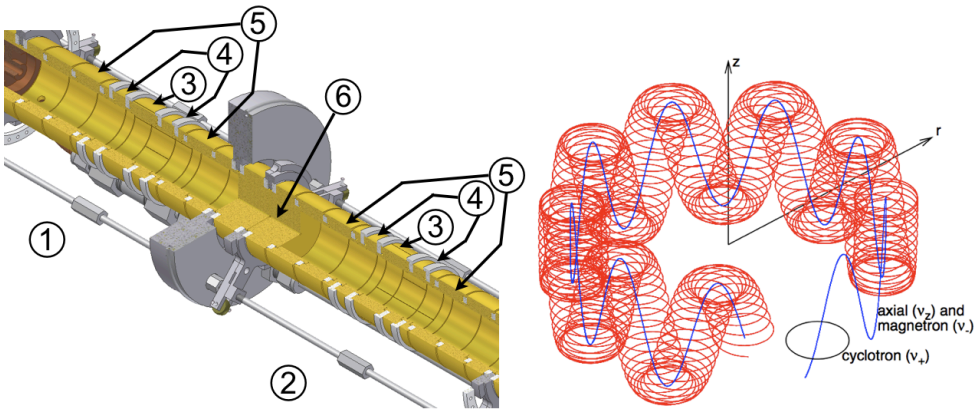

Figure 4.1: The electrode structure of JYFLTRAP is shown on the left panel: 1. Purification trap. 2. Precision trap. 3. Ring electrodes. 4. Correction electrodes. 5. End cap electrodes. 6. 2 mm diaphragm. The right panel illustrates the ion motion in a Penning trap (Original plot courtesy of T. Eronen).

4.1.2. The JYFLTRAP Setup

The JYFLTRAP setup is a versatile device for a range of mass measurements and mass-filtering applications that are well documented in Refs. [54, 69] and references therein. The DC (direct current) beam of ions with the same A/q from the IGISOL (Ch. 3) are fed into a gas-filled radio-frequency quadrupole (RFQ) cooler-buncher [53]. The RFQ is used to prepare well-defined ion samples (bunches) by decelerating them with a potential gradient, followed by trapping into a potential created by radio-frequency quadrupole and DC electric fields and finally cooling by collisions with the He buffer gas ($p \sim 1$ mbar). After a desired collection time, the ions are released and injected into the JYFLTRAP Penning trap setup consisting of two identical, cylindrical traps inside the same superconducting 7 T magnet [54, 69].

The first trap works as a purification trap with a MRP up to a few $\times 10^5$. This trap is filled with low-pressure helium gas ($p \sim 10^{-4}$ mbar) to cool the captured ions. The magnetron radius of all ions (independent of mass) is increased with an electric dipole excitation and is followed by an electric quadrupole excitation to center the ions mass-selectively [70]. At this point only the ions with matching excitation frequency are at an orbit with a small enough radius to pass the 2 mm diaphragm. The rest will collide with the entrance wall of the diaphragm when the sample is moved forward to the second trap.

The mass of the ions of interest is determined via the standard time-of-flight ion cyclotron resonance (TOF-ICR) method [71, 72]. The isobarically pure sample of ions is excited with a phase-locked dipole excitation to increase their magnetron radius [73], followed by a quadrupole excitation with the frequency $\nu_c = \frac{1}{2\pi}\frac{q}{m}B$. This excitation converts the initial magnetron motion of the ions into the reduced cyclotron motion, resulting in a maximum increase in the radial energy for resonantly excited ions. This increase is detected as a reduction in the time of flight when ions travel to a micro-channel plate detector. The flight times of ions are recorded while the excitation frequency is scanned, resulting in the typical resonance curve given in Fig. 4.2. It is worth noting, that the true cyclotron frequency, ν_c, is not a trap eigenfrequency and it can not be directly determined. Instead, the sideband frequency, $\nu_+ + \nu_-$, is measured and although systematic frequency shifts might arise due to misalignment and harmonic distortion, their contributions are lower than the uncertainties typically quoted for unstable ions [74, 75].

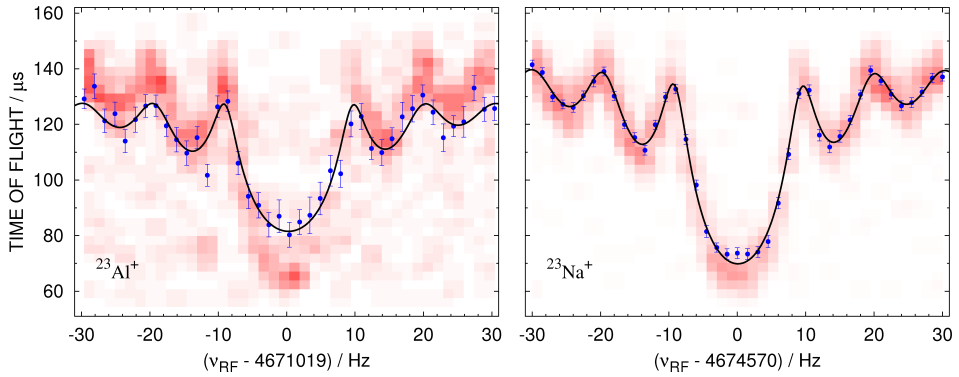

Figure 4.2: Typical cyclotron resonance curves of $^{23}Al^+$ (left) and $^{23}Na^+$ (right) from this experiment. The intensity of the red color indicates the amount of ions arriving in a given time bin, and the solid dots give the average of all time-of-flights at a given frequency.

The mass of the ions of interest is determined from the ratio of the measured cyclotron frequency of the sample and a well-known reference case, i.e.

$$m = \frac{\nu_{c,ref}}{\nu_c}(m_{ref} - m_e) + m_e. \tag{4.2}$$

The measurements of the ions of interest are interleaved by reference measurements to account for temporal changes in the magnetic field and the final frequency ratio

is taken as weighted average of all such pairs. In this work, the masses of ^{23}Al and ^{23}Mg were measured by using stable ^{23}Na as a reference. The analysis procedure reported in Ref. [76] is similar to the high-precision Q_{EC} measurements (see e.g. [77] and references therein). It is worth noting, that as all ions used in this study have the same $A/q = 23$, the precision is enhanced due to the absence of mass-dependent frequency shifts [78].

4.2. Decay Spectroscopy by the Implantation Technique

4.2.1. Implantation Setups

Radioactive decay studies following implantation of the source into the detection medium is a standard technique especially in the case of high energy secondary beams of reaction products from different types of recoil spectrometers [79–82]. During this work an implantation setup was developed for the MARS to be used in studies of β-decaying nuclei. Here a description of the first versions of the setup used for ^{23}Al and ^{31}Cl are given.

The implantation chamber, which was installed into the focal plane of MARS, housed a rotatable degrader system and our detector setup. A schematic presentation of the setup is given in Fig. 4.3. The radioactive species in the beam were first identified with reduced beam intensity in a ΔE-E target telescope placed in front of the detector set up. After the separator had been adjusted so that only the activity of interest passed through the last pair of slits, the telescope was moved away and the beam was allowed to enter the implantation chamber. The beam then traveled through an Al degrader, which was used to control the implantation depth into the detector stack. The angular resolution of the rotating degrader system is 0.1°.

Setup I – Decay spectroscopy of ^{23}Al and ^{31}Cl

The very first experimental setup used in experiments for the study of the β-decay of ^{23}Al [83] and ^{31}Cl [84] was a detector stack consisting of a double-sided silicon strip detector (DSSSD) and a thick silicon pad-detector. The DSSSD was a 69 μm thick Micron W1 with 16(x)+16(y) 3.1 $\times$ 50 mm^2 strips, and the Si pad was 998-μm thick, with a surface area of 50 $\times$ 50 mm^2. The detector stack had cooling capability and was mounted on a platform at a 45° angle in order to increase the effective implantation thickness and to allow for a good gamma-ray efficiency for

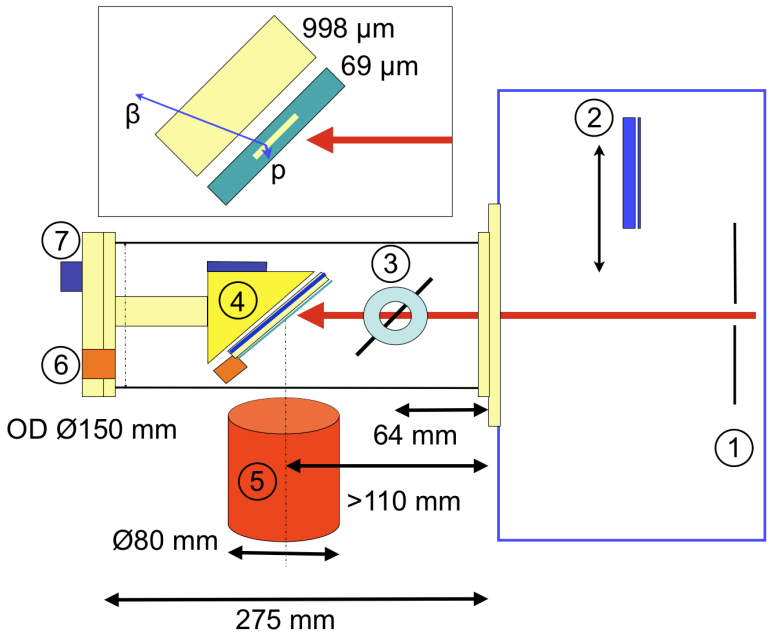

Figure 4.3: Schematic presentation of the detector setup I at the focal plane of MARS. The red arrow illustrates the beam. 1. Separator XY-slits, 2. ΔE-E detector for beam tuning, 3. Rotatable aluminum degrader, 4. 45° wedge with the detector stack, 5 HPGe detector, 6. Cabling connections, 7. Cooling system. Setups II and III had an additional HPGe detector on the opposite side of the chamber. The inset shows the detector stack from setup I (not in scale). See text for more details.

a 70%-relative-efficiency high-purity germanium (HPGe) detector installed outside the chamber as close as physically possible (11 cm).

Setup II – Decay spectroscopy of ^{31}Cl

The second setup was otherwise similar to the first one, but it had an extended detector stack, consisting of a single-sided silicon strip detector (SSD), a double-sided silicon strip detector (DSSSD) and a thick silicon pad-detector. The SSD used was 300 μm thick Micron X with 16 strips that were summed by a cabling connector where all signal leads were soldered together. The DSSSD we used was a 45 μm thick Micron BB2 with 24(x)+24(y) 1.1×25 mm^2 strips, and the Si-pad was 998-μm thick, with a surface area of 50×50 mm^2. Two 70%-relative-efficiency high-

purity germanium (HPGe) detectors were installed outside the chamber as close as physically possible (11 cm) in a back-to-back configuration.

Setup III – High intensity $\beta\gamma$-study of ^{31}Cl

The second setup was modified so that the first SSD and DSSSD were replaced by an aluminum plate (thickness 200 μm) to allow the use of maximal beam intensity to measure high statistics for $\beta\gamma\gamma$-coincidences. The Si-pad detector was used as a β-detector and the two HPGe detectors were used in same configuration as in setup II.

Setup IV – Determination of the Half-life of ^{31}Cl

The half-life determination was done by using a tape-transport system connected to the focal plane of MARS. The ^{31}Cl beam was separated and implanted into the aluminized mylar tape that was outside the vacuum. The half-life determination was done by moving the implanted sample to a 4π proportional gas counter system that has been developed for high-precision studies of super-allowed β-decays. See e.g. Ref. [85] and references therein for more details of the tape transport and detection system.

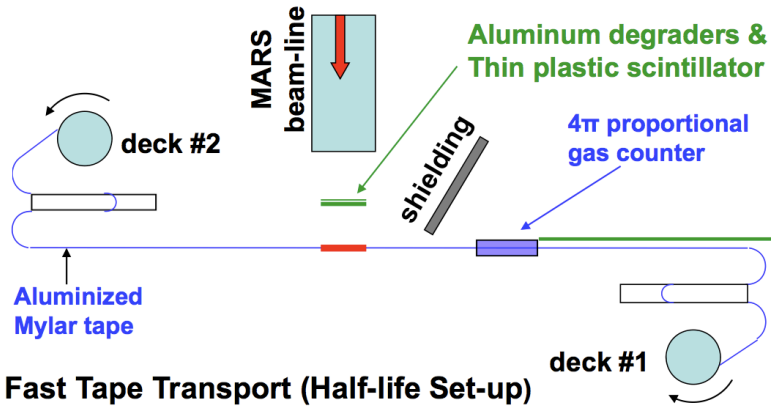

Figure 4.4: Schematic presentation of the setup used for determining the half-life of ^{31}Cl. Figure courtesy of Victor Iacob.

4.2.2. Measurement procedure

In the experiments, the two (three) Si detectors were used in two different modes: an "implantation control mode" and a "measurement mode". In the first mode the detector were used as a $\Delta E-E$ ($\Delta E-\Delta E-E$) telescope to control the implantation of the beam of interest midway into the DSSSD by adjusting the implantation depth with the rotating Al degrader and observing the beam spot in the two-dimensional energy-loss-versus-energy plot relating the signals from both detectors. Later this was done in the DSSSD alone when using only two detectors. In case of three detectors, the beam spot was also observed in the two-dimensional energy-loss-versus-energy-loss plot.

The beam tuning procedure is illustrated in Fig. 4.5. After the species of interest (^{31}Cl in this case) was selected from the separator it goes through the whole setup and a signal can be seen clearly in both the DSSSD and the Si-pad. When the angle of the degrader is increased, the spot in the ΔE-E plot moves until it disappears from the back detector and is fully stopped in the DSSSD. If the degrader angle is increased further, the signal disappears also from the DSSSD spectrum implying that it is fully stopped in the degrader. Because the energy loss and range are proportional to $1/\cos\,\theta$, where θ is the degrader angle, the degrader angle when the beam is stopped into the middle of the DSSSD is found as average of these two angles. The right panel of figure 4.5 illustrates the ΔE-ΔE plot from the second ^{31}Cl experiment. Here a clear punch through point in the topmost detector can be seen. The average straggling for the beams used was determined from LISE++ [86] calculations and GEANT4 [87] simulations and it was found to be around 10-20 μm, depending on the ion of interest.

In the ^{23}Al experiment, these measurements led to the decision to reduce the momentum spread of the beam from $\Delta p/p = \pm 0.6\%$ to $\pm 0.25\%$ by closing the momentum-defining slits after dipole 1 of MARS. This reduced the rate of ^{23}Al nuclei striking the detector at 42 MeV/u to 600-800 pps and narrowed the depth distribution of the implanted ^{23}Al to $\sim$ 17 μm, full width at half maximum (FWHM). In the ^{31}Cl experiments the momentum spread of the beam was $\pm 0.25\%$, adjusted based on similar arguments as above. This resulted in a rate of ^{31}Cl nuclei (E = 34 MeV/u) of a few hundred pps and with depth distribution of the stopped ^{31}Cl of $\sim$ 13 μm, FWHM.

During the experiments the beams were pulsed: in the case of ^{23}Al, the desired activity was implanted into the detector for one second, followed by a 5 ms wait. Decays from the sample were then recorded for one second, yielding a duty-cycle

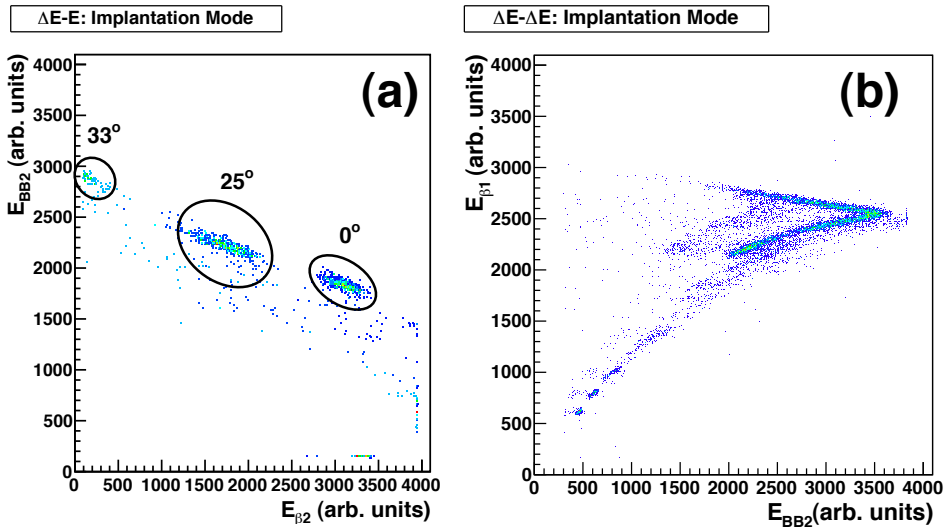

Figure 4.5: An example of the beam tuning in case of the ^{31}Cl beam in implantation mode. (a) With the ΔE-E telescope (labeled as BB2 and β_2). The aluminum degrader angles of 0°, 25° and 33° are shown overlaid in the same plot. (b) With the ΔE-ΔE telescope (labeled as β_1 and BB2) when the aluminum degrader angle was at 47°.

of 50%. In the case of ^{31}Cl the implantation and measurement time were 300 ms with a 5 ms wait in between. The secondary beam intensity was limited to a few hundred ions per second and the implantation spot was spread over several strips to reduce damage to the detectors. This also helped to keep the acquisition count-rate at around a few hundred Hz, which resulted in a negligible dead-time. In the high intensity study of ^{31}Cl (setup III), the thin detectors were replaced by a dummy Al plate to utilize full available beam intensity. All the data were collected with a condition of a logical OR between β-p coincidences and β-$\gamma(\gamma)$ coincidences.

4.2.3. Detector responses

When a β-decay with proton emission happens in the middle of the detector, the observed total decay energy is a sum of the proton, the recoiling daughter nucleus and the average energy that the preceding β deposits in the detector, i.e.

$$E_{\text{obs.}} = E_{\text{p}} + E_{\text{rec.}} + E_{\langle\beta\rangle}. \tag{4.3}$$

After the proton emission, the recoiling daughter nucleus has an energy that is $1/M_{\text{rec.}} \cdot E_{\text{p}}$, assuming that the decay takes place at rest and that the recoil from β-decay is negligible. However, some of the energy of the daughter nucleus is not recorded by the detector, as the heavy ion loses a fraction of it's energy to the silicon lattice instead of to the ionization. This fraction k can be obtained e.g. from a TRIM [64] calculation for the relevant recoil energies. Calculated fractions for selected recoils are illustrated in Fig. 4.6. Thus, equation 4.3 becomes:

$$\begin{aligned} E_{\text{obs.}} &= E_{\text{p}} + \frac{k}{M_{\text{rec.}}} E_{\text{p}} + E_{\langle\beta\rangle} \\ &= E_{\text{p}} \left(1 + \frac{k}{M_{\text{rec.}}}\right) + E_{\langle\beta\rangle}. \end{aligned} \tag{4.4}$$

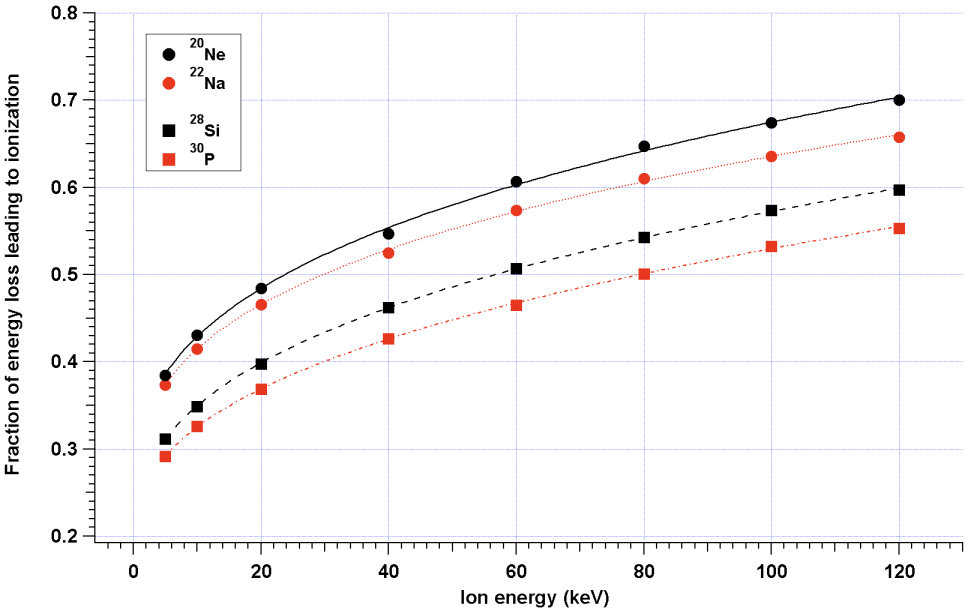

Figure 4.6: Fraction of the energy loss of the recoils leading to the ionization process. The data points are simulated with TRIM [64] ($N = 10000$) and the respective lines show the fits that were used to determine the fraction for implanted recoil energies.

The β-response of a silicon detector depends on the volume of the active detection area from which the signal is collected. In the case of the Si-pad detector the total

volume of the detector is about 2500 mm^3, whereas the volume of a single pixel in the DSSSD is only about 0.59 mm^3 and 0.045 mm^3 for W1 and BB2, respectively. The betas are emitted isotropically and therefore the majority of them deposit only very little energy as they exit through about the half-thickness of the implantation detector. This deposited energy shifts the peaks a little in energy and the betas that leave more along the detector cause the proton lines to tail on the high energy side of the peak.

These effects are demonstrated in Fig. 4.7 (a,b) for a thick Si-pad detector. Here we can see the effects of the β-summing to the peaks of ^{20}Na. Notably both major α-lines are showing an effect of forming two peaks close to each other, most likely due to the fact that in this case the implantation is not in the middle of the detector but closer to the edge. Naturally the betas leaving through the thicker part of the detector deposit more energy and cause the second peak to appear. Figure 4.7 also shows the spectra from a single strip in the W1 (c) and BB2 (d) respectively. The volume effect is demonstrated clearly in the low energy part in which the beta background is shifting lower as the active detection volume gets smaller.

As the decay occurs inside the detection medium, the preceding β-particles are always present and summed up with the measured protons, resulting in proton peaks that do not follow a pure Gaussian shape. Instead the peaks have a tail on the high-energy side, which can be described with a skewed Gaussian peak shape of an approximate form:

$$\begin{aligned} f(E) &= \frac{1}{\sqrt{2\pi}\sigma} exp\left[-\frac{1}{2}\left(\frac{E-\mu}{\sigma}\right)^2\right], \text{for } E \leq \mu + a\cdot\sigma \\ f(E) &\propto |E-\mu|^{-n}, \text{for } E > \mu + a\cdot\sigma, \end{aligned} \tag{4.5}$$

where E is the energy, σ is the peak width, μ is the peak centroid and a and n are constants. This peak shape is available in the ROOT [88] default package RooFit (where it is called a Crystal Ball shape). In practice, major proton lines are used to determine the parameters defining the shape of the peak and then these parameters are fixed as the shape of the peak (β-tailing) is independent of energy.

The thickness of the detector determines the proton detection efficiency: protons with higher energy will lose only a fraction of their energy in a thin detector. In practice, the half-thicknesses of the used DSSSDs are enough to fully stop protons up to 1.2 to 1.7 MeV. Some of the higher energy protons will lose only a fraction of their energy in the active volume of the implantation detector before escaping,

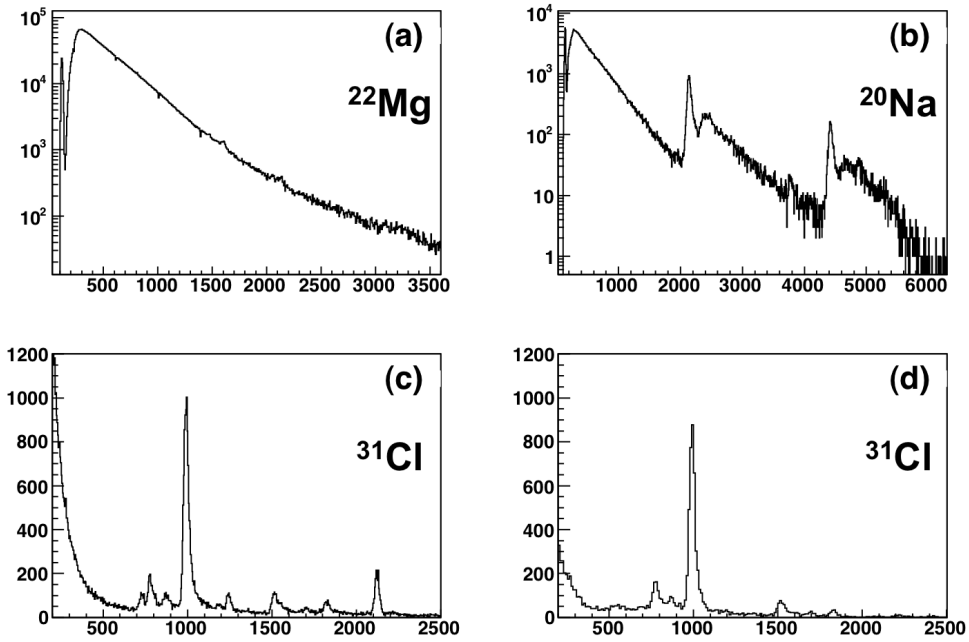

Figure 4.7: β-responses of different Si detectors. Panel (a) show the β-decay of ^{22}Mg and panel (b) ^{20}Na recorded with a 998μm Si-pad. The double peaks in the ^{20}Na decay are due to fact that the decay doesn't happen in the middle of the detector, thus adding more into the total energy of the decay when the β escapes through thicker part. (c) One 3×50 mm^2 strip from W1(69 μm) type DSSSD. (d) One 1×25 mm^2 strip from BB2(45 μm) type DSSSD, for the decay of ^{31}Cl in the middle of the detector. The spectrum in (c) has also protons originating from the decay of ^{29}S which also is stopped inside the DSSSD, whereas in (d) ^{29}S is not detected inside the DSSSD.

whereas some of the protons will still be detected at full energy (e.g. those emitted along the strip). As the energy gets higher the full energy peak gets smaller and the continuum of energy deposited due to the escaping protons gets higher. A Geant4 [87] simulation of the energy deposition of protons with several energies and different detection volumes was used to determine the detection efficiency of the DSSSD. A comparison of the simulated full-peak detection efficiencies of BB2 and W1-type DSSSDs are given in Fig. 4.8. The simulations verify the understanding that below one MeV the efficiency is constant and starts to decrease with increasing proton energy. In addition to losing protons from the full-energy peak, the escaping protons contribute to the overall background. The total line shape was resolved

from aforementioned simulations and the details are presented in appendix section A.3.

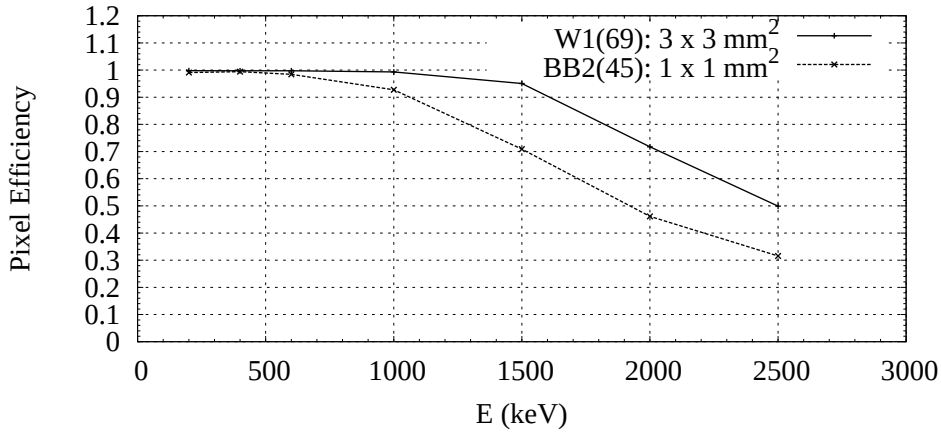

Figure 4.8: Simulated pixel efficiencies of W1 and BB2 type DSSSDs. In the simulation, total of 10^6 protons with energies of 0.2, 0.4, 0.6, 1.0, 1.5, 2.0 and 2.5 MeV were emitted from a source in the middle of a 3.1×3.1 mm^2 pixel in a 69 μm thick W1-type DSSSD or in a 1×1 mm^2 pixel in 45 μm^2 thick BB2-type DSSSD. The uncertainties of each point are of the order of 2%. Simulation data courtesy of B. Roeder.

5. Results and Discussion

5.1. Cryogenic Ion Guide tests

The cryogenic ion guide was tested in two different experiments. The first experiment was used to study the general behavior of the system whereas the second was dedicated for a study of the stopping properties. The discussion on the stopping and topics related to the cryogenic gas catcher development are detailed in Refs. [89,90] whereas this section concentrates on the properties that have implications for the IGISOL method. The stopping tests were conducted by using 300 and 340 MeV ^{58}Ni beams from the K-130 cyclotron. Radioactive ion beams were produced by bombarding a 4.4 mg/cm^2 ^{nat}Mg target with 40 MeV protons. To test the extraction of radioactive ions without beams from the cyclotron, a ^{223}Ra α-recoil source was housed inside the ion guide.

The system was found to cool to a minimum of about 80 K in vacuum (coolant T = 77K) and with gas load the operating point was close to 90 K. This can be understood as the ion guide is exposed to the surrounding vacuum. In addition, the pumping arrangements of the cold finger insulating vacuum were insufficient (due to restrictions placed by the operating environment, the insulating vacuum had to be handled with same pumping system as the target chamber, leading to heat leaks with increasing gas load).

Increasing the helium pressure in the ion guide increases the mass flow through the exit nozzle. The increase in mass flow is observable throughout the differential pumping system as shown in Fig. 5.1. The direct conclusion is that less pumping capacity is needed for a constant stopping density in the case of lower temperature, or, more important, higher stopping density can be achieved with the existing pumping setup. As the density scales with T^{-1} and the conductance of the exit hole with $T^{1/2}$, the mass flow exiting the ion guide and thus the pressure of the vacuum system should scale with $T^{-1/2}$. Because the pressure inside the ion guide cannot be determined at very low pressures (sub mbar), it is fair to reject the points at "zero" pressure in Fig. 5.1. This yields the illustrated curves that follow a power law with a power close to one (0.9 – 1.1). Taking into account that the vacuum system gauges

are calibrated for air (mostly N_2) and not for He, the trend can be said to be linear within the uncertainties. The ratio of the pressure curves scales roughly as 0.5.

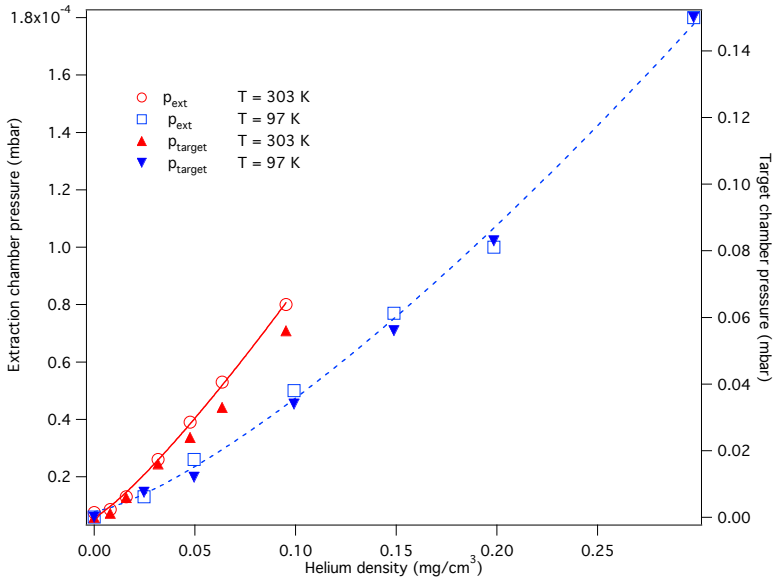

Figure 5.1: Effect of stopping gas density on the pressure of the pumping system. The same pressures ranging from 0 to 600 mbar were used for both temperatures. For constant density, less pumping power is needed when ion guide and stopping gas are cooled. The fits shown in the graph approach linearity if the points at "zero" pressure are rejected, yielding roughly the expected $T^{-1/2}$ dependence between the vacuum system pressure and density.

Mass scans in the IGISOL focal plane at room temperature and after cooling down are shown in Fig. 5.2. The effect of freezing out impurities is clearly demonstrated as several mass peaks vanish. However, as the lowest temperature reachable with this setup is only 80 to 90 K, it is clear that oxygen and nitrogen are not frozen from the gas. In fact, the mass peaks at $A/q = 14, 16, 28, 32$ (N^+, O^+,N_2^+, O_2^+) are enhanced visibly. In addition at least neon (melting point 24 K, boiling point 27 K) and argon (m.p. 84 K, b.p. 87 K) currents are increased when cooling, but for example xenon (m.p. 161 K, b.p. 165 K) is diminishing. From this one can conclude that for further suppression of the impurities, lower temperatures, below the melting point of oxygen (~54 K), should be reached. The most practical way to achieve this would be use of cryo-cooler instead of a cryogenic liquid bath. A cryo-cooler is the solution that has been taken into use for the full-size cryogenic gas catcher project

for FAIR.

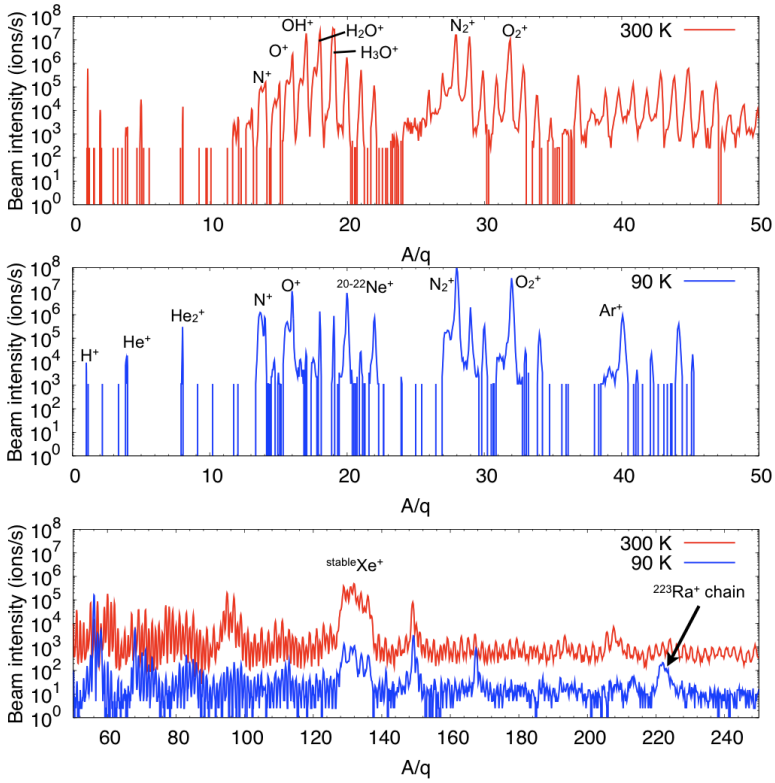

Figure 5.2: Mass scan in IGISOL focal plane at different temperatures. The two top panels show the lower end of the scanned mass range and the lower panel the higher part. Major identified constituents are labeled, see text for discussion.

As additional information, the mass scan in Fig. 5.2 shows that even the use of high purity He gas (typical in-house recycled He used at IGISOL corresponds to commercial purity 99.996%) and the gas purification traps [55] do not seem to remove all impurities. This effect has been observed e.g. in mass measurement experiments in the $A = 30$ region.

Extraction of a radioactive ion beam in cryogenic temperatures (and at room temperature as a reference) was tested with the ^{24}Mg(p,αn)^{20}Na reaction. This reaction is known have a good yield from IGISOL. ^{20}Na also has a short half-life of 446 ms, making it ideal for the secondary beam tuning (fast response to change of param-

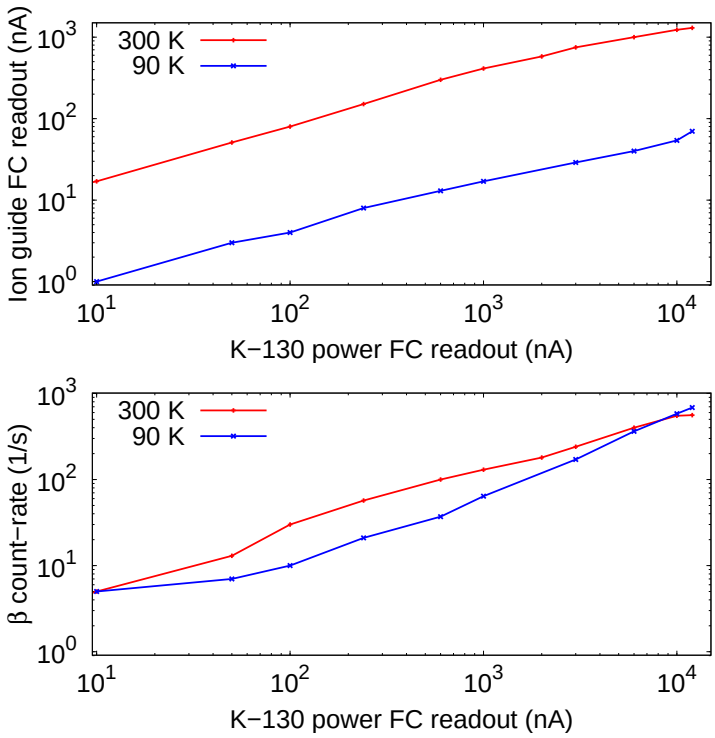

Figure 5.3: Extracted total secondary beam currents (upper panel) and produced activities at $A/q = 20$ (lower panel) from the cryogenic ion guide at different temperatures, as measured in the IGISOL focal plane. Cooling of the stopping gas and the ion guide clearly reduces the overall extracted current while keeping the extracted activity at approximately the same level.

eters). Figure 5.1 (lower panel) shows the measured ^{20}Na activity vs the primary proton beam current at room temperature and at cryogenic temperature. The upper panel of Fig. 5.1 shows the total output current from the ion guide for same primary beam intensities. The drop in total current due to freezing out of impurities is clearly visible. On the other hand, the activity produced does not change when cooling down (the small deviations can be accounted most likely for the fluctuations in the separator magnetic field etc.). Thus one can conclude, that cooling down the ion guide and stopping gas may provide a good way to suppress the impurities from the secondary beams without affecting the radioactive yield.

5.2. Mass excess of ^{23}Al

As described in Ref. [76], the masses of ^{23}Al and ^{23}Mg were measured with JYFL-TRAP by using stable ^{23}Na as a reference (see Fig. 4.2 in chapter 4 for illustration of typical resonances). All ions used in this study had the same $A/q = 23$, and thus the precision is enhanced due to the absence of mass-dependent frequency shifts. To avoid systematic frequency shifts due to high numbers of simultaneously stored ions in the trap, the number of stored ^{23}Mg and ^{23}Na ions were limited to a maximum of 2–3 ions per bunch. The excitation time of the ions was limited to 100 ms due to a rather strong damping from ion-atom collisions in the precision trap. The measured frequency ratios of $^{23}Mg^{+}/^{23}Na^{+}$ and $^{23}Al^{+}/^{23}Na^{+}$ with deduced mass excesses are presented in table 5.1. In total, 3 resonances were recorded for ^{23}Mg and 29 for ^{23}Al, interleaved by reference measurements to account for temporal changes in the magnetic field.

Table 5.1: The measured frequency ratios of given nuclei to reference nucleus ^{23}Na and deduced mass excesses as reported in Ref. [76].

Nuclide	$T_{1/2}$	Frequency ratio $\frac{\nu_{c,\mathrm{ref}}}{\nu_c}$	$ME_{\mathrm{Exp.}}$ (keV)	ME_{Lit} (keV)
^{23}Mg	11.317(11) s [91]	1.000189428(36)	-5473.38(77)	-5473.8(13) [3]
^{23}Al	446(6) ms [92]	1.000760142(16)	6748.07(34)	6770(19) [3]

5.2.1. Test of the Isobaric Multiplet Mass Equation

As the new value for the mass excess of ^{23}Al, 6748.07(34) keV, not only deviates from the previous values but is about two orders of magnitude more precise, it was used to test the validity of the IMME by combining it with the existing data. Given in table 5.2 are the members of the $A = 23, T = 3/2$ multiplet.

Table 5.2: The members of the $A = 23$, $T = 3/2$ quartet.

Nuclide	$T_{1/2,\text{g.s.}}$	T_3	$ME_{\text{g.s.}}$ (keV)	E_{ex} (keV)	$ME_{\text{T=3/2}}$ (keV)
^{23}Ne	37.24(12) s [91]	+3/2	-5154.05(10)[1]	-	-5154.05(10)
^{23}Na	stable	+1/2	-9529.8536(27)[1]	7891.19(15)[4]	-1638.66(15)
^{23}Mg	11.317(11) s [91]	-1/2	-5473.49(67)[2]	7802.64(48)[5]	2329.15(82)
^{23}Al	446(6) ms [92]	-3/2	6748.07(34)[3]	-	6748.07(34)

[1] From Ref. [3]. [2] Weighted average of Ref. [3] and this work (Table 5.1).
[3] This work. [4] From Ref. [91]. [5] Weighted average of Ref. [91] and Ref. [93].

The fit to the IMME, using values from table 5.2 and illustrated in Fig. 5.4, was done by using a standard non-linear least-squares fitting routine where the uncertainties in the energies of the isobaric analogue states were used as the weights. The results for both quadratic and cubic fits are tabulated in table 5.3 and compared to the values from the previous compilation [94]. The obtained fit to the quadratic form is remarkably good ($\chi^2/n = 0.28$) and all the parameters are determined with uncertainties less than 200 eV. A fit to the cubic form can be used to test how well the quadratic form reproduces the experimental data. As there are as many parameters as data points, the fit trivially reproduces the experimental data. To estimate the 1σ error bars for the cubic fit, each parameter was locked to the value from the best fit and then varied one by one so that one gets $\chi^2 = 1$ for the fit in each case. The values extracted from the cubic fit are also in table 5.3. All the lower-order terms (a,b,c) can be seen to be close to those from a quadratic fit and the cubic term 0.22(42) keV to be zero within the uncertainty. Therefore it is safe to say that IMME seems to hold very well for the $J^\pi = 5/2^+$, $T = 3/2$ quartet in $A = 23$.

Table 5.3: IMME coefficients from a fit to the data in table 5.2 and comparison to existing data. All fit parameters are given in keV.

	Quadratic			Cubic	
	This work	Ref. [94]		This work	Ref. [94]
a	288.54(18)	288.3(20)	a	288.77(47)	283.7(43)
b	-3967.40(12)	-3965.8(54)	b	-3967.90(94)	-3959(8)
c	225.99(10)	225.2(27)	c	225.88(23)	232(7)
χ^2/n	0.28	1.48	d	0.22(42)	-6.6(55)

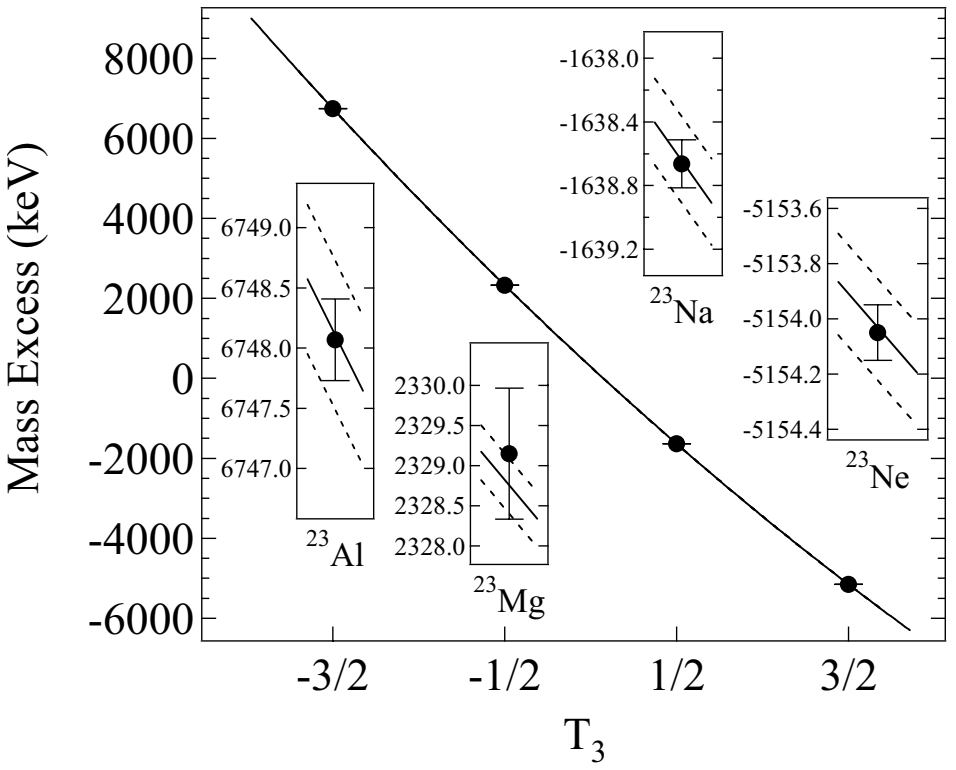

Figure 5.4: The $A = 23$, $T = 3/2$ multiplet and the fit to the quadratic IMME with 1σ error bands.

The latest compilation of the IMME coefficients and correlations includes 430 identified multiplets, given in Ref. [94]. The most notable deviations from Eq. 2.3, being statistically significant, are found in the $A = 8$, $T = 2$ quintet and the $A = 9$, $T = 3/2$ quartet. They are considered to be the only real deviations from the first-order perturbation treatment. Since this compilation, the validity of IMME has been of particular interest among sd-shell nuclei [95–103].

A possible breakdown of Eq. 2.3 in the $A = 33$, $T = 3/2$ quartet was suggested after the mass measurement of the ground state of ^{33}Ar [95]. However, this was solved by a better measurement of the excitation energy of the IAS in ^{33}Cl [96]. Recent determination of the masses of ^{35,36}K, belonging to the $A = 35$ and $A = 36$ multiplets [99], indicates a possible breakdown of the IMME in the $A = 35$ quartet. However, the deviations in the $A = 35$ case might be due to problems with the IAS in ^{35}Cl as discussed in Ref. [99]. Another addition towards testing the IMME in the upper sd-shell is provided by the $A = 37$ quartet [100], following the mass measurement of the ground state of ^{37}Ca. However, the experimental data of the analogue state in ^{37}Ar is not sufficiently precise for a meaningful test of the quadratic IMME.

To date, the most notable breakdown of IMME seems to be in the $A = 32$, $T = 2$ quintet. Ref. [98] reported a small violation of the IMME, determined with high precision via a measurement of the IAS in ^{32}S. It was also speculated that the ^{32}Si mass excess could be wrong and this has been confirmed by a Penning trap mass measurement [101]. Interestingly, it was found to deviate in such a way that does not restore the validity of the IMME and direct measurements of the mass excesses of ^{32}P and ^{32}Cl were called for. Ref. [102] reported a new Penning trap mass measurement of ^{31}S which was used to determine the mass excess of ^{32}Cl (indirectly through $S_p(^{32}\mathrm{Cl})$ and it was found to agree with the latest evaluation [3] and (^{3}He,t) data [104]. Based on extensive discussion, Ref. [102] calls for a new direct mass measurements of ^{32}Si, ^{32}P,^{32}Cl and ^{32}Ar to verify the breakdown. In Ref. [105] the isospin-breaking correction, δ_C, was determined experimentally to be 5.3(9)% in good agreement with results from a shell-model calculation 4.6(5)%. A recent theoretical work in Ref. [103] has a discussion on utilizing the latest versions of the universal *sd* interactions [106] on the latest experimental data in the $A = 32, T = 2$ quintet. Despite overall agreement with experimental data, there are indications of large uncertainties in some calculated values (e.g. the resulting Γ_p for the $T_3 = -1$ member varies significantly with the interaction used). Thus Ref. [103] calls for more accurate theoretical tools and more complete experimental level schemes, also in other multiplets to study e.g. the similarities between the isospin-mixing effects.

5.2.2. Influence on the reaction rate of ^{22}Mg(p,γ)^{23}Al

The improved ground state mass of ^{23}Al, 6748.07(34) keV from this work, also improves the ^{23}Al proton separation energy. The new $S_p(^{23}\mathrm{Al})$ = 141.11(43) keV can be calculated by combining our result for the mass excess of ^{23}Al and the mass excesses of ^{22}Mg, -399.79(25) keV [107] and ^{1}H, 7288.97050(11) keV [3]. The resulting $S_p(^{23}\mathrm{Al})$ is higher than previous (123(19) keV [108]), indicating a reduced halo nature. The new S_p has influence on the calculated astrophysical S-factor for the proton capture reaction ^{22}Mg(p,γ)^{23}Al and its corresponding reaction rate in the stellar environments [109, 110].

The reaction rate of ^{22}Mg(p,γ)^{23}Al is dominated by the direct capture component and the resonant capture is competitive only around 0.2-0.45 GK [109]. The new S_p changes the location of the lowest resonance (corresponding to the $J^\pi = 1/2^+$ first excited state in ^{23}Al) from E_r = 405(27) keV [108] to E_r = 387(19) keV. It is good to note that the uncertainty in the resonance energy is still dominated by the relatively large uncertainty of the energy of the first excited state in ^{23}Al. The effect of this change in the equilibrium density of ^{23}Al at 0.3 GK is about a factor of 2, making only a marginal contribution to the ^{22}Mg(p,γ)^{23}Al rate [110]. However, in the case of more violent scenarios with higher temperatures and densities, such as X-ray bursts, the new S_p value may help in fast sequential two-proton capture on ^{22}Mg. An increased S_p indicates ^{23}Al to be more resilient to destruction through photodissociation, making this isotope a potentially more important player in the reaction networks in explosive H-burning processes.

5.3. β-decay of ^{23}Al

β-decay of ^{23}Al was studied with setup I described in section 4.2.1. A brief overview of results is given here, based on the full discussion in Ref. [83].

5.3.1. γ spectrum

The β-gated γ-ray spectrum from the decay of ^{23}Al in this experiment is presented in Fig. 5.5. The intensities for the γ-ray lines at 1600 keV and 2050 keV, relative to the line at 451 keV, agree with the previous studies [48, 92, 93]. The only impurity present in larger quantities in the stopped beam, ^{14}O, is identified in the γ-ray spectrum through the 2313-keV line, which follows its β decay. There is also a tiny

amount of ^{22}Mg stopped in the thick Si-detector, because a few tens of 583 keV γ-rays from ^{22}Na are observed without any proton coincidences. The γ-rays that follow the β-decay of ^{23}Mg, most notably the one at 439 keV, are also present since this daughter activity stays in the detector. We do not observe the 2317-keV, 5055-keV, 5067-keV and 5729-keV γ-ray transitions observed in Ref. [111]. This is not surprising since these γ-ray transitions originate from the states at 7769.2(10) keV and 7779.9(9) keV, whose spin assignments are $9/2^+$ and $11/2^+$ respectively: Their population in β-decay would be negligible.

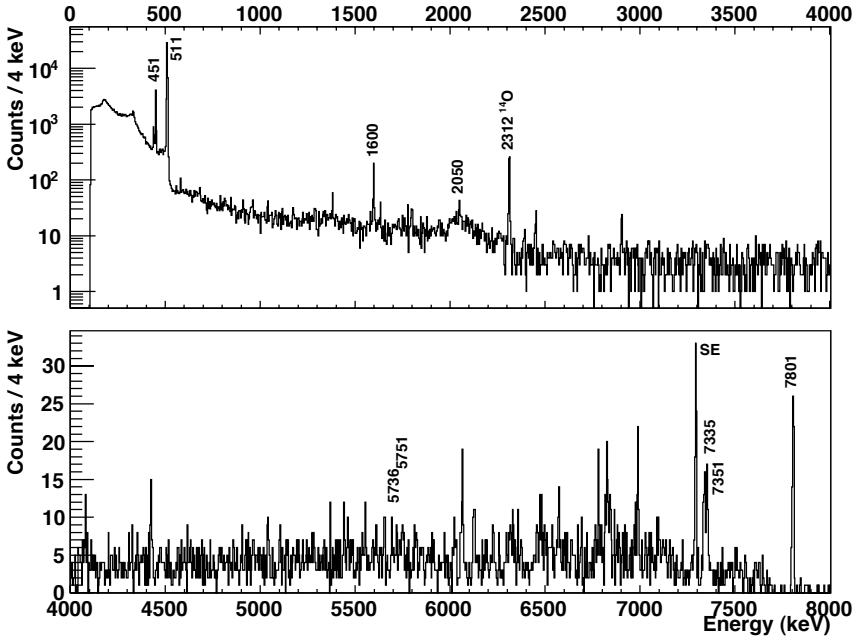

Figure 5.5: The γ-ray spectrum following the β decay of ^{23}Al from 0-4 MeV (upper panel, log scale) and 4-8 MeV (lower panel, linear scale). Major γ-lines relevant for the states near S_p are identified: The strongest transitions at 451 keV, 1600 keV and 2050 keV, as well as the 5751-keV, 7351-keV and 7801-keV transitions originating from the IAS, and the 5736-keV and 7335-keV transitions from the 7787 keV state just below the IAS are identified. The only major contaminant present was ^{14}O ($E_\gamma = 2313$ keV), as seen also in Fig. 3.7.

5.3.2. Proton spectrum

The energy calibration for the DSSSD was done with known β-delayed protons from the decay of ^{21}Mg [112]. In addition, the 554(6)-keV and 839(7)-keV proton lines from the decay of ^{23}Al [48] were also used as an internal calibration to obtain a more reliable extrapolation down to the interesting energy region around 200 keV. The ^{21}Mg beam, which is only a weak byproduct of our reaction (see Fig. 3.7), has a range in Al about 100 μm longer than ^{23}Al. By adjusting the energy degrader, we could tune it into the middle of the DSSSD, albeit with a meager rate of $\sim$1 pps.

We could clean the proton spectrum considerably by requiring that the multiplicity of each recorded event in the DSSSD is one, and that the energies of the front and back sides of the DSSSD are consistent with each other (i.e. $E_x = E_y$). This means that instead of looking at only 16 separate strips, we look into 256 separate pixels, each of size $\sim 3.1 \times 3.1$ mm^2. Still, the pixel volume of the DSSSD used was fairly large and, as can be seen in the top panel of Fig. A.1, its β-response yields a considerable background extending all the way up to about 400 keV in the ^{23}Al proton spectrum. To look for the astrophysically interesting proton energies we had to use background subtraction, see appendix A and Ref. [83] for more details. The resulting background-reduced spectrum for the β-decay of ^{23}Al is presented in Fig. 5.6 and compared with the one from Ref. [48]. The data from the present work is clearly closer to the spectrum presented in Ref. [48] than to the spectrum in Ref. [47], in which significant noise at low energy was evidently interpreted as a peak at $E_{p,lab} = 223$ keV.

The results obtained from our fits are presented in Table 5.4, where we give the observed peak centroids, deduced center-of-mass proton energies, energies of the intermediate excited states in ^{23}Mg, proton intensities relative to the 451-keV γ-transition, and absolute intensities from each state. It was shown in Ref. [92] that a doublet of states at 7787 and 7803 keV exists (see Fig. 5.7), of which the second was demonstrated to be the IAS of the $T = 3/2$ ^{23}Al ground state. The energy we obtain for the lowest measured proton group indicates that these protons originate from a level with an energy of 7787(11) keV instead of the IAS ($E_{ex} = 7802.64(48)$ keV [91, 93]), the state to which it was assigned in the previous works [47, 48]. This identification is based on the energy matching, on the fact of the existence of these two states 16 keV apart and the strong population of the lower state in β-decay [92, 93]. A comparison of our proton energies to those given in [47, 48] appears in Table 5.5. Both earlier works assigned the protons as being from the IAS, and used arguments based mostly on shell-model calculations with isospin-nonconserving

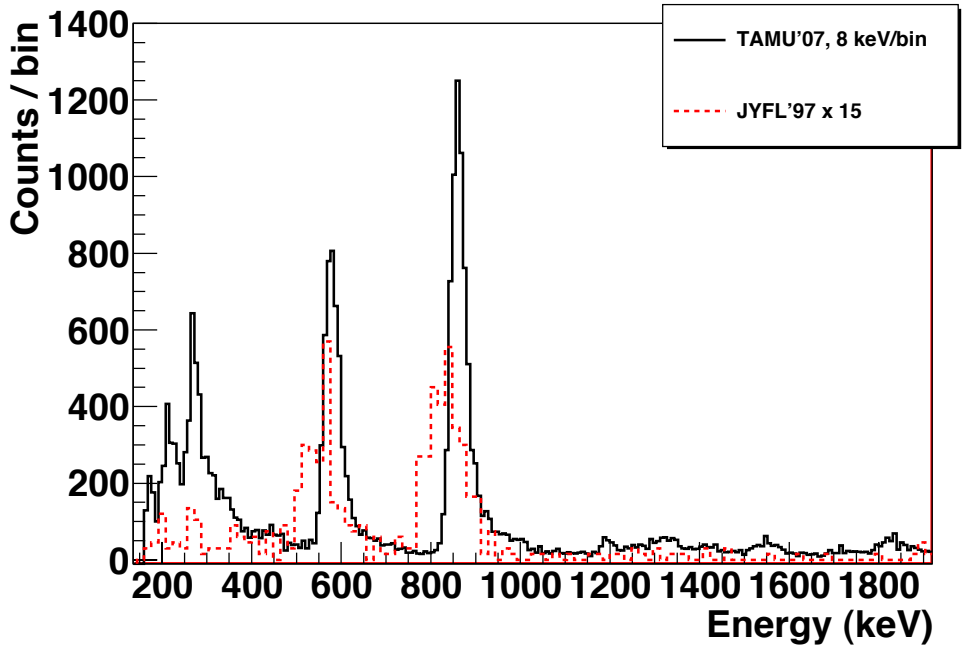

Figure 5.6: Comparison of the β-delayed proton spectrum of ^{23}Al obtained in this experiment (black solid line) and the spectrum published in [48], which has been magnified $\times 15$ (red dash line). The original data for this plot is courtesy of K. Peräjärvi [113]. The peaks from this work are slightly higher in energy because they represent the total measured decay energy, whereas in [48] the spectrum was obtained from a detector outside the source, which recorded only the proton energy.

interactions to achieve large enough isospin mixing to allow isospin-forbidden proton emission in competition with γ-ray emission. With our improved resolution and statistics, we do not see any substantial number of protons originating from the IAS and therefore we cannot support the extraordinarily large isospin mixing claimed in Ref. [47]. While with our typical resolution of 30 keV (FWHM) in the DSSSD used we cannot completely rule out some small contribution from the IAS, we do not find a reasonable argument to believe that of the two states in the doublet in question, the lower state ($T = 1/2$ isospin) does not proton-decay, while the (mostly) $T = 3/2$ IAS would, given that the decay of the latter is isospin forbidden. This is an additional argument for our identification.

We observe all previously identified β-delayed proton groups with emitted proton

Table 5.4: Measured proton energies and intensities from the β-decay of ^{23}Al. $E_{ex}(^{23}Mg)$ from the present work are calculated with $S_p(^{23}Mg) = 7580.9(7)$ keV [3, 76, 114]. The relative intensities are normalized to the observed number of 451 keV γ-rays, and the absolute branching is based on $I_{\gamma,abs.}(451) = 43.3(10)\%$ from [93]. The uncertainties quoted for the decay energies are quadratic sums of the uncertainties from the calibration and the fit. Uncertainties from the calibration dominate in the region where no background reduction was made, whereas in the background-subtracted region the fitting error impacts the uncertainty.

		$E_{ex}(^{23}Mg)$ (keV)			
$E_{meas.}$ (keV)	$E_{p,cm}$ (keV)	Present	Adopted[1]	Relative intensity	Absolute branching (%)
214(11)	206(11)	7787(11)	7786.86(53)[2]	0.32(6)	0.14(3)
273(9)	267(9)	7848(9)	7854.8(12)	0.42(8)	0.18(4)
341(15)	337(15)	7917(15)		0.08(2)	0.03(1)
446(15)	443(15)	8024(15)	8017.2(12)	0.04(2)	0.02(1)
579(8)	579(8)	8160(8)	8163.3(12)	0.65(2)	0.28(1)
861(8)	866(8)	8447(8)	8453(5)	0.95(3)	0.41(1)
1194(8)	1204(8)	8785(8)	8793(8)	0.04(1)	0.02(1)
1326(9)	1338(9)	8919(9)	8916(6)	0.06(1)	0.02(1)
1405(10)	1419(10)	8999(10)	8990(6)	0.04(1)	0.02(1)
1546(9)	1561(9)	9142(9)	9138(6)	0.06(1)	0.03(1)
1712(25)	1729(25)	9310(25)	9328(8)	0.04(1)	0.02(1)
1824(9)	1843(9)	9424(9)	9420(8)	0.11(1)	0.05(1)
					$\Sigma = 1.22(5)$ %

[a] Latest evaluation of A=23, Ref. [91]
[b] Weighted average of Refs. [91,93]

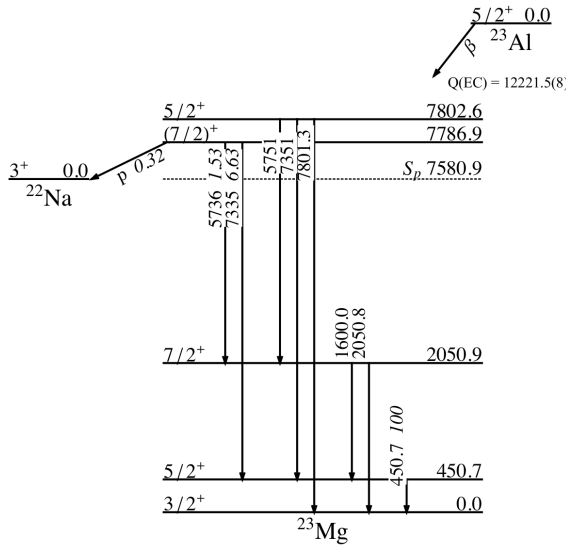

Figure 5.7: Partial level scheme of ^{23}Mg. The transition intensities (in italics, percents relative to the 451 keV line) for the astrophysically relevant 7787 keV state are shown; γ intensities and energies are from Ref. [93] and the proton intensity from this work.

energies higher than 200 keV, apart from the 1931(14) keV group, which was identified in Ref. [48]. In addition, we find a small peak with $E_{\mathrm{p,cm}} = 337(15)$ keV in the tail of the larger 267(9) keV peak. A higher statistics measurement with the same or better resolution should be made to clarify its existence. In previous reaction studies, the excitation energy region of this peak has either been covered by a contamination peak (in ^{25}Mg(p,t) [115]) or been unobserved (in ^{24}Mg(p,d) [116]). We also identify six proton groups ($E_p > 1200$ keV) from levels that have only been observed so far in a ^{25}Mg(p,t) measurement [115] and most of these higher proton groups have been confirmed at IGISOL [117, 118] .

Table 5.5: Proton energies and intensities obtained in this work compared to the results from previous β-decay studies. All energies are quoted in the center-of-mass system. Here the intensities from the present work and from Ref. [48] are quoted relative to the 866-keV line to conform with the convention in Ref. [47].

$E_{p,cm}$ (keV)			Relative intensity		
Ref. [47][1]	Ref. [48][1]	Present	Ref. [47]	Ref. [48][2]	Present[3]
233(20)	209(20)	206(11)	2.2(5)	0.10(8)	0.34(6)
298(20)	282(20)	267(9)	0.9(3)	0.13(9)	0.45(9)
		337(15)			0.08(3)
	418(20)	443(15)		0.13(9)	0.04(2)
585(5)	579(7)	579(8)	0.7(1)	0.73(49)	0.69(3)
877(5)	877(6)	866(8)	1.0	1.0	1.0
		1204(8)			0.04(1)
		1338(9)			0.06(1)
		1419(10)			0.05(1)
		1561(9)			0.06(1)
		1729(25)			0.04(1)
		1843(9)			0.11(1)
	1939(14)			0.06(5)	

[1] Originally reported as laboratory energies.

[2] Originally reported as intensities relative to 451 keV γ-line.

[3] Calculated from intensities presented in Table 5.4.

5.3.3. The case of missing ^{22}Na

The composition of the nova ejecta between ^{20}Ne and ^{27}Al depends greatly on the cyclic nuclear-reaction chains beyond the CNO cycle: namely, the so-called NeNa and MgAl (pseudo-)cycles. The MgAl cycle is crucial for the synthesis of ^{26}Al ($T_{1/2}$ = 0.7 My) and the NeNa cycle is relevant for the synthesis of ^{22}Na ($T_{1/2}$ = 2.6 y). Both ^{26}Al and ^{22}Na could be detected by space-based γ-ray telescopes through their characteristic γ-rays following β-decay. The short half-life of ^{22}Na raises the possibility of detecting it as a point-like source since it decays before spreading away from the site of its synthesis. The amount of ^{22}Na created in novae may also be relevant for explaining non-standard ^{22}Ne abundances in the Ne-E meteorites [119].

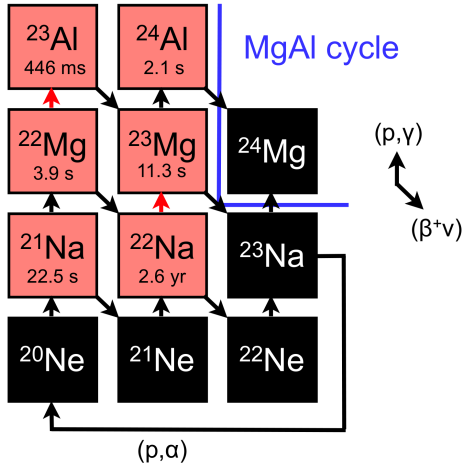

Figure 5.8: NeNa-cycles and possible depleting reactions. The black boxes present stable and the red ones β-emitting nuclei.

So far, there are no confirmed observations of γ-rays of novae origin [120, 121]. However, there is a recent, disputed report about the possible detection of the 1275 keV line from the decay of ^{22}Na, but it appears to originate from a diffuse (not point-like) source, most likely from the photo-activation of ^{22}Ne by cosmic rays [122]. The NeNa cycle, illustrated in Fig. 5.8, proceeds along the path of stable nuclei via the reaction chain: ^{20}Ne(p,γ)^{21}Na($\beta^+\nu$)^{21}Ne(p,γ)^{22}Na($\beta^+\nu$)^{22}Ne(p,γ)^{23}Na(p,α)^{20}Ne. When the temperature rises, however, proton capture starts to compete with β decay and the proton-capture reactions move the reaction products higher in mass, bypassing ^{22}Na. This leads eventually into the MgAl cycle and to a reduced abundance of ^{22}Na in the

end products. The rates of these depleting reactions have been of considerable interest, and recent studies include ^{21}Na(p,γ)^{22}Mg [123, 124], ^{22}Mg(p,γ)^{23}Al [109, 110], ^{22}Na(p,γ)^{23}Mg [46–48, 92, 111, 125–128], ^{23}Na(p,γ)^{24}Mg [129] and ^{23}Mg(p,γ)^{24}Al [130].

The observed state at $E^* = 7787$ keV in ^{23}Mg makes the largest contribution to the astrophysical reaction rate in ^{22}Na(p,γ)^{23}Mg. Typical temperatures in ONe-novae are in the region of 0.1-0.4 GK and therefore states up to about 0.9 MeV above the proton separation threshold in ^{23}Mg may contribute to the radiative proton capture in ^{22}Na(p,γ)^{23}Mg. However, in practice, the dominant resonances are in the lower end of the Gamow window, where the total width is dominated by the γ-ray partial width. Here the meaningful region is in the neighborhood of the IAS in ^{23}Mg.

Since the 7787-keV state is fed in allowed β-decay, the positive-parity assignment is solid, as shown in Ref. [92]. Given the selectivity of β decay, the possible spins for this state are 3/2, 5/2 or 7/2. A spin of 3/2 is excluded by the observation of the proton emission to the $J^\pi = 3^+$ ground state of ^{22}Na, since that would require the proton to carry away an angular momentum of L=2. The $5/2^+, T = 3/2$ IAS is only 16 keV higher than the 7787-keV state and another state with same spin and parity would cause strong mixing between these states. However, it has been demonstrated that the $A = 23, T = 3/2$ isobaric multiplet, of which the state at 7803 keV is the $T_z = -1/2$ member, obeys the isobaric multiplet mass equation (IMME) to a high precision [76]. Therefore we rule out a spin of 5/2 for the 7787-keV neighboring state and assign it spin-parity $(7/2)^+$. This is more restrictive than the currently accepted spin-parity for the 7787-keV state $(7/2^+)$ [91]. Based on the proton intensity we observed for the decay of this state and the γ-ray intensities determined in Ref. [93], we obtain a proton branch for this state of 3.7%, and γ-branchings of 78.2% and 18.% to the 451-keV and 2050-keV states, respectively. The relevant part of the decay scheme is shown in Fig. 5.7.

The lifetime of the 7787-keV state has been measured to be $\tau = 10(3)$ fs from in-beam γ-spectroscopy [111]. Using that lifetime and our measured proton and γ branchings, we derive $\Gamma_\gamma = 63(20)$ meV, $\Gamma_p = 2.5(11)$ meV and a resonance strength $\omega\gamma = 1.4^{+0.5}_{-0.4}$ meV. This resonance strength agrees with the old value of 1.8(7) meV from the first direct measurement reported by Stegmüller *et al.* [127]. However, it differs substantially from the more recent direct measurement by Sallaska *et al.* [46, 128] who measured $\omega\gamma = 5.7^{+1.6}_{-0.9}$ meV for the 7787 keV state, 3.2 times larger than the older result. The difference between the latest direct measurement and the earlier one are discussed in detail in Ref. [128] and in the following only the possible sources of difference compared to our work are discussed.

The resonance strength we obtained is based on indirect information and combines data from several different experiments. The lifetime of the 7787 keV state was determined by Jenkins et al. [111] who used the Doppler-shift-attenuation method (DSAM) [131] under the assumption that feeding to this high-lying unbound state is direct. DSAM is most sensitive in the range from a few fs to a few tens of fs, which coincides with the observed life-time for the state. However, the uncertainty quoted for this lifetime was 3 fs and represents the major contribution to the uncertainty for the $\omega\gamma$ result derived in this work.

The γ-ray intensities for the 7787 keV state determined in [92, 93] were obtained with the same instruments and techniques used for other high-precision β-decay branching-ratio measurements (see e.g. [132] and references therein). The resultant γ-ray branching ratios disagree only slightly with those reported by Sallaska *et al.* [128]; but they differ considerably from those determined by Jenkins *et al.* [111], who attribute some of the γ-lines to a nearby state, which has not been found in any direct measurement, nor was it observed in any β-decay experiments.

The relative proton intensities determined in this work may suffer from the fact that a significant background had to be subtracted in order to analyze the low-energy peaks. It is also worth noting that our uncertainties for the low-energy proton peak intensities are at best just under 20%, yet their contribution to the total error of the resonance strength is small compared with the contribution from the uncertainty in the lifetime. Furthermore, our proton intensity relative to the 451 keV γ-ray line is already somewhat higher than Peräjärvi *et al.* [48] and it is unlikely that we have lost any significant amount of the proton intensity in the lowest-energy proton groups. Therefore, if the resonance strength of the 7787 keV state is indeed as high as claimed in Ref. [46], then the lifetime of the 7787 keV state should be less than its present value.

All in all, given the discrepancy between the latest direct measurement of $\omega\gamma$, and both our result and that of Stegmüller *et al.* [127], more indirect data is clearly needed to settle this issue. A new, more precise level lifetime measurement for the 7787 keV state is called for. Moreover, a measurement of the lifetime of the 7855-keV state would also be beneficial, since its proton intensity is less sensitive to the background present in our measurement.

Our data is consistent with the earlier high spin assignment, $9/2^+$, of the state at 7769 keV and therefore we confirm that it does not contribute to the astrophysical reaction rate of the radiative proton-capture reaction ^{22}Na(p,γ)^{23}Mg.

5.4. The β-decay of ^{31}Cl

5.4.1. β-delayed protons from ^{31}Cl

The DSSSD calibration was performed with well known β-delayed proton groups from the decay of ^{29}S. Only three of the groups, at 739.5(9), 1257(10) and 2129.8(9) keV [133] were intense enough for calibrating individual strips. Thus the most intense proton line from ^{31}Cl at 985(6) keV (weighted average of all previous studies as given in Ref. [134]) was also included as an internal calibration. These lines yield a calibration which has an uncertainty of about 3 - 4 keV over the whole range.

The total spectra of ^{29}S and ^{31}Cl, acquired by tuning each of the species into the middle of the W1(69) type DSSSD (setup I), are illustrated in the top panel of Fig. 5.9. At the used rigidity ^{29}S has only a slightly longer range in Si than ^{31}Cl and thus it also stops in the DSSSD when ^{31}Cl is centered. In this case all the ^{29}S lines are shifted about 10 keV compared to the situation when ^{29}S is centered (in Fig. 5.9, seen best from the 2129 keV line). This follows naturally from the fact that ^{29}S decays closer to the triggering Si-pad and thus preceding positrons leave less energy to be piled up during proton detection. When ^{29}S is centered, only the strongest ^{31}Cl proton lines from decays occurring in the degrader are visible. The lower panel of Fig. 5.9 shows the total spectra collected for ^{31}Cl with 45 μm BB2 and 69 μm W1 DSSSDs. The BB2 spectrum is cut below 500 keV due to high thresholds in electronics caused by noise conditions during most of the experiment. However, the spectrum collected with BB2 helps to identify some of the weaker proton groups that are harder to see in the spectrum acquired with W1.

As in this case intense high energy protons were present, the fit function of each line beyond one MeV has to include an escape tail. This is not only to account for the efficiency, but also to take into account piling up of the escaping protons with the lower lying proton groups. The shape of the escape tail for each peak was determined from Geant4 simulations and the shape was fixed for the fit. The minimal fit to the spectrum is established with an exponential background and a total of 20 proton groups. Of these, four can be identified to belong to ^{29}S and rest to ^{31}Cl. The resulting proton energies are given in the laboratory frame and compared to previous works in table 5.6. The relative intensities extracted from the fit are given in table 5.7. Four of the proton groups observed in this work cannot be associated with any known weaker proton groups for ^{29}S. So, they are assigned to ^{31}Cl. It is good to note that these lines are fairly weak and the β-tail of larger peaks smears them, so these groups should be treated as tentative assignments.

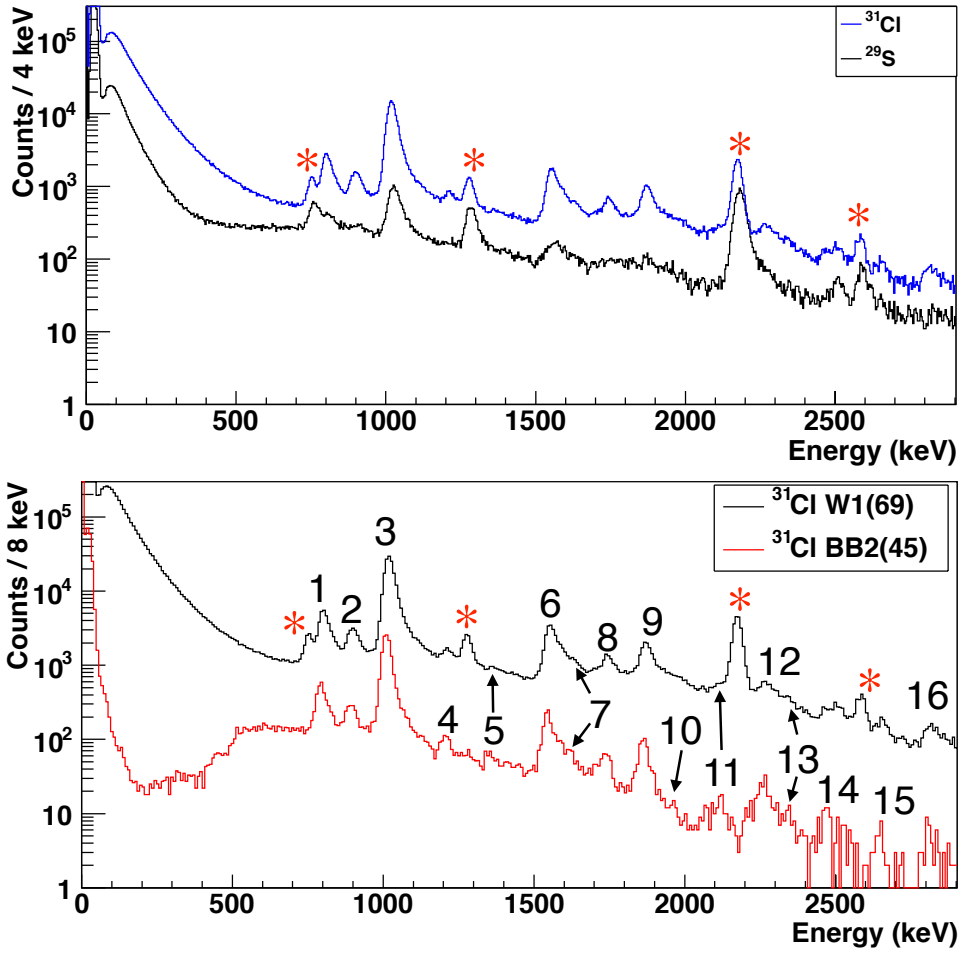

Figure 5.9: β-delayed protons from decays of ^{29}S and ^{31}Cl. Top panel shows the spectra when either ^{31}Cl or ^{29}S are centered in the 69 μm thick DSSSD. The bottom panel shows the spectra collected for ^{31}Cl with the 45 μm BB2 and the 69 μm W1 DSSSDs. The BB2 spectrum is cut below 500 keV due to high thresholds in the electronics caused by noise conditions during most of the run. Peaks marked with a red asterisk are identified to originate from the known decay of ^{29}S [133]. The rest are assigned to the decay of ^{31}Cl.

Table 5.6: Comparison of proton energies from ^{31}Cl decay. All energies are given in E_{lab} as in previous works, in units of keV. The average value is the weighted average of all the works presented in this table. The corresponding level energy is determined by assuming decay to the ground state of ^{30}P and using the calculated average proton energy with $S_p(^{31}\mathrm{S}) = 6130.92(38)$ keV [3, 102].

Ref. [135]	Ref. [136]	Ref. [137]	Ref. [134]	This work	Average	E_{lev}
			762(14)	780(2)	780(2)	6936(2)
	845(30)		853(18)	877(2)	876(2)	7036(2)
989(15)	986(10)	986(10)	978(15)	993(2)	993(2)	7157(2)
	1173(30)		1175(19)	1185(3)	1185(3)	7355(3)
				1345(17)	1345(17)	7521(17)
1528(20)	1520(15)	1524(10)	1521(20)	1520(3)	1521(3)	7702(3)
				1594(17)	1594(17)	7778(17)
	1695(20)		1688(22)	1706(3)	1706(3)	7894(3)
	1827(20)		1825(23)	1830(3)	1830(3)	8022(3)
				1927(17)	1927(17)	8122(17)
	2113(30)		2075(30)	2070(17)	2079(13)	8279(13)
	2204(30)		2217(30)	2224(3)	2224(3)	8429(3)
			2299(30)	2286(17)	2289(15)	8496(15)
			2454(40)	2489(17)	2484(16)	8697(16)
			2601(40)	2641(17)	2635(16)	8854(16)
			2751(40)	2807(17)	2799(16)	9023(16)

Table 5.7: Relative proton intensities $I_{p,rel.}$ from the decay of ^{31}Cl normalized to the 993(2) keV proton group and to the 2234 keV γ-line. Peak number refers to labels in the bottom panel of Fig. 5.9. All energies are E_{lab} in keV and the relative intensities in %.

	This work			Ref. [134]		
Peak no.	E_p	$I_{p,rel.}$	$I_{p/\gamma 2234}$	E_p	$I_{p,rel.}$	$I_{p/\gamma 2234}$
1	780(2)	20.4(2)	0.43(1)	763(14)	9.1(22)	0.10(3)
2	877(2)	12.4(2)	0.26(1)	853(18)	1.2(12)	0.013(13)
3	993(2)	100(4)	2.12(3)	978(15)	100(4)	1.08(14)
4	1185(3)	2.7(1)	0.057(3)	1175(19)	1.7(6)	0.018(7)
5	1345(17)	1.3(12)	0.028(26)			
6	1520(3)	21.0(4)	0.44(1)	1520(20)	13.6(14)	0.15(3)
7	1594(17)	1.4(2)	0.03(4)			
8	1706(3)	6.4(2)	0.136(5)	1688(22)	3.9(7)	0.043(9)
9	1830(3)	10.9(2)	0.231(5)	1825(23)	8.8(11)	0.096(16)
10	1927(17)	1.4(1)	0.031(2)			
11	2070(17)	1.3(1)	0.028(2)	2075(30)	1.3(5)	0.014(5)
12	2224(3)	2.3(1)	0.048(2)	2217(30)	4.1(8)	0.044(10)
13	2286(17)	0.9(7)	0.018(2)	2299(30)	1.5(5)	0.016(6)
14	2489(17)	0.91(6)	0.019(2)	2454(40)	1.0(4)	0.010(4)
15	2641(17)	0.19(4)	0.004(1)	2601(40)	0.4(3)	0.004(3)
16	2807(17)	0.3(1)	0.006(2)	2751(40)	0.6(3)	0.007(4)

5.4.2. β-delayed γ rays from ^{31}Cl

The low energy part of the energy and efficiency calibration of the Ge detector(s) was done by using standard calibration sources. The calibration was extended up to 8 MeV by using known γ rays from ^{32}Cl and ^{28}P decays. Figure 5.10 shows the full γ-ray spectrum collected simultaneously with protons following the ^{31}Cl decay in Fig. 5.9. Most of the transitions shown in Fig. 5.11 have not been observed before in β-decay. So far the most extensive study was presented in Ref. [134], where four transitions at 1249.1(14), 2234.5(8), 3536(2) and 4046(2) keV were assigned to follow the β decay of ^{31}Cl. The observed γ transitions and their comparison to literature are summarized in tables 5.8 and 5.9 and the relative intensities are given in table 5.10.

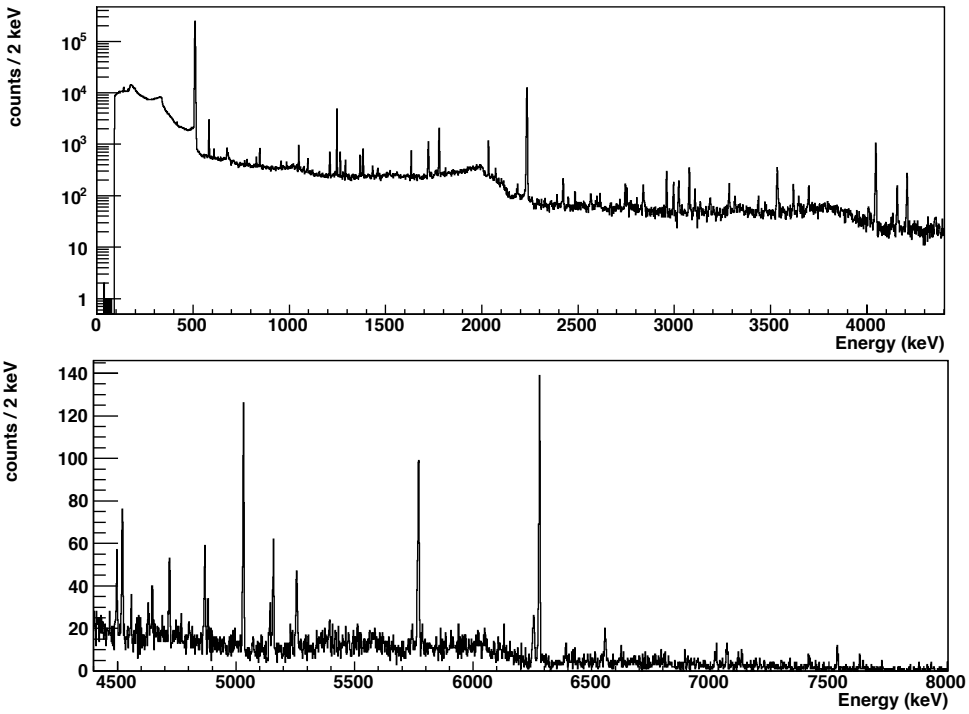

Figure 5.10: β-delayed γ rays from decay of ^{31}Cl. Note that the top panel has a log scale and the bottom panel a linear scale.

A partial level scheme presented in Fig. 5.11 displays γ transitions and levels observed in this work. We base our identification on (i) known existence of the level in literature [134, 138–144] and (ii) observed $\gamma\gamma$ coincidence with setups II and III. Some of the levels can be identified from singles so that two observed transitions sum up to some other level. No $\gamma\gamma$ coincidences were observed for the levels above the lowest $T = 3/2$ state in ^{31}S. Their identification is based only on escape peaks and possible counterparts in literature. No random summing of the strongest transitions was observed (e.g. of the two lowest transitions or summing with the annihilation peak).

In our spectra we also observe γ transitions from species other than ^{31}S. As the final beam purity was only about 85%, we have some contaminants stopped inside the setup so that they produce the γ lines observed. The major impurities expected from the beam identification in Fig. 3.7 are ^{29}S, ^{30}S and ^{28}P. In the γ-ray spectrum of Fig. 5.10 we observe 677 and 709 keV lines corresponding to the first and second excited states in ^{30}P [145]. As there is ^{29}S implanted simultaneously, it is not surprising to observe 1038, 1383 and 2423 keV lines originating from states fed in ^{29}P [138]. βp decay of ^{29}S is known to feed excited states at 1779 and 4617 keV in ^{28}Si [133] providing observed γ lines at 1778 and 2838 keV, respectively. It is good to note that these can originate partly from the decay of contaminating ^{28}P. As ^{31}S is also β unstable we expect to see transitions following its decay, even though the decay mostly feeds the ground state of stable ^{31}P [138]. We observe small peaks at 1265 and 3134 keV. However we cannot resolve the 2232 keV line from the second excited state, as it overlaps with the 2234 keV transition from the second excited state in ^{31}S.

We observe γ lines at 1247.55(25) and 2234.18(17) keV corresponding to the first and second excited states in ^{31}S. We also see a line at 985.5(3) keV, a weak transition between the second and first excited states [138]. As said above, given the weak feeding in β decay and small observed intensities of other lines from ^{31}P we take the 2234.18(1) keV line to be fully from ^{31}S. The line at 3077.1(2) keV originates most likely from a state identified in literature as 3079(11) keV;$1/2^+$ [138] and 3081(5) keV [139]. A line at 846.0(3) keV can be a transition from this level to the second excited state. The line at 3284.6(2) keV originates from the known level identified in literature as 3285.5(5) keV with spin assignment $5/2^+$,$(3/2^+)$ [138], 3286(5) keV [139] and 3285.11(19) keV with $5/2^+$ [140]. A line at 1049.1(1) keV is the transition to the second excited state and the line at 2035.16(4) to the first excited state [138, 140].

The line at 5785.7(7) keV originates most likely from a level identified in literature as 5781(8) keV; $(3/2,5/2)^+$ [138], 5777(5) keV [139], 5781(5) keV; $5/2^+$ [141] and

5779(3) keV; $5/2^+$ [143]. We also note that we do observe a line at 5768.2(5) keV, matching with the first escape of the 6279.5(3) keV line. It is worth noting here that Ref. [134] tentatively assigned the observed 3536(2) keV γ line to originate from this level and feed the second excited state. However it was also discussed that it may be an escape peak of the 4045(2) keV transition. Our observed line at 3534.7(2) keV matches closely with the first escape peak of the 4046.2(2) keV (difference 511.2(3) keV). Interesting enough, when placing a gate on the 2234 keV transition, we do observe a 3540(3) keV line in coincidence as seen in Fig. 5.12. This would match a state at 5774(3) keV. Unfortunately we are not able to resolve such line from the escape peak.

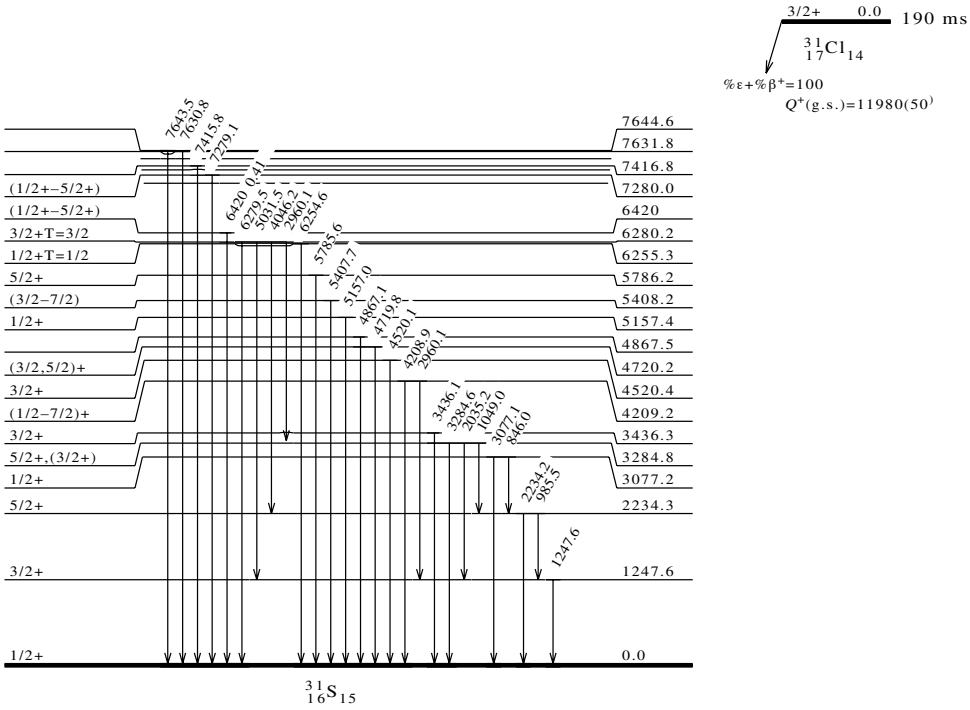

Figure 5.11: Partial level scheme of ^{31}S. Only levels that have a counterpart in literature or could be determined from $\gamma\gamma$ coincidences are shown. Spin assignments are from literature [134, 138–144].

Table 5.8: Observed γ transitions from ^{31}Cl decay below $S_p(^{31}\mathrm{S}) = 6130.92(38)$ keV [3, 102]. Literature data are extracted from the NUDAT/ENSDF database, version of Oct 03, 2011, Ref. [138] unless otherwise stated. All energies are given in keV. Uncertainties in the table for this work are statistical (fit + calibration) only. For systematic uncertainties, add 1.5 keV.

Literature				This work	
E_{level}	J^π	E_γ	E_{final} ; J^π	E_{level}	E_γ
1248.9(2)	$\frac{3}{2}^+$	1248.8(3)	0 ; $\frac{1}{2}^+$	1247.6(3)	1247.6(3)
2235.6(4)	$\frac{5}{2}^+$	986.6(5)	1248.9 ; $\frac{3}{2}^+$	2234.3(2)	985.5(3)
		2235.5(5)	0; $\frac{1}{2}^+$		2234.2(2)
3079.0(11)[1]	$\frac{1}{2}^+$	843.4(12)	2235.6 ; $\frac{5}{2}^+$	3077.2(2)	846.0(3)
		3078.8(12)	0 ; $\frac{1}{2}^+$		3077.1(2)
3285.5(5)	$\frac{5}{2}^+$ [2]	1050.4(2)[2]	2235.6 ; $\frac{5}{2}^+$	3284.8(3)	1049.1(1)
		2035.8(2)[2]	1248.9 ; $\frac{3}{2}^+$		2035.2(2)
		3285.3(11)[2]	0 ; $\frac{1}{2}^+$		3284.6(2)
3437(7)	$\frac{3}{2}^+$	2188.1(7)	1248.9 ; $\frac{3}{2}^+$	3436.3(7)	2186.6(3)
		3436(8)	0 ; $\frac{1}{2}^+$		3436.1(7)
4204(7)	$(\frac{1}{2} - \frac{7}{2})$		1248.9(2) ; $\frac{3}{2}^+$	4209.2(2)	2960.1(1)
			0 ; $\frac{1}{2}^+$		4208.9(2)
4525(8)	$\frac{3}{2}^+$			4520.4(3)	4520.1(3)
4718(6)	$(\frac{3}{2}, \frac{5}{2})^+$			4720.2(4)	4719.8(4)
4866(7)	$(\frac{1}{2} - \frac{5}{2})^+$[3]			4867.5(3)	4867.1(3)
5151(6)	$(\frac{1}{2} - \frac{5}{2})^+$[3]			5157.4(3)	5157.0(3)
5408(9)	$(\frac{1}{2} - \frac{5}{2})^+$[3]			5408.2(9)	5407.7(9)
5775.1(15)[4]	$\frac{5}{2}^+$[4]	3536(2) [5]		5774(3)[6]	3540(3)[6]
					5768.2(5)[7]
					5785.7(7)[8]

[1] In Ref. [139] 3081(5) keV. [2] From Ref. [140].

[3] J^π assignment from this work based on β selection rules.

[4] Adopted by Ref. [143] as a weighted average for energy and the assignment based on all preceding known work [134, 138, 139, 141, 143].

[5] Tentative assignment in Ref. [134], overlaps with 4045(2) keV escape.

[6] A matching line in coincidence with the 2234 keV line. Unable to resolve a singles line due to a close lying escape peak as in Ref. [134].

[7] Most likely the first escape of 6729.5(3) keV line at this energy.

[8] Falls within the uncertainties of 5781(8) keV [138] and 5781(5) keV [141].

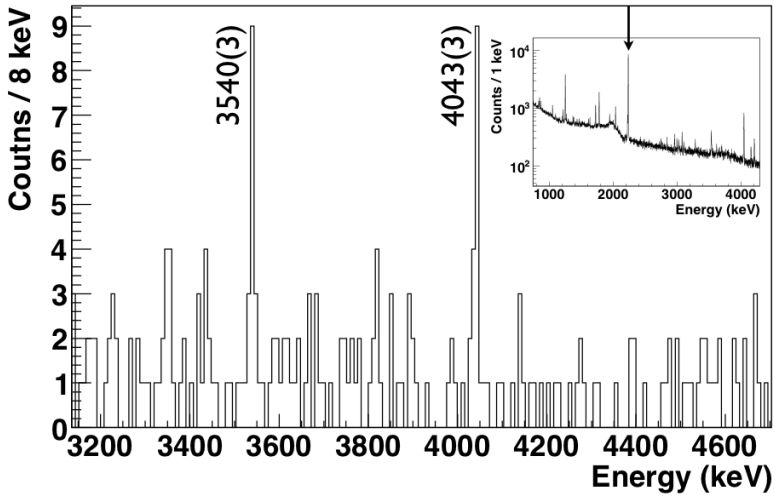

Figure 5.12: The 4046 keV transition in coincidence with the 2234 keV transition (inset) from setup III. Surprisingly the peak at 3540(3) keV appears also to be in coincidence with the 2234 keV transition. See text for discussion.

The observations above the $S_p(^{31}\mathrm{S}) = 6130.92(38)$ keV [3, 102] are most interesting, as precise determination of the level energies translates to precise resonance energies for astrophysics. Here we observe a line at 6254.6(5) keV which originates likely from a state identified in literature as 6267(10) keV; $1/2^+$ [138], 6267(5) keV; $1/2^+$ [141], 6259(2) keV; $1/2^+$ T=1/2 [142, 143], 6260(1) keV; $1/2^+$ [144]. The line at 6279.5(3) keV is identified to originate from the known $T = 3/2, 3/2^+$ IAS of ^{31}Cl ground state identified previously at 6268(10) keV [138], 6283(2) keV [142, 143] and 6284(1) keV [144]. We observe a γ transition at 4043(3) keV in coincidence with the 2234 keV transition (Fig. 5.12) and thus confirm the observation of the 4045(2) keV transition of Ref. [134] assigned to originate from the IAS. From a singles spectrum we extract an energy of 4046.2(2) keV for this transition. In addition we observe two other transitions with energies 2995.6(2) and 5031.5(3) keV that can be matched to originate from the IAS.

Above the IAS there are still quite a few interesting transitions for which we cannot assign any coincidences or other transitions that could sum up to similar energy. The most interesting feature is a pair of peaks with energies of 7630.8(6) and 7643.5(8) keV. As seen in Fig. 5.13, both lines have clear first and second escape peaks and no counterparts from possible contaminants exists. In literature only reported

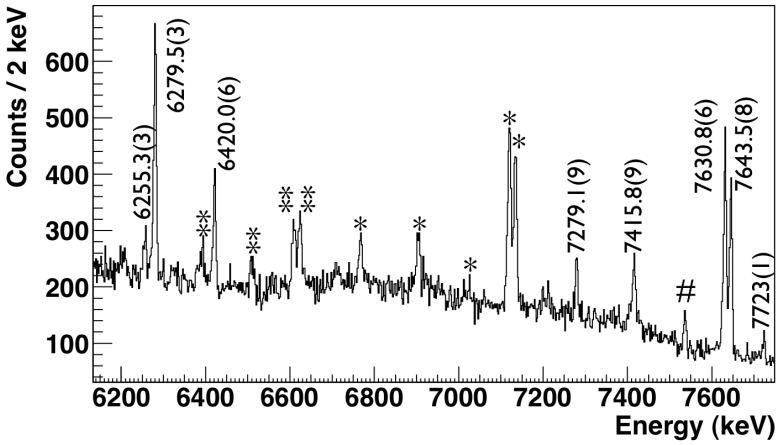

Figure 5.13: Observed γ ray spectrum above $S_p(^{31}\mathrm{S})$ taken with setup III, with both HPGe detector spectra summed for increased statistics. Identified escapes are marked with "$*$" and "$**$" for first and second escapes, respectively. Possible contamination from ^{28}Si is denoted with #.

matching states are at 7600(30) and 7660(30) keV from a (^{3}He,α) measurement reported in Ref. [146]. Also, for the latter state, there is a close correspondence at 7641(3) keV from a (^{3}He,t) reaction reported in Ref. [143]. However the assignment for this level is ($\frac{5}{2} - \frac{13}{2}^-$), which would not be fed in allowed β decay. No literature counterparts were found for lines at 6420.0(6), 7279(1), 7415.8(9) keV lines, nor could those be identified to be any escape peaks. We assign these tentatively to originate from corresponding states in ^{31}S.

Table 5.9: Observed γ transitions from ^{31}Cl decay above $S_p(^{31}\mathrm{S}) = 6130.92(38)$ keV [3, 102]. Literature data are extracted from the NUDAT/ENSDF database, version Oct 03, 2011, Ref. [138] unless otherwise stated. All energies are given in keV. Uncertainties in the table for this work are statistical (fit + calibration) only. For systematic uncertainties, add 1.5 keV.

Literature			This work		
E_{level}	J^π	E_γ	E_{level}	E_γ	E_{final} ; $J^{\pi\,1}$
6259(2)[2]	$\frac{1}{2}^+, T = \frac{1}{2}$		6255.3(5)	6254.6(5)	0 ; $\frac{1}{2}^+$
6281.2(14)[3]	$\frac{3}{2}^+, T = \frac{3}{2}$		6280.2(3)	2995.6(2)	3284.8(3) ; $\frac{5}{2}^+$
		4045(2)[4]		4046.2(2)[5]	2234.3(2) ; $\frac{5}{2}^+$
				5031.5(3)	1247.6(3) ; $\frac{3}{2}^+$
				6279.5(3)	0 ; $\frac{1}{2}^+$
			6420.7(6)[6]	6420.0(6)	
			7280(1) [6]	7279(1)	
			7416.8(9) [6]	7415.8(9)	
7600(30)[7]			7631.8(6)	7630.8(6)	
7660(30)[7,8]			7644.6(8)	7643.6(8)	

[1] J^π from literature, see table 5.8. [2] From Ref. [142, 143]. [3] Adopted by Ref. [143] as weighted average of all known works [134, 138, 139, 141, 143].
[4] From Ref. [134]. [5] Energy from a singles measurement.
[6] Tentative assignment, no escapes or coincidences detected. No counterpart in literature. [7] Value in the evaluation in Ref. [138] based on (^{3}He,α) measurement reported in [146]. [8] Ref. [143] has ($\frac{5}{2} - \frac{13}{2}^-$) at 7641(3) keV.

Table 5.10: Relative gamma intensities from the decay of ^{31}Cl normalized to the 2234.2(2)keV line.

This work		Ref. [134]		
E_γ	$I_{\gamma/\gamma 2234}$	E_γ	$I_{\gamma/\gamma 2234}$	
846.0(3)	1.7(1)			
985.5(5)	0.3(1)			
1049.0(3)	2.1(1)			
1247.6(3)	24.0(3)	1249.1(14)	32(7)	
2035.2(2)	7.2(3)			
2186.6(3)	0.5(1)			
2234.2(2)	100(1)	2234.5(8)	100(12)	
2960.1(2)	2.6(2)			
2995.6(3)	1.9(1)			
3077.1(2)	3.5(2)			
3284.6(3)	1.7(2)			
3436.1(7)	0.8(1)			
3534.7(3)	5.7(2)	3536(2)	26(8)	Possible 1st escape of 4046
4046.2(2)	16.0(4)	4045(2)	14(6)	
4208.9(3)	4.2(2)			
4520.1(3)	1.3(1)			
4719.8(4)	0.9(1)			
4867.1(4)	1(1)			
5031.5(3)	2.4(2)			
5157(4)	1.2(1)			
5407.7(9)	0.01(1)			
5785.6(8)	0.3(1)			
6254.6(5)	0.7(1)			
6279.5(3)	3.2(2)			
6389.7(11)	0.24(7)			
6420(7)	0.15(9)			
7279.1(10)	0.09(7)			
7415.8(10)	0.15(6)			
7630.8(7)	0.15(5)			
7643.5(8)	0.09(5)			

5.4.3. On proton-gamma coincidences

Given the small proton branching ratios and the fact that the γ detection efficiency is at the per mil level at best, it is not surprising that only a few (mostly random) counts appear in γ ray spectra gated with some of the proton groups. The lowest energy proton group from ^{29}S, at 739.5(9) keV is known to feed the 1779 keV state in ^{28}Si [133]. By setting a gate on the aforementioned proton group in the ^{31}Cl spectrum, as shown in the inset of the left panel in Fig. 5.14 we do observe a clear line at 1778 keV in the γ spectrum. When correcting for the γ detection efficiency, the number of observed γ rays roughly equals the number from a fit to the proton group, demonstrating that the proton-γ coincidence in our setup works. When setting a gate to the 1185(3) keV proton group, shown in the right panel of Fig. 5.14 we do not observe 677 or 709 keV γ lines corresponding to the first and second excited state in ^{30}P. However, interestingly there are a few (total of five, even at 1 keV/bin) excess counts at 1454 keV, corresponding to the third excited state in ^{30}P [145]. With present statistics we cannot say anything conclusive, but this indeed suggests that the proton group at 1185(3) keV could originate from a higher state in ^{31}S as proposed in Ref. [143].

5.4.4. Half-life of ^{31}Cl

The half-life of ^{31}Cl was determined with a proportional counter and tape transport system (setup IV). A total of $6 \cdot 10^6$ events, including both ^{31}Cl and the daughter ^{31}S decays, from 17 different runs were used to obtain $T_{1/2} = 190(1)$ ms. This deviates from the previous value of 150^{+25}_{-20} ms determined in Ref. [147]. However, it should be noted that the previous value was determined from a source produced with the He-jet technique without any mass separation, having significant ^{32}Cl contamination.

5.4.5. Bottleneck reaction in ONe novae: ^{30}P(p,γ)^{31}S

At the typical nova peak temperatures of 0.1 - 0.4 GK, the nova nucleosynthesis proceeds through a series of capture reactions (mainly radiative proton capture) and β-decay. A long β-decay half-life can become a "bottleneck" for the reaction path, allowing nucleosynthesis to proceed only via capture reactions. One such nucleus with a long enough half-life is ^{30}P ($T_{1/2} = 2.498(4)$ min [145]), making it a mandatory passing point towards ^{32}S. The nucleosynthesis can proceed further via $^{30}\mathrm{P}(\mathrm{p},\gamma)^{31}\mathrm{S}(\mathrm{p},\gamma)^{32}\mathrm{Cl}(\beta^+)^{32}\mathrm{S}$ or via $^{30}\mathrm{P}(\mathrm{p},\gamma)^{31}\mathrm{S}(\beta^+)^{31}\mathrm{P}(\mathrm{p},\gamma)^{32}\mathrm{S}$ [45]. Theo-

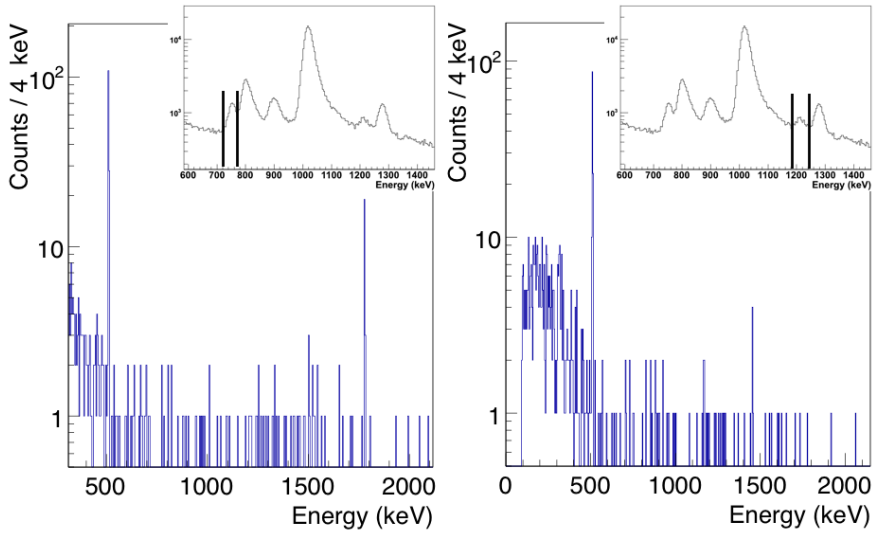

Figure 5.14: Coincident γ rays from different proton groups. The left panel shows coincident γ rays observed when a gate (in the inset) is set to the lowest energy proton group of ^{29}S, known to feed the 1779 keV level in ^{28}Si [133]. The right panel shows coincident γ rays observed when a gate (in the inset) is set to the 1185(3) keV [134] proton group.

retical calculations, based on several hydrodynamic nova simulations show that if the ^{30}P(p,γ) rate is reduced by a factor of 100, an enhancement in ^{30}Si is obtained [43, 45]. The final abundance pattern obtained in the calculations is important in understanding the abundances of the observed nova ejecta in the S-Ca region. For example, high ^{30}Si/^{28}Si and close-to-solar ^{29}Si/^{28}Si abundance ratios observed in pre-solar grains point towards nova origin [148]. The observed isotopic ratios can also be used to distinguish between the composition of the white dwarf companion and they are thought to be good indicators of attained peak temperature during the TNR [149].

A short half-life of ^{30}P prevents fabrication of such targets and so far there are no intense enough beams of ^{30}P available for direct measurements of ^{30}P(p,γ)^{31}S. Until recently, the reaction rate of ^{30}P(p,γ)^{31}S in ONe novae has been based only on a statistical model (Hauser-Feshbach) with large uncertainties [43, 45]. In recent years, several studies have made improvements for the spectroscopic information about the excited states in ^{31}S at the relevant energy range [134, 140–144, 150]. In

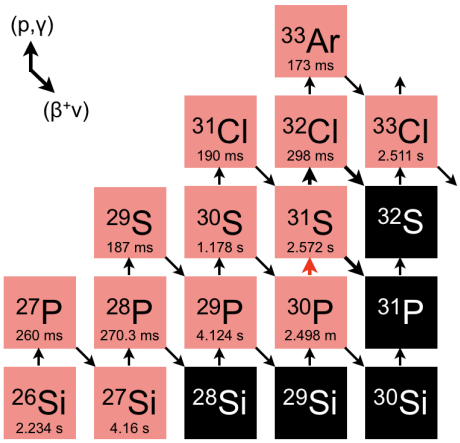

Figure 5.15: Reactions in the $A = 30$ region. The relatively long half-life of ^{30}P makes it a mandatory passing point on the way to ^{32}S and beyond at typical nova temperatures. The black boxes present stable and the red ones β-emitting nuclei.

Refs. [140, 150], Jenkins et al. used a $^{12}C(^{20}Ne, n)^{31}S$ reaction with in-beam γ-ray spectroscopy to produce several high-spin states upon which an extensive level scheme was built. Kankainen et al. reported in Ref. [134] a study of β-delayed protons and γ-rays from the decay of ^{31}Cl, produced as an isobarically pure source. Ma et al. used the $^{32}S(p, d)^{31}S$ reaction with a high resolution spectrometer in Ref. [141] where they reported total of 26 excited states in ^{31}S, including five new states. The $^{31}P(^{3}He, t)^{31}S$ reaction has been used three times in Refs. [142–144] where also a high-resolution spectrometer was used. In Ref. [143] a total of 17 new levels and 5 new tentative levels in ^{31}S were reported by Wrede et al. and Parikh et al. placed more constraints on the J^{π} for several states in Ref. [144]. Our decay data about the states above the $S_p(^{31}S)$ can be used in combination to these latest data to improve the knowledge on the resonances of ^{30}P(p,γ)^{31}S in novae.

Members of the $A = 31, T = 3/2$ isospin quartet are presented in table 5.11. A quadratic fit with the isobaric multiplet mass equation (2.3) to the $T_3 = 3/2, 1/2$ and -1/2 members of the multiplet yields coefficients that can be used to extrapolate the mass of ^{31}Cl. From the fitted coefficients, we obtain a predicted value for the mass excess of the ^{31}Cl ground state to be -7056.8(33) keV. This value agrees with the experimental value of -7070(50) keV [151] and also improves the $Q_{EC}(^{31}Cl)$ and $S_p(^{31}Cl)$ to be 11985.8(33) keV and 282.8(44) keV, respectively. The latter is important for the ^{30}S(p,γ)^{31}Cl reaction in novae and X-ray bursts.

However, a direct mass measurement of ^{31}Cl is needed to establish the ground state mass excess and to check the validity of the IMME in the $A = 31, T = 3/2$ quartet. This confirmation is required, especially when considering the case of $A = 32, T = 2$ quintet discussed earlier (see sec. 5.2.1). In the latter multiplet the quadratic IMME has been observed to break with high precision. On the other hand, in the $A = 32$ case the closest non-analogue state ($T = 0, 1^+$), from where most of the isospin mixing is originates, is only about 188 keV away [105]. In ^{31}S the closest known $T = 1/2, 3/2^+$ state is over 700 keV away [138,152], reducing the strength of possible isospin mixing in the $A = 31$ case.

Table 5.11: The members of the $A = 31$, $T = 3/2$ quartet.

Nuclide	$T_{1/2,\text{g.s.}}$	T_3	$ME_{\text{g.s.}}$ (keV)	E_{ex} (keV)	$ME_{\text{T=3/2}}$ (keV)
^{31}Si	157.3(3) m[1]	+3/2	-22949.036(43)[2]	–	-22949.036(43)
^{31}P	stable	+1/2	-24440.44128(68)[2]	6380.8(17) [1]	-18059.7(17)
^{31}S	2.572(13) s [1]	-1/2	-19042.55(24) [3]	6280.2(16)[4]	-12762.4(16)
^{31}Cl	190(1) ms [4]	-3/2	-7066(50)[2,5]	–	-7066(50)

[1] From Ref. [138]. [2] From AME2011 preview, Ref. [4]. [3] From Ref. [102]
[4] This work. [5] Value in AME03 (Ref. [3]) is -7070(50) keV, based on a reaction measurement in Ref. [151].

6. Summary and Outlook

In this work results of testing a cryogenic ion guide were presented. The successful tests have led to a full-scale prototype gas catcher, being tested on-line at GSI during this fall. Also, it was shown that observed contaminant stable mass beams at standard operational conditions at IGISOL can be improved when going to cryogenic operation. This can improve possibilities for mass measurements, or using the JYFLTRAP as a mass filter in mass regions that traditionally contain significant amounts of stable beam components originating from impurities in the system.

The β-decay experiments reported here were a part of the development work of a β-decay setup for the MARS focal plane. In addition to the studies of ^{23}Al and ^{31}Cl reported in this thesis, further studies have been done for β-decays of ^{20}Mg and ^{27}P, both being relevant for explosive hydrogen burning scenarios. The setup would benefit from having a smaller strip volume for the DSSSD. Adding time correlation for the implantation would enable the observation of the detailed history of each implanted ion, cleaning the spectrum further.

The experimental results of this work include the first direct mass measurement of ^{23}Al. The new value for the mass is two orders of magnitude more precise than the previous value. The newly determined mass was used to test the isobaric multiplet mass equation with high precision in the $A = 23, T = 3/2$ isobaric multiplet. A good agreement between theory and experimental values was found.

The study of the β-decay of ^{23}Al brought new information to the discrepancy between earlier measurements concerning proton emission from the IAS in ^{23}Mg. Contrary to previous works [47,48], the lowest detectable proton group was assigned to a state 16 keV below the IAS. Based on this assignment, it was possible by combining our results with existing data [92,93], to determine simultaneously proton and γ decay branches from the same state, allowing determination of the resonance strength of the astrophysically most relevant resonance by completely indirect data. The result was in agreement with the older direct determination [127], but disagreeing with latest direct experiment [46].

The high statistics study of the β-decay of ^{31}Cl confirmed several of the results of Ref. [134]. In addition a couple of new proton groups were observed. Several states

in ^{31}S were observed in β-decay for the first time, including the IAS of ^{31}Cl. The results constrain the possible J^{π} of the states observed. The improved energy of the IAS was used in addition with the latest experimental data as an input for the IMME to determine indirectly the ^{31}Cl mass, S_p and Q_{EC}. In addition, through $p-\gamma$ coincidences, the βp decay of ^{29}S was observed to feed excited states in ^{28}Si as interpreted so far only by known levels in ^{29}P by Ref. [133].

Classical novae are becoming the first stellar phenomena where an understanding of nucleosynthesis can rely on experimental nuclear physics input [38, 39]. The latest review on the status of nuclear astrophysics in Ref. [39] points out that one of the open key questions is: "What causes the discrepancy between models and observations regarding the mass ejected during classical nova outbursts?" The main interest in the nuclear physics part, related to this question, is concentrating on the reactions ^{18}F(p,α)^{15}O, ^{25}Al(p,γ)^{26}Si and ^{30}P(p,γ)^{31}S. The energies and spin-parities of the states above S_p(^{31}S) obtained this work can be used to constrain the results from reaction studies to improve the understanding of the ^{30}P(p,γ)^{31}S reaction.

In the end, it should be noted that the experiments are only as good as their calibrations. The calibrations of this work rely entirely on work done in the 1970's (^{21}Mg in Ref. [112] and ^{29}S in Ref [133]). The data presented in the literature is extremely good technically, but all of it is obtained from a non-mass-separated source. For example, the lowest observed proton group following the decay of ^{31}Cl was identified from a mass-separated source first time in Ref. [134] and now confirmed here. So the question arises, how much else there is missing or has been misidentified? A systematical study using advances in detector technologies (see e.g. Ref. [153–155]) coupled to excellent mass separation techniques available today could reveal something new about the nuclei in this region.

A. Data reduction

A set of techniques can be used for reducing unwanted background events from the recorded proton spectra as in case of the ^{23}Al β-decay study. Requirement of β-coincidence, multiplicity of one in both sides of the DSSSD (narrowing the decays to one pixel) and that the front-back energy difference is not too large reject most of the random noise and clear the β background significantly.

The intensities of the two strongest known proton lines were used to check that no relevant data had been lost as the different conditions were applied to the data, in order to subtract the background. There are losses due to the incomplete charge collection of the events taking place in the interface of the adjacent strips and for protons that leave the detector, however these effects can be estimated from simulations. Geant4 simulations show that below $E_p = 1.0$ MeV we miss less than 4% of the events and between 1.0 ... 1.5 MeV we lose 5-10% of the events. These effects are corrected and the uncertainty of these corrections does not add considerably to the overall uncertainties.

A.1. Background reduction routine

The details of the background reduction routine used in the case of ^{23}Al (section 5.3) are given here. In this experiment, we had to use background subtraction to look for the astrophysically interesting proton energies. The β-response of the detector was measured by using ^{22}Mg, which β-decays to excited states of ^{22}Na emitting only γ-rays. Simulations have shown that the energy-loss spectra of the emitted positrons are very similar in the two cases, and the measurements confirmed that, so this is a safe assumption to start with.

As the statistics collected for ^{22}Mg were smaller than for ^{23}Al, the collected spectra have to be scaled to match each other. When hunting a small amount of events one cannot reject any data, thus scaling ^{23}Al down does not come into question. Thus the measured β spectrum from ^{22}Mg must be scaled up to match the statistics. However, due to small statistics, there are small fluctuations in the continuum. Multiplying

the spectrum directly would result in artificially large bumps which could in turn create artificial peaks in the reduced spectrum.

To get rid of these statistical fluctuations, the spectrum was smoothed by using standard routines from the histogramming classes of the ROOT analysis framework[1]. Before smoothing, the data was re-binned with method `TH1::Rebin()` from 1 keV/ch to 4 keV/ch to initially reduce the number of fluctuations. The smoothing routine starts with the background shape estimation with ROOT method `TH1::ShowBackground()` and is followed by smoothing with method `TH1::Smooth()`. After smoothing, the routine looks at the bin contents at the user defined energy (the energy where the background height is needing to be matched), calculates the scaling factor and uses method `TH1::Add()` to create the scaled histogram from the original. Finally, the background reduced spectrum is then created by subtracting the smoothed and scaled ^{22}Mg spectrum from the ^{23}Al spectrum.

The backgrounds were chosen to be matched around 150 keV which is above our worst noise conditions (and thus our trigger thresholds) and low enough not to be in the region of the interesting proton lines. In practice, matching points in energies ranging from 120 to 190 keV were checked.

The larger peak around 270 keV can be used as an additional check for our background subtraction. This peak is visible as a clear "bump" on top of the beta continuum in the raw data presented in Fig. A.1 and it can be fitted with a shape described by Eq. 4.5 on top of a simple background of an exponential shape. The values for the peak centroid and area obtained by this procedure were in excellent agreement with the results obtained from the background-subtracted fit previously described. We conclude that the intensities of the proton peaks around 200 keV obtained from the background-subtracted spectrum have an uncertainty of 20% or better.

A.2. On error analysis of the reduced spectrum

The uncertainties in the background reduction relate mainly to the peak areas. The peak location is assumed to stay intact if the background spectrum is smooth enough. The uncertainty of the peak areas in the reduced spectrum can be estimated by (at least) two different methods.

[1] The methods mentioned are well documented in a searchable reference guide with references to relevant literature, always up to date and available for each version of ROOT at `http://root.cern.ch`. In this work version 5.22 was used unless otherwise stated.

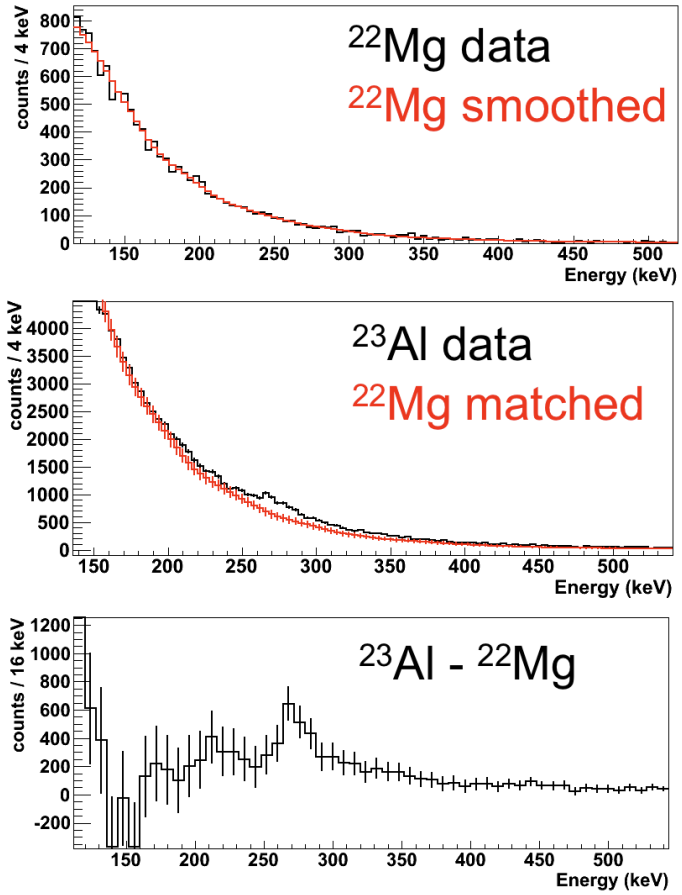

Figure A.1: Illustration of the background reduction in the β decay of ^{23}Al. The top panel shows the measured ^{22}Mg data in black and the background shape after smoothing. The middle panel shows the ^{23}Al data and the smoothed ^{22}Mg data from the top panel, scaled to the β-continuum of the ^{23}Al data at 150 keV. The bottom panel shows the resulting spectrum when the smoothed ^{22}Mg β response is subtracted from the ^{23}Al data.

If the function describing the background can be thought to vary slowly under the peak of interest, one can safely fit the background separately outside the peak region to obtain shape of the background. This shape can be then used as a starting point for the composite fit where the peak and the background are described by their own functions, but fitted as a sum. If the peak is described with a function $f_{\mathrm{peak}}(x)$, the ^{22}Mg background with $f_{\mathrm{bkg}}(x)$ and our original non-reduced ^{23}Al spectrum by $f_{\mathrm{data}}(x)$, our peak on top of the background, as well as after the subtraction should be:

$$f_{\mathrm{peak}}(x) = f_{\mathrm{data}}(x) - f_{\mathrm{bkg}}(x). \tag{A.1}$$

The uncertainty of the peak area is then:

$$\sigma^2_{\mathrm{peak}} = \sigma^2_{\mathrm{data}} + \sigma^2_{\mathrm{bkg}}, \tag{A.2}$$

which becomes $\approx A_{\mathrm{data}} + A_{\mathrm{bkg}}$ for Poisson statistics [156].

The original data has a statistical error of $\sqrt{N}$ for each bin and this is stored by ROOT into the histogram objects. [2] Each of the applied methods, mentioned in the earlier section, calculate and refill the error structure propagating the errors in each step. The uncertainties after the background subtraction are about three times larger than the bare statistical error. This yields a more realistic estimate for the uncertainties in the fitted peaks.

The relative error for the peak area from the fit to the background reduced spectrum with bin errors given by ROOT is 16%, whereas by using only Poisson statistics for the bins, the fit error is ∼2% and the estimated effect for the error in peak area (Eq. A.2) due to background reduction is ∼13%. The best estimate for the starting point of the final fitting with full errors was deduced from a fit only to the Poisson errors to avoid local minima in the chi squared space. While the errors are somewhat large, they are a more realistic representation of the uncertainties for the resulting spectrum.

[2] N.B. Method `TH1::SetDefaultSumw2()` has to be used before making any new histograms to create the structure to store the sum of squares of weights by default. This structure is filled with the existing bin contents. The error per bin will be computed as $\sqrt{(\mathrm{sumofsquaresofweight})}$ for each bin. If existing histograms are loaded from external root-files, `TH1::Sumw2()` has to be used.

A.3. Line shape for β-delayed proton emission observed inside a Si detector

As presented in chapter 4, the β-tail of an observed proton peak can be understood with equation 4.5:

$$f(E) = \frac{1}{\sqrt{2\pi}\sigma} exp\left[-\frac{1}{2}\left(\frac{E-\mu}{\sigma}\right)^2\right], \text{for } E \leq \mu + a \cdot \sigma$$
$$f(E) \propto |E-\mu|^{-n}, \text{for } E > \mu + a \cdot \sigma.$$

On the other hand, this line shape is valid only for protons with low enough energy to be stopped fully inside the detection volume. The energy of escaping protons, determined from a SRIM [64] calculation for both detectors is illustrated in Fig. A.2.

In practice the detector responses were determined by Geant4 [87] simulations. An example of one proton line with an escape tail is given in Fig. A.3. In theory, the energy deposition of charged particles in a thin layer follows the Landau distribution [157]. There is no analytical solution for the Landau distribution, but an approximate form that reproduces the overall behavior is given in Ref. [158]:

$$f(E) \propto exp\left(-\frac{1}{2}\lambda + exp(-\lambda)\right), \lambda = (E - E_0)/w, \tag{A.3}$$

where E_0 is the most probable value of the distribution and w is the width parameter. It is worth noting that Eq. A.3 is only an approximation and it does not reproduce the properties of Landau distribution exactly, especially when $\lambda \to \infty$ (for more details, see e.g. Ref. [159]). However, at relevant energies this form is a good approximation of the simulated data as demonstrated in Fig. A.3. The escape tail shape was determined from the simulations and then added as a constant contribution for each of the peaks in the fit to the real measurement data.

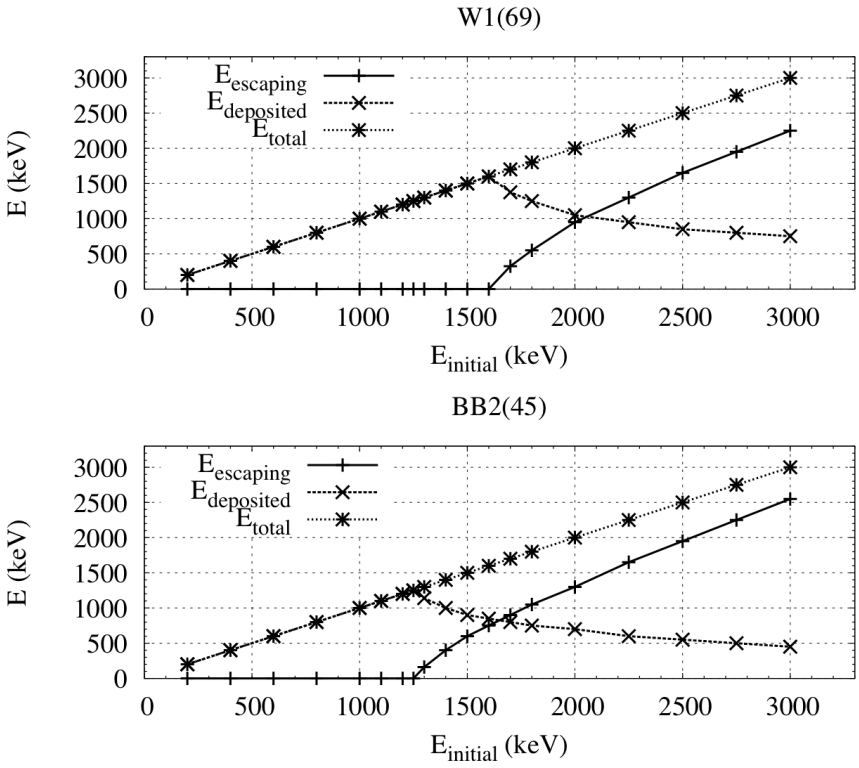

Figure A.2: Energy deposition of protons escaping the detection volume based on a SRIM [64] calculation.

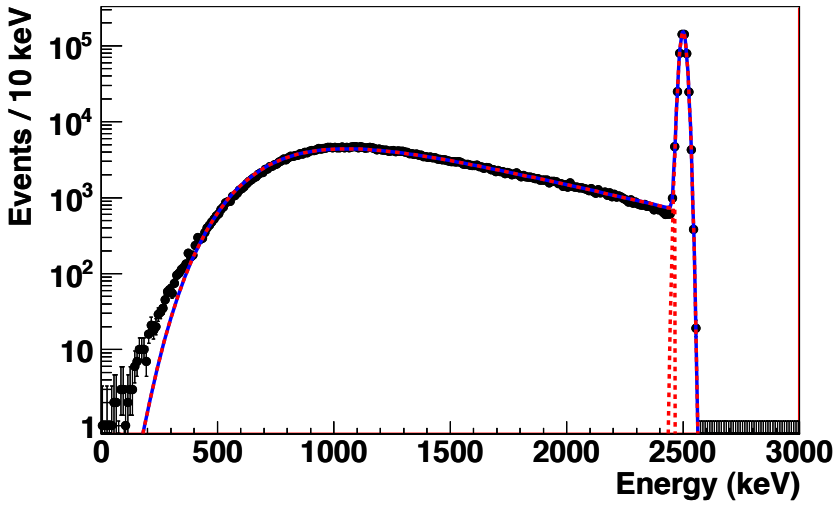

Figure A.3: Simulated line shape of escaping protons. In this example 10^6 protons are emitted in the middle of a pixel of a W1 type detector (thickness 69 μm). Also shown is the approximate form of the energy response given by a fit to Eq. A.3 and a Gaussian peak describing the full-energy proton peak. Simulation data courtesy of B. Roeder.

Bibliography

[1] K. S. Krane, *Introductory Nuclear Physics* (John Wiley & Sons Inc., New York, 1988).

[2] A. Wapstra, G. Audi, and C. Thibault, Nucl. Phys. A **729**, 129 (2003).

[3] G. Audi, A. Wapstra, and C. Thibault, Nucl. Phys. A **729**, 337 (2003).

[4] G. Audi and W. Meng, Private Communication (2011), the AME2011-preview: `http://amdc.in2p3.fr/masstables/Ame2011int/filel.html`.

[5] J. Suhonen, *From Nucleons to Nucleus – Concepts of Microscopic Nuclear Theory* (Springer, Berlin / Heidelberg, 2007), ISBN: 978-3-540-48859-0.

[6] O. Haxel, J. H. D. Jensen, and H. E. Suess, Phys. Rev. **75**, 1766 (1949).

[7] W. Heisenberg, Z. Phys. **77**, 1 (1932).

[8] S. M. Lenzi and M. Bentley, in *The Euroschool Lectures on Physics with Exotic Beams, Vol. III*, Vol. 764 of *Lect. Notes Phys.*, edited by J. Al-Khalili and E. Roeckl (Springer, Berlin / Heidelberg, 2009), pp. 57–98.

[9] E. P. Wigner, in *Proceedings of the Robert A. Welch Foundation Conferences on Chemical Research.*, edited by W. O. Millikan (Robert A. Welch Foundation, Houston, 1958), Vol. 1, p. 88.

[10] W. MacDonald, Phys. Rev. **98**, 60 (1955).

[11] W. MacDonald, Phys. Rev. **100**, 51 (1955).

[12] W. MacDonald, Phys. Rev. **101**, 271 (1956).

[13] S. Weinberg and S. Treiman, Phys. Rev. **116**, 465 (1959).

[14] J. Jänecke, Phys. Rev. **147**, 735 (1966).

[15] J. Jänecke, in *Isospin in Nuclear Physics*, edited by D. H. Wilkinson (North-Holland publishing company - Amsterdam, The Netherlands, 1969), pp. 297–387.

[16] I. S. Towner and J. C. Hardy, Phys. Rev. C **77**, 025501 (2008).

[17] J. C. Hardy and I. S. Towner, Phys. Rev. C **79**, 055502 (2009).

[18] E. Fermi, Z. Phys. **88**, 161 (1934).

[19] G. Gamow and E. Teller, Phys. Rev. **49**, 895 (1936).

[20] S. Raman and N. B. Gove, Phys. Rev. C **7**, 1995 (1973).

[21] B. Singh, J. L. Rodriguez, S. S. M. Wong, and J. K. Tuli, Nucl. Data Sheets **84**, 487 (1998).

[22] P. J. Brussaard and P. W. M. Glaudemans, *Shell-model applications in nuclear spectroscopy* (North-Holland publishing company, Amsterdam, 1977).

[23] K. Nakamura and Particle Data Group, J. Phys. G **37**, 075021 (2010).

[24] I. S. Towner and J. C. Hardy, Rep. Prog. Phys. **73**, 046301 (2010).

[25] N. Gove and M. Martin, At. Data and Nucl. Data Tables **10**, 205 (1971).

[26] H. Primakoff and S. P. Rosen, Rep. Prog. Phys. **22**, 121 (1959).

[27] B. Blank and M. Borge, Prog. Part. Nucl. Phys. **60**, 403 (2008).

[28] M. Pfützner, L. V. Grigorenko, M. Karny, and K. Riisager, arXiv:1111.0482v1 (nucl-ex) .

[29] C. Iliadis, Nucl. Phys. A **618**, 166 (1997).

[30] C. Iliadis, *Nuclear Physics of Stars* (Wiley-VCH, Weinheim, 2007), ISBN: 978-3-527-40602-9.

[31] J. Cerny and J. C. Hardy, Annu. Rev. Nucl. Sci. **27**, 333 (1977).

[32] J. M. Soper, in *Isospin in Nuclear Physics*, edited by D. H. Wilkinson (North-Holland publishing company - Amsterdam, The Netherlands, 1969), pp. 229–258.

[33] J. C. Hardy, J. E. Esterl, R. G. Sextro, and J. Cerny, Phys. Rev. C **3**, 700 (1971).

[34] N. Auerbach, Physics Reports **98**, 273 (1983).

[35] W. Ormand and B. Brown, Phys. Lett. B **174**, 128 (1986).

[36] C. Rolfs and W. Rodney, *Cauldrons in the Cosmos* (The University of Chicago Press, Chicago 60637, USA, 1988).

[37] *Fundamental Astronomy*, edited by H. Karttunen *et al.* (Springer, Berlin Heidelberg, 2003), title of original Finnish edition: Tähtitieteen perusteet (Ursan julkaisuja 56).

[38] J. Jose, M. Hernanz, and C. Iliadis, Nucl. Phys. A **777**, 550 (2006).

[39] J. José and C. Iliadis, Rep. Prog. Phys. **74**, 096901 (2011).

[40] J. Isern, M. Hernanz, and J. Jose, in *Astronomy with Radioactivities*, Vol. 812 of *Lecture Notes in Physics*, edited by R. Diehl, D. H. Hartmann, and N. Prantzos (Springer, Berlin / Heidelberg, 2011), pp. 233–305.

[41] D. A. Hardy, NASA Astronomy Picture of the Day Collection, http://apod.nasa.gov/apod/ap060726.html.

[42] F. Paresce and R. Jedrzejewski, News release: STScI-1994-06, http://hubblesite.org/newscenter/archive/releases/star/nova/1994/06/.

[43] C. Iliadis *et al.*, Astrophys.J. Suppl. **142**, 105 (2002).

[44] J. Jose, A. Coc, and M. Hernanz, Astrophys. J. **520**, 347 (1999).

[45] J. Jose, A. Coc, and M. Hernanz, Astrophys. J. **560**, 897 (2001).

[46] A. L. Sallaska *et al.*, Phys. Rev. Lett. **105**, 152501 (2010).

[47] R. J. Tighe *et al.*, Phys. Rev. C **52**, R2298 (1995).

[48] K. Peräjärvi *et al.*, Phys. Lett. B **492**, 1 (2000).

[49] P. Dendooven, Nucl. Instrum. and Meth. in Phys. Res. B **126**, 182 (1997).

[50] M. Huyse, in *The Euroschool Lectures on Physics with Exotic Beams, Vol. I*, Vol. 651 of *Lecture Notes in Physics*, edited by J. Al-Khalili and E. Roeckl (Springer, Berlin / Heidelberg, 2004), pp. 1–32.

[51] J. Äystö, Nucl. Phys. A **693**, 477 (2001).

[52] P. Karvonen *et al.*, Nucl. Instrum. and Meth. in Phys. Res. B **266**, 4794 (2008).

[53] A. Nieminen *et al.*, Phys. Rev. Lett. **88**, 094801 (2002).

[54] V. Kolhinen *et al.*, Nucl. Instrum. and Meth. in Phys. Res. A **528**, 776 (2004).

[55] J. Huikari *et al.*, Nucl. Instrum. and Meth. in Phys. Res. B **222**, 632 (2004).

[56] FAIR – Facility for Antiproton and Ion Research, `http://www.gsi.de/portrait/fair_e.html`.

[57] H. Geissel *et al.*, Nucl. Instrum. and Meth. in Phys. Res. B **204**, 71 (2003), `http://www.gsi.de/forschung/fair_experiments/superfrs/index_e.html`.

[58] H. Geissel *et al.*, Nucl. Instrum. and Meth. in Phys. Res. A **282**, 247 (1989).

[59] D. Rodriguez *et al.*, Eur. Phys. J. ST **183**, 1 (2010).

[60] G. Savard *et al.*, Nucl. Phys. A **701**, 292 (2002).

[61] L. Weissman *et al.*, Nucl. Phys. A **746**, 655 (2004).

[62] P. Dendooven, S. Purushothaman, and K. Gloos, Nucl. Instrum. and Meth. in Phys. Res. A **558**, 580 (2006).

[63] S. Purushothaman *et al.*, Nucl. Instrum. and Meth. in Phys. Res. B **266**, 4488 (2008).

[64] J. F. Ziegler, SRIM/TRIM package, `http://www.srim.org/`.

[65] R. Tribble, R. Burch, and C. Gagliardi, Nucl. Instrum. and Meth. in Phys. Res. A **285**, 441 (1989).

[66] R. Tribble, C. Gagliardi, and W. Liu, Nucl. Instrum. and Meth. in Phys. Res. B **56-57**, 956 (1991).

[67] R. Tribble *et al.*, Nucl. Phys. A **701**, 278 (2002).

[68] K. Blaum, Physics Reports **425**, 1 (2006).

[69] T. Eronen *et al.*, Hyperfine Interactions (2011), TO BE PUBLISHED.

[70] G. Savard *et al.*, Phys. Lett. A **158**, 247 (1991).

[71] G. Graff, H. Kalinowsky, and J. Traut, Z. Phys. A **297**, 35 (1980).

[72] M. König *et al.*, Int. J. Mass Spect. Ion Proc. **142**, 95 (1995).

[73] K. Blaum *et al.*, J. Phys. B **36**, 921 (2003).

[74] G. Gabrielse, Int. J. Mass Spect. **279**, 107 (2009).

[75] G. Gabrielse, Phys. Rev. Lett. **102**, 172501 (2009).

[76] A. Saastamoinen *et al.*, Phys. Rev. C **80**, 044330 (2009).

[77] T. Eronen, Phd thesis, University of Jyväskylä, 2008.

[78] V.-V. Elomaa, Phd thesis, University of Jyväskylä, 2009.

[79] J. I. Prisciandaro, A. C. Morton, and P. F. Mantica, Nucl. Instrum. and Meth. in Phys. Res. A **505**, 140 (2003).

[80] J.-C. Thomas *et al.*, Eur. Phys. J. A **21**, 419 (2004).

[81] J. Büscher *et al.*, Nucl. Instrum. and Meth. in Phys. Res. B **266**, 4652 (2008).

[82] R. Kumar *et al.*, Nucl. Instrum. and Meth. in Phys. Res. A **598**, 754 (2009).

[83] A. Saastamoinen *et al.*, Phys. Rev. C **83**, 045808 (2011).

[84] A. Saastamoinen *et al.*, AIP Conf. Proc **1409**, In press (2011).

[85] V. E. Iacob *et al.*, Phys. Rev. C **82**, 035502 (2010).

[86] O. Tarasov and D. Bazin, Nucl. Instrum. and Meth. in Phys. Res. B **266**, 4657 (2008), `http://www.nscl.msu.edu/lise`.

[87] S. Agostinelli *et al.*, Nucl. Instrum. and Meth. in Phys. Res. A **506**, 250 (2003).

[88] R. Brun and F. Rademakers, Nucl. Instrum. and Meth. in Phys. Res. A **389**, 81 (1997).

[89] M. Ranjan, Phd thesis, University of Groningen, 2011.

[90] M. Ranjan *et al.*, Europhys. Lett. **96**, 52001 (2011).

[91] R. B. Firestone, Nucl. Data Sheets **108**, 1 (2007).

[92] V. E. Iacob *et al.*, Phys. Rev. C **74**, 045810 (2006).

[93] Y. Zhai, Ph. D. thesis, Texas A&M University, 2007.

[94] J. Britz, A. Pape, and M. Antony, Atomic Data and Nuclear Data Tables **69**, 125 (1998).

[95] F. Herfurth *et al.*, Phys. Rev. Lett. **87**, 142501 (2001).

[96] M. Pyle *et al.*, Phys. Rev. Lett. **88**, 122501 (2002).

[97] K. Blaum *et al.*, Phys. Rev. Lett. **91**, 260801 (2003).

[98] S. Triambak *et al.*, Phys. Rev. C **73**, 054313 (2006).

[99] C. Yazidjian *et al.*, Phys. Rev. C **76**, 024308 (2007).

[100] R. Ringle *et al.*, Phys. Rev. C **75**, 055503 (2007).

[101] A. A. Kwiatkowski *et al.*, Phys. Rev. C **80**, 051302(R) (2009).

[102] A. Kankainen *et al.*, Phys. Rev. C **82**, 052501(R) (2010).

[103] A. Signoracci and B. A. Brown, Phys. Rev. C **84**, 031301 (2011).

[104] C. Wrede *et al.*, Phys. Rev. C **81**, 055503 (2010).

[105] D. Melconian *et al.*, Phys. Rev. Lett. **107**, 182301 (2011).

[106] B. A. Brown and W. A. Richter, Phys. Rev. C **74**, 034315 (2006).

[107] A. Parikh *et al.*, Phys. Rev. C **71**, 055804 (2005).

[108] J. A. Caggiano *et al.*, Phys. Rev. C **64**, 025802 (2001).

[109] T. Al-Abdullah *et al.*, Phys. Rev. C **81**, 035802 (2010).

[110] A. Banu *et al.*, Phys. Rev. C **84**, 015803 (2011).

[111] D. Jenkins *et al.*, Phys. Rev. Lett. **92**, 031101 (2004).

[112] R. G. Sextro, R. A. Gough, and J. Cerny, Phys. Rev. C **8**, 258 (1973).

[113] K. Peräjärvi, private communication.

[114] M. Mukherjee *et al.*, Eur. Phys. J. A **35**, 31 (2008).

[115] H. Nann, A. Saha, and B. H. Wildenthal, Phys. Rev. C **23**, 606 (1981).

[116] S. Kubono *et al.*, Z. Phys. **348**, 59 (1994).

[117] O. S. Kirsebom, Phd thesis, University of Aarhus, 2010.

[118] O. S. Kirsebom *et al.*, Eur. Phys. J. A **47**, 130 (2011).

[119] D. Black, Geochim.et Cosmochim. Acta **36**, 347 (1972).

[120] A. F. Iyudin *et al.*, Astron. Astrophys. **300**, 422 (1995).

[121] R. Diehl *et al.*, New Astron. Rev. **52**, 440 (2008).

[122] A. F. Iyudin *et al.*, Astron. Astrophys. **443**, 477 (2005).

[123] S. Bishop *et al.*, Phys. Rev. Lett. **90**, 162501 (2003).

[124] B. Davids *et al.*, Phys. Rev. C **68**, 055805 (2003).

[125] S. Seuthe *et al.*, Nucl. Phys. A **514**, 471 (1990).

[126] S. Schmidt *et al.*, Nucl. Phys. A **591**, 227 (1995).

[127] F. Stegmüller *et al.*, Nucl. Phys. A **601**, 168 (1996).

[128] A. L. Sallaska *et al.*, Phys. Rev. C **83**, 034611 (2011).

[129] C. Rowland *et al.*, Astrophys. J. **615**, L37 (2004).

[130] L. Erikson *et al.*, Phys. Rev. C **81**, 045808 (2010).

[131] B. Cederwall *et al.*, Nucl. Instrum. and Meth. in Phys. Res. A **354**, 591 (1995).

[132] V. E. Iacob *et al.*, Phys. Rev. C **74**, 015501 (2006).

[133] D. J. Vieira, R. A. Gough, and J. Cerny, Phys. Rev. C **19**, 177 (1979).

[134] A. Kankainen *et al.*, Eur. Phys. J. A **27**, 67 (2006).

[135] J. Äystö *et al.*, Phys. Lett. B **110**, 437 (1982).

[136] J. Äystö *et al.*, Phys. Rev. C **32**, 1700 (1985).

[137] T. Ognibene *et al.*, Phys. Rev. C **54**, 1098 (1996).

[138] P. Endt, Nucl. Phys. A **633**, 1 (1998).

[139] J. Vernotte *et al.*, Nucl. Phys. A **655**, 415 (1999).

[140] D. Jenkins *et al.*, Phys. Rev. C **72**, 031303(R) (2005).

[141] Z. Ma *et al.*, Phys. Rev. C **76**, 015803 (2007).

[142] C. Wrede *et al.*, Phys. Rev. C **76**, 052802(R) (2007).

[143] C. Wrede *et al.*, Phys. Rev. C **79**, 045803 (2009).

[144] A. Parikh *et al.*, Phys. Rev. C **83**, 045806 (2011).

[145] M. S. Basunia, Nucl. Data Sheets **111**, 2331 (2010).

[146] F. Ajzenberg-Selove and J. L. Wiza, Phys. Rev. **143**, 853 (1966).

[147] J. Äystö *et al.*, Phys. Scr. **T5**, 193 (1983).

[148] S. Amari, E. Zinner, J. Jose, and M. Hernanz, Nucl. Phys. A **688**, 430C (2001).

[149] J. Jose *et al.*, Astrophys. J **612**, 414 (2004).

[150] D. G. Jenkins *et al.*, Phys. Rev. C **73**, 065802 (2006).

[151] W. Benenson *et al.*, Phys. Rev. C **15**, 1187 (1977).

[152] C. Wrede *et al.*, Phys. Rev. C **79**, 045808 (2009).

[153] O. Tengblad *et al.*, Nucl. Instrum. and Meth. in Phys. Res. A **525**, 458 (2004).

[154] R. D. Horansky *et al.*, J. Appl. Phys. **107**, 044512 (2010).

[155] L. Trache *et al.*, AIP Conf. Proc **1409**, In press (2011).

[156] P. R. Bevington and D. K. Robinson, *Data Reduction and Error Analysis for the Physical Sciences*, 3rd ed. (McGraw-Hill, New York, NY 10020, USA, 2003).

[157] L. Landau, J. Phys. (USSR) **8**, 201 (1944).

[158] J. E. Moyal, Phil. Mag. **46**, 263 (1955).

[159] K. S. Kölbig and B. Schorr, Comp. Phys. Comm. **31**, 97 (1984).